

INAUGURAL - DISSERTATION
zur
Erlangung der Doktorwürde
der
Naturwissenschaftlich-Mathematischen
Gesamtfakultät
der
Ruprecht-Karls-Universität
Heidelberg

Vorgelegt von
M. Tech.- Srinivas Yarlanki
aus Kharagpur, Indien
Tag der mündlichen Prüfung: 18. November 2005

Thema

Modeling of Droplet Interactions

Gutachter: Prof. Dr. Eva Gutheil

Priv.-Doz. Dr. Uwe Riedel

Zusammenfassung

Sprays in praktischen Anwendungen bestehen aus vielen Tröpfchen. Das Verhalten eines Tröpfchens hängt stark von den benachbarten Tröpfchen ab, wenn der Abstand zwischen beiden in der Größenordnung des Tröpfchendurchmessers liegt. In Spray-Berechnungen wird die Interaktion zwischen Tröpfchen während Aufheizung, Verdampfung, Zündung und Verbrennung normalerweise vernachlässigt. Diese Annäherung ist unzureichend, da benachbarte Tröpfchen sowohl eine Energiesenke als auch eine Brennstoffquelle für das umgebende Gas darstellen.

Numerische Untersuchungen von Tröpfchenwechselwirkungen wurden bisher meist in einer zweidimensionalen axialsymmetrischen Konfiguration durchgeführt. Diese Konfiguration vernachlässigt die Tatsache, dass hydrodynamische Wechselwirkungen meist dreidimensionaler Natur sind. Außerdem haben numerische Untersuchungen in der Vergangenheit viele wichtige Eigenschaften wie die Abbremsung der Tröpfchen sowie Zirkulationen innerhalb der Tröpfchen vernachlässigt. In einigen Fällen wurden grundlegende Details des numerischen Lösungsverfahrens wie die Berechnung der korrekten Gleichungen für bewegte Gitter nicht beachtet.

Es wurde eine numerische Methode entwickelt, um die Wechselwirkungen zwischen Tröpfchen während der Zündung in drei Dimensionen zu untersuchen. Dabei wurden hydrodynamische Wechselwirkungen, Zirkulationen innerhalb der Tröpfchen, Abbremsung durch das umgebende Gas, detaillierte Chemie, sowie weitere zusätzliche Bedingungen des numerischen Lösungsverfahrens berücksichtigt. Die Einzelheiten für die Berücksichtigung der korrekten Gleichungen für bewegte Gitter wurden erläutert. Ein modifiziertes Mehrgitterverfahren wurde für die Berechnung der Verdampfung der Tröpfchen angewandt. Nachdem sichergestellt wurde, dass das Programm die Interaktion zwischen Tröpfchen zuverlässig simuliert, wurden diese Effekte für ein einzelnes Ethanol-Tröpfchen und für zwei gleich große Ethanol-Tröpfchen in Tandem-Konfiguration durch numerische Simulation untersucht. Die berechnete Zündverzögerung für wechselwirkende Tröpfchen stimmt gut mit den experimentellen Daten überein.

Abstract

Practical sprays are composed of many droplets and a typical droplet will be strongly influenced by the neighboring droplets when the average spacing between them is of the order of a few droplet diameters. In spray computations, typically the interaction of droplets during heating, vaporization, ignition, and combustion is neglected. This approximation is poor since neighboring droplets constitute an energy sink and a fuel source to the gas surrounding the droplets.

Numerical studies of droplet interactions, so far, have been mostly carried out in two dimensional axisymmetric configuration which is hard to justify as hydrodynamic interactions are in general three dimensional. Moreover, numerical studies in the past often neglected many important features of the flow like gas phase deceleration, internal circulation in the droplets. In some cases even essential details of the numerical solution procedure like accounting for the correct equations on moving grids have been missing.

A numerical method is developed and droplet interactions during ignition are studied in a three dimensional configuration accounting for hydrodynamic interactions, internal circulation inside the droplets, gas phase deceleration, detailed chemistry and correct equations on moving grids. The details of accounting for the correct equations on moving grids are discussed. A modified multigrid technique is applied to the droplet vaporization problem. After assessing the ability of the code to accurately simulate the interaction between droplets, interaction effects are studied by numerically simulating ignition of a single ethanol drop and of a pair of identical ethanol droplets in tandem configuration. The calculated ignition delay for the interacting droplets case agrees favorably with experiments.

Acknowledgments

I express my sincere gratitude to my supervisor Prof. Dr. E. Gutheil.

I profoundly thank Mr. Stefan Friedel from the central administration of computing services for his help with the clusters. I thank Mr. Peter Groppenbacher, Mr. Marco De Rosa and Ms. Daniela Urzica for their help with this thesis. I also thank all my past and present colleagues and friends for their pleasant company.

I acknowledge the extraordinary understanding and support of Prof. Gutheil and Mr. Atindra Sapkota. I could not have made it without them standing by me through some very trying and difficult times.

Financial support from DFG is greatly appreciated.

Nomenclature

A	coefficient in discretized equation [-]
A_r	pre-exponential factor in Arrhenius rate equation ($[(\text{mol}/\text{m}^3)^{1-n}/\text{s}]$: for a reaction of order n)
C	molar concentration [kg/m^3]
C_D	total drag coefficient [-]
C_L	total lift coefficient [-]
c_P	specific heat capacity at constant pressure [$\text{J}/(\text{kgK})$]
d	instantaneous droplet diameter [m]
d_o	initial droplet diameter [m]
D_{ij}	binary diffusion coefficient of species i into species j [m^2/s]
$E_{a,r}$	activation energy of reaction r [J/mol]
f	integrand at control volume face [-]
$F_{D,F}$	friction drag force [N]
$F_{D,p}$	pressure drag force [N]
$F_{D,T}$	thrust drag force [N]

F_L	lift force [N]
h	specific enthalpy [J/kg]
h_{i,T^o}^o	standard enthalpy of formation of species i at reference temperature T^o [J/kg]
\mathbf{i}	unit vector in the main flow direction [-]
I	identity tensor [-]
I_h^{2h}	restriction operator [-]
I_{2h}^h	prolongation operator [-]
\mathbf{j}	unit vector orthogonal to the main flow direction [-]
k	thermal conductivity [J/(msK)]
$k_{f,r}$	forward rate constant for a chemical reaction r [-]
$k_{b,r}$	backward rate constant for a chemical reaction r [-]
\mathbf{k}	unit vector orthogonal to \mathbf{i} and \mathbf{j} [-]
L_{vap}	latent heat of vaporization of fuel [J/kg]
\dot{m}	mass-flux due to vaporization [kg/(m ² s)]
m_e	mass-flux across eastern CV face [kg/(m ² s)]
M	molecular weight [kg]
\mathbf{n}	outward unit normal vector [-]
N_R	total number of chemical reactions [-]
N_S	total number of species [-]
\overline{Nu}	average Nusselt number [-]
p	local pressure [Pa]

P	absolute pressure [Pa]
R	universal gas constant [J/(molK)]
R_h^m	residual vector after m iterations on grid with spacing h
$r_{i,k}$	molar rate of creation/destruction of species i in reaction k [mol/s]
S	CV surface area [m ²]
\overline{Sh}	average Sherwood number [-]
t	time [s]
\mathbf{t}_g	unit vector in the direction of shear force at a surface [-]
T	temperature [K]
\mathbf{U}_g	droplet deceleration velocity [m/s]
\mathbf{v}	velocity vector [m/s]
\mathbf{v}_b	local grid velocity vector [m/s]
X	mole fraction [-]
Y	mass fraction [-]

Greek Symbols

Γ	stress tensor [N/m ²]
Ω	CV volume [m ³]
γ	diffusion coefficient [m ² /s]
δ_{ij}	Kronecker delta [-]
$\lambda_{i,r}$	collision efficiency of the i^{th} species in r^{th} reaction [-]

μ	dynamic viscosity [Ns/m ²]
ρ	density [kg/m ³]
τ	viscous part of stress tensor [N/m ²]
$\nu'_{i,k}$	stoichiometric coefficient of species i in reaction k [-]
$\nu''_{i,k}$	stoichiometric coefficient of species i in reaction k [-]
Λ	nte effect of third body collision efficiency [-]
β_r	dimensionless temperature exponent [-]
ϕ	any scalar variable [-]
σ	surface tension [J/m ²]

Subscripts and Superscripts

—	interpolated/average value
~	restricted value
^	coarse grid approximation
*	current estimate of solution
'	correction
o	initial conditions
∞	free-stream conditions
a	air
f	fuel
g	gas phase

h	grid level with spacing h
i	numerical index for species
int	gas-liquid interface
l	liquid phase
m	gaseous mixture of various chemical species
m^*	current estimate after m outer iterations
nb	neighboring control volume
r	numerical index for chemical reactions
T	transpose
u_i	dependent on velocity field
P	Control volume center

Contents

1	Introduction	1
1.1	Interaction Amongst Droplets	2
1.2	Moving Grids and the Space Conservation Law	8
1.3	Application of Multigrid Technique on Moving Grids	10
2	The Mathematical Model	12
2.1	Assumptions	12
2.2	The Governing Equations	13
2.3	The Boundary Conditions	14
2.4	Initial Conditions	19
2.5	Evaluation of Transport Properties	20
2.5.1	Gas Phase Properties	20
2.5.2	Liquid Phase Properties	22
2.6	Evaluation of Forces and Reaction Rates	22
3	The Numerical Method	27
3.1	Discretization of the Partial Differential Equations	28
3.1.1	Discretization in Space	28

3.1.1.1	Approximation of Surface and Volume Integrals . . .	28
3.1.1.2	Interpolation Scheme	30
3.1.2	Discretization in Time	31
3.1.3	Discretized Algebraic Equation System	32
3.2	The Numerical Grid	33
3.2.1	Grid Generation	33
3.2.2	Effect of Grid Movement	33
3.2.2.1	Discretization of Space Conservation Law	34
3.2.2.2	Generalization of Space Conservation Law	35
3.2.2.3	Grid Velocity as a Counterbalance for Unsteady Term	35
3.2.2.4	No Unique Grid Velocity	40
3.2.2.5	Effect of Grid Movement on the Pressure-Correction Equation	40
3.2.2.6	Adjustment of Mass Flux at Outflow	41
3.2.3	The Multigrid Technique	42
3.2.3.1	Application of Multigrid Technique to Droplet Va- porization	44
3.2.3.2	Treatment of Secondary Mass Flow due to Grid Movement	44
3.2.3.3	Change in Geometry due to Grid Movement	46
3.2.3.4	Treatment of Interface Boundary Conditions	47
3.2.3.5	Evaluation of Pressure during Multigrid Restric- tion Cycle	48
3.3	The Pressure-Correction Equation	49

3.4	Implementation of Boundary Conditions	51
3.4.1	Evaluation of Tangential Gradients	51
3.4.2	Evaluation of Grid Distortion and Interface Motion	52
3.5	Solution Algorithm	53
4	Results and Discussion	56
4.1	Generalization of Space Conservation Law	56
4.2	Convergence Acceleration by Multigrid	65
4.3	Interaction between two Solid Spheres in a Convective Flow	70
4.3.1	Wake Structure	71
4.3.2	Pressure and Shear Stress Distribution	74
4.4	Single and Interacting Droplet Ignition	76
5	Conclusions	92

List of Figures

2.1	Schematic of flow configuration	15
3.1	Example of a control volume and notation used	29
3.2	Example CV and its neighbours	31
3.3	Solution algorithm	54
4.1	Schematic of flow configuration	57
4.2	Cross-section of numerical grids	59
4.3	Comparison of temperatures	59
4.4	X -component of velocity at reference point	60
4.5	Comparison of velocity components	61
4.6	Comparison of velocity components	61
4.7	Cross-sections of numerical grids	62
4.8	Comparison of temperatures	63
4.9	Comparison of velocity components	64
4.10	Z -component of velocity	64
4.11	Schematic of flow configuration and the grid around the drop . . .	66
4.12	Multigrid cycle definition	67
4.13	Convergence history	67

4.14 Residual history	68
4.15 Residual history	69
4.16 Residual history	69
4.17 Schematic of the flow configuration for $S = 4.5$ for two cross-sectional views	71
4.18 Streamline patterns in the $X - Y$ plane at a Reynolds number of 100.	72
4.19 Streamline patterns in the $X - Y$ plane for bottom sphere at $S = 1.5$ and $Re = 100$	73
4.20 Distribution of pressure coefficient	75
4.21 Distribution of shear stress coefficient	76
4.22 Grid around drops and the variation of maximum temperature with time	78
4.23 Ignition delay times from Sangiovanni and Kesten (1977)	78
4.24 Comparison of droplet radius and drag coefficients	80
4.25 Comparison of Nusselt and Sherwood numbers	80
4.26 Zoomed view of contour plots of temperature for single droplet at different time instants: top left 0.5 ms, top right 1.0 ms, bottom left 1.5 ms and bottom right 2.0 ms	81
4.27 Zoomed view of contour plots of temperature for interacting droplets at different time instants: from top to bottom 0.5 ms, 1.0 ms, 1.5 ms and 2.0 ms	83
4.28 Contour plot of gas temperature at ignition: single droplet	84
4.29 Contour plot of gas temperature at ignition: interacting droplets	84
4.30 Contour plots of gas temperature at 6.5 ms: single droplet	85

4.31	Contour plots of gas temperature at 6.5 ms: interacting droplets . . .	85
4.32	Contour plots of OH mass fraction at 6.5 ms: single droplet	86
4.33	Contour plots of OH mass fraction at 6.5 ms: interacting droplets .	86
4.34	Contour plots of CO mass fraction at 6.5 ms: single droplet	88
4.35	Contour plots of CO mass fraction at 6.5 ms: interacting droplets .	88
4.36	Contour plots of CO ₂ mass fraction at 6.5 ms: single droplet	89
4.37	Contour plots of CO ₂ mass fraction at 6.5 ms: interacting droplets	89
4.38	Contour plots of CH ₂ O mass fraction at 6.5 ms: single droplet . . .	90
4.39	Contour plots of CH ₂ O mass fraction at 6.5 ms: interacting droplets	90

List of Tables

2.1	Properties in the liquid phase	22
4.1	Description of test cases	57
4.2	Initial parameters used in the study	65
4.3	Initial values used for ethanol droplets	77

Chapter 1

Introduction

Sprays occur in a wide variety of industrial and power applications and in materials processing. A liquid spray in air is a two-phase flow with a gas as the continuous phase and a liquid as the dispersed phase in the form of droplets or ligaments. Practical sprays are composed of many droplets and a typical droplet will be strongly influenced by the neighboring droplets when the average spacing between them is of the order of a few droplet diameters. In spray computations, typically the interaction of droplets during heating, vaporization, ignition, and combustion is neglected. This approximation has been found to be poor since neighboring droplets constitute an energy sink and a fuel source to the gas surrounding the droplets. Therefore, an effort needs to be made to relax this simplification.

A numerical method has been developed to simulate droplet interaction effects during vaporization and combustion using moving grids with finite volume discretization. Multigrid technique has been used on moving grids for convergence acceleration. The current status on droplet interaction problem and on various aspects of the numerical method is briefly reviewed in the following.

1.1 Interaction Amongst Droplets

Interactions amongst droplets found in sprays have been studied both experimentally and theoretically for last many years since the early studies of Cornish (1965) and Fedoseeva (1973). A very comprehensive review is given by Annamalai and Ryan (1992) which is complemented by asymptotic studies by Umemura (1994). The early models used many assumptions such as quasi-steadiness, quiescent ambiance and regularly ordered, fixed droplets to simplify the problem. Noteworthy of such models are:

1. The method of bispherical coordinates for two droplets by Fedoseeva (1973), Samson & Deutch (1977) and Twardus & Brzustowski (1977)
2. Method of images by Labowsky (1976) for up to nine droplets
3. Drop-in-a-bubble model which has been used to model a spherical cloud of droplets by Reiss (1951) and Fuchs (1959) which was modified later by Zung (1967), Tishkoff (1979), Bellan & Cuffel (1983) and Bellan & Harstad (1987)
4. Point source approximations which can model more than 10 droplets (Annamalai and Ryan, 1991)

Of the above mentioned approaches the first two methods can only be applied to a few (less than 10) droplets whereas the point source approximation assumes very large interdroplet spacing. The drop-in-a-bubble model is actively been used and further developed by various authors (see for example Sanyal and Sundarajan (1992), Chen and Tong (1988), Tsai and Sterling (1990), Sripada *et al.* (1996), Huang *et al.* (1996) and Mukhopadhyay and Sanyal (1999)). Although the Drop-in-a-bubble model accounts for droplet interactions through build-up of vapor fuel concentration and cooling of the gas phase environment, hydrodynamic interactions are not accounted for in this model. Due to the large amount of literature available in modeling droplet interactions only those models which account for hydrodynamic interactions in clouds and studies of individual droplet interactions is focussed in the following.

Interactions due to hydrodynamic forces on two freely moving, interacting spheres of different radii were studied by Batchelor and Green (1972) in an inviscid linear flow. Jeffrey and Onishi (1984) extended this work by including the inertia forces. Tal and Sirignano (1984) and Tal *et al.* (1984, 1983) studied heat and mass transfer in an array of non-evaporating droplets at a Reynolds number of about 100. Labowsky (1977, 1980), Umemura *et al.* (1981) and Xiong *et al.* (1985) studied interactions amongst evaporating drops however in these studies convection, internal circulation and transient heating were neglected. Patnaik (1986) included the effects of convection, internal circulation and transient heating in his study of droplet interactions. Raju and Sirignano (1987, 1990) and Chiang *et al.* (1990) extended the studies of Patnaik (1990) further over a wide range of parameters. Numerical modeling techniques were further developed by Lafaurie *et al.* (1994), Rieber and Frohn (1995) and Nobari and Tryggvason (1996) to study collisions of drops.

However, most of these studies were carried out with two or three droplets placed in tandem (i.e. the line joining the droplets being parallel to the main flow) and data on other configurations is scarce. Kim *et al.* (1993) studied the three-dimensional flow interactions between two fixed identical solid spheres and also between two fixed identical liquid droplets placed side-by-side such that the line joining them is normal to the direction of flow. They provided drag, lift and moment coefficients for various separation distances for three different Reynolds numbers of 50, 100 and 150. They found that the two spheres repel each other when they are close and the repulsion is stronger the closer they are. However, the two spheres weakly attract each other at intermediate separation distances (approximately between 7 and 21 droplet diameters) and at large separation distances (greater than about 21 diameters) they do not interact at all. The maximum separation distance at which repulsion or weak attraction occurs decreases with increasing Reynolds number. The force distribution around each sphere was used to explain the flow physics of above described interaction effects. The same flow structure was found for liquid droplets (external flow structure) too, except that the magnitude of the lift, torque and drag was lower than that for solid spheres. Silverman and Sirignano (1994) use the data presented here to develop a correlation, which was used

in their model for droplet interactions. The range of Reynolds numbers and viscosity ratios investigated along with other factors like neglect of heat and mass transfer in this study severely restricts the predictive capability of Silverman and Sirignano's model (1994). Zhang and Fan (2002) investigated the drag forces of particles aligned in a line parallel to the direction of relative motion between the fluid stream and the particles. The particle-particle interactions and wake effects were taken into account for quantitatively describing the drag force. A semi-analytical expression for the drag force of the trailing particle was formulated based on the velocity distribution in the far wake region downstream of the leading particle. The drag force ratio was thus determined for the particle Reynolds number range of 54 to 154 and found to be in agreement with measured values. The model of Silverman and Sirignano (1994) assumed the form and parameters of the correction functions due to lack of experimental or theoretical data. Zhang and Fan's study (2002) could be used as a guideline to improve the correction function for the tandem case in Silverman and Sirignano's model (1994). Devarakonda and Ray (2003) carried out experimental studies of the effect of droplet interactions on unsteady evaporation in a linear stream. They emphasize that if the time needed for the droplets to reach steady state is greater than the droplet residence time (in the experiment) then during the unsteady period the evaporation rate of an interacting droplet may exceed the steady-state evaporation rate of an isolated droplet leading to a correction factor greater than unity if the rate is normalized by the steady-state evaporation rate (Fedoseeva (1973) obtained correction factors greater than 1 for ethanol droplets (see Annamalai and Ryan, 1992)). Thus, during unsteady evaporation, the correction factor should be calculated using the evaporation rate for an identical isolated droplet under identical conditions. They do this by using an energy balance at the interface, written in terms of the heat transfer correction factor and a mass balance at the interface, written in terms of the mass transfer correction factor, for a droplet in the array. These equations can be used to calculate the mass transfer correction factor, from the measured instantaneous evaporation rate and surface temperature of a droplet, and heat transfer correction factor, from the size and temperature history of the droplets. They found that the correction factors for both heat and mass transfer are almost

identical and that they increase as the inter-droplet separation distance increases (but is less than unity). To verify that the correction factor is independent of the fuel used, they used the correction factor obtained from ethanol droplets to calculate the droplet size and surface temperature for methanol droplets (using the energy/mass balance equations), for a given separation distance, and found excellent agreement.

Recently, Renaud *et al.* (2003) carried out experiments on the vaporization of a three-dimensional cubic centered array of 1-octadecanol droplets at critical pressure and also at twice the critical pressure. Labowsky (1976) studied this geometry for a sub-critical pressure and in quiescent ambiance, using the method of images in the past (see Annamalai and Ryan, 1992). The vaporization rate observed by Renaud *et al.* (2003) for the droplet located at the center was effected most as compared to the peripheral droplets in agreement with Labowsky (1976). However, the authors define a mean evaporation rate and use it to draw surprising conclusions that the evaporation rate of the center droplet increases as the separation distance decreases and that the corrections factors for the center droplet are greater than unity. It is possible that the use of mean evaporation rates instead of instantaneous evaporation rates is responsible for these conclusions as Devarakonda and Ray (2003) conclude that neglecting unsteady effects can lead to correction factors greater than unity.

Atthasit *et al.* (2003) experimentally studied the influence of lateral spacing in non-evaporating droplet streams. They found that in the case of a single stream the droplet drag coefficient decreases with decreasing separation distance. However, with multiple adjacent droplet streams, the droplet drag coefficient decreases below a Reynolds number of 45 and increases very rapidly above this Reynolds number and can even exceed isolated droplet drag coefficient. Further, they showed that the variation of the drag coefficient with lateral spacing follows the same qualitative trend as that of Silverman and Sirignano's model (1994). Unfortunately, a direct comparison based on actual relative drop locations was not made instead the data from multiple streams was compared to a spatially averaged drag coefficient correction from Silverman and Sirignano's model (1994) and the Reynolds numbers for the two cases were also different.

Experimental studies of droplet interaction effects on ignition were carried out by Reichenbach *et al.* (1962) who studied n-octane droplet arrays without convection. Inuma (1962) extended the study of Reichenbach *et al.* (1962) to include convective effects. Sangiovanni and Kesten (1975) studied ignition delay of interacting furfuryl alcohol drops in a high temperature environment with forced convection. Sangiovanni and Kesten (1977) extended their previous work to study the effect of spacing on ignition delay for furfuryl alcohol and butyl alcohol drops. Sommer (1986) studied the ignition delay in decane droplet streams in experiment similar to that of Sangiovanni and Kesten (1975). Sato *et al.* (1986) measured the ignition delays in an actual spray using high speed photography. Kadowaki *et al.* (1996) and Nohara *et al.* (2000) conducted experiments in microgravity to study the interaction effects on ignition using ceramic balls soaked with liquid fuel, instead of actual droplets, in their experiments. Due to the complexity of the problem the data on ignition delays in interactive droplet combustion is relatively scarce compared to that of burning rates and flame structure. The burning rates in interactive droplet combustion date to the early studies of Kanevsky (1956) and Rex *et al.* (1956). Later Sangiovanni and Dodge (1978) and Miyasaka and Law (1981) studied interactive combustion experimentally whereas Nuruzzaman *et al.* (1970, 1971) and Rangel and Sirignano (1987, 1988) studied interactive combustion numerically. More recently interactive combustion has been studied experimentally in microgravity by Mikami *et al.* (1994).

Detailed simulation of droplet interactions, in convective flows, accounting for both hydrodynamic and non-hydrodynamic interactions done so far have been limited to non combusting drops. It was extended to combusting drops by Dwyer *et al.* (2000) who carried out a three-dimensional numerical simulation of six stationary heptane droplets, placed asymmetrically in a plane, at two Reynolds numbers of 5 and 30 using the overset or Chimera grids. Their finite volume formulation used the Navier-Stokes equations, in low Mach number approximation, in which the convective fluxes are expressed relative to the grid velocity (as moving grids were used to resolve the regressing drop surface). Internal circulation inside the droplets was neglected and a one dimensional spherical heat conduction equation was used inside the

drops. A two-stage approach was used for droplet combustion. In the first stage the combustion process of droplet group was calculated using one-step global chemistry to determine the temperature and fuel concentrations and in the second stage the combustion of representative single droplets, with averaged local flow effects, was calculated using detailed chemistry. They provided the variations of Nusselt number, droplet diameter, droplet temperature and drag and lift coefficients as a function of time. They found that the Chimera grid is efficient to deal with this kind of problems and that the shape of the reaction zone, evaporation rates and the forces on the droplets were very dependent on the geometry of the array. Further, Reynolds number has a strong influence on droplet interactions. At lower Reynolds number the interactions were much stronger while at higher Reynolds number the array behaved more like a single entity. Stapf *et al.* (1998) relaxed the condition of stationary droplets and a group of ten droplets and was considered. They found that ignition and combustion depend on specific local conditions of the fuel droplets and thus are different at different locations in the spray.

Aouina *et al.* (2001) included spatial temperature variation inside the droplets. They numerically studied convective heating, vaporization, ignition and subsequent combustion of two equal sized liquid oxygen droplets in hydrogen at high pressures. The initial liquid oxygen temperature was cryogenic and the pressure was 10 bar. Detailed chemical reaction systems were used and the physical properties were obtained from NASA polynomials. They found that the ignition time is considerably shorter for two interacting droplets as compared to isolated droplets. Also, the ignition time increases and the combustion mode changes from single droplet flame to an envelope flame as the distance between the droplets decreases. They found that under convective conditions the location of ignition was not identical for the droplets, the upstream droplet ignites in the aft region and the downstream droplet ignites in the fore region.

Although the numerical simulations of Stapf *et al.* (1998), Dwyer *et al.* (2000) and Aouina *et al.* (2001) included hydrodynamic interactions in convective flows a few important details were missed. Stapf *et al.* (1998) neglected internal circulation in the droplets. More impor-

tantly it seems that Stapf *et al.* (1998) also neglected the convective mass flux contribution due to grid movement in the governing equations. The convective mass flux contribution due to grid movement was later included by Dwyer *et al.* (2000) however it was not clear if the space conservation law has been satisfied too. Moreover, Dwyer *et al.* (2000) considered stationary droplets and thus did not account for droplet deceleration. The calculations of Aouina *et al.* (2001) were done in a two dimensional axisymmetric configuration and neglected internal circulation in the droplet and droplet deceleration. The purpose of this thesis is to develop a numerical model and study the droplet interactions in a three dimensional configuration accounting for detailed hydrodynamic interactions, internal circulation inside the droplets, gas phase deceleration, convective mass flux contribution due to grid movement and the space conservation law.

1.2 Moving Grids and the Space Conservation Law

The technique of Moving Grids is applied to wide variety of problems in computational fluid dynamics (CFD). One such class of problems, where moving grids are applied, involve fluid flows in which the computational boundary is moving. Specific examples of the application of moving grids to these flows are abundant in aerospace, biomedical, Combustion, Plasma Physics, Materials Science and turbomachinery research. Another class of problems, applying moving grids, are the moving mesh methods, strategies for adaptive grids which adjust as the solution evolves to better resolve the underlying flow field (see for example Cao *et al.* 2002). Trulio and Trigger (1961) and later Thomas and Lombard (1979) discovered that when moving grids are used, an equation called the Space Conservation Law (SCL) or Geometric Conservation Law (GCL) has to be satisfied along with other conservation equations for mass, momentum and scalars. Demirdžić and Perić (1988) showed that failure to satisfy the SCL introduces errors in the form of artificial mass sources. More recently, Gulliard and Farhat (2000) have reemphasized the importance of SCL and proved that satisfying the space conservation law, in an appropriate discretized form, is a sufficient condition for a numerical scheme to be at least first-order time-accurate on moving meshes. Numerical methods for sat-

isfying the SCL (or GCL) are presented by Thomas and Lombard (1979) for finite-difference schemes, Demirdžić and Perić (1988 and 1990) for finite volume schemes, Farhat *et al.* (2001) and Geuzaine *et al.* (2003) for Arbitrary Lagrangian Eulerian (ALE) schemes. In all these proposed methods for satisfying the SCL, the time integration scheme used for SCL is (and should be) the same as that for other conservation equations. Perhaps this was not stated explicitly enough and it is not surprising that Kamakoti and Shyy (2004) found that for a first-order fully implicit flow solver, and four different time integration schemes for SCL, the first-order fully implicit time integration of SCL gave the best results.

Although, the importance of SCL has been emphasized many times in the literature (see Thomas and Lombard 1979, Demirdžić and Perić, 1988 and Gulliard and Farhat, 2000) the exact arguments used to emphasize it require further attention. Thomas and Lombard (1979) emphasized that satisfying the SCL ensures that if an initially *spatially uniform flow* (which is a steady flow and hence not applicable to unsteady flows) is computed on moving grids then the numerical solution would reproduce that uniform flow. Demirdžić and Perić (1988) also considered a *spatially uniform flow* (in this case zero velocities and pressures everywhere) and showed that by violating SCL the exact initial solution is destroyed. Gulliard and Farhat 2000, too, prove that satisfying the SCL with compute a *spatially uniform flow* exactly on a moving grid. However, the situation for unsteady flows is not clear. There is evidence in the literature pointing to the insufficiency of the SCL. Tamura and Fujii (1993) suspected that SCL may create problems with unsteady compressible flow simulations, on rapidly distorting grids, but unfortunately they did not provide any conclusive data to support it. Morton *et al.* (1997) found that satisfying or violating the SCL produced the same results. The studies of Tamura and Fujii (1993) and Morton *et al.* (1997) suggest that although SCL is important to prevent artificial mass sources it is inadequate for unsteady flows. In the present study it is shown that SCL is just one equation out of a set of equations which has to be satisfied on moving grids and neglecting other equations of this set produces erroneous solutions for unsteady flows.

1.3 Application of Multigrid Technique on Moving Grids

A wide variety of computationally intensive problems in CFD involve moving boundaries and are often solved using the moving grid technique. Examples of such, computationally intensive problems applying moving grid technique, are design and optimization of flows in rotor-stator configurations found for instance in turbomachinery and stirred reactors, problems involving phase change like solidification/melting, vaporization/condensation or crystallization and fluid structure interaction (FSI) problems involving the deformation and/or movement of a solid body in response to fluid forces acting on it. It is natural to consider the application of convergence acceleration techniques to reduce the computational costs of these problems. The multigrid technique is frequently used for convergence acceleration in CFD.

However, the application of multigrid technique on moving grids is not straightforward except for the simplest cases when the grid movement is either known *a priori* as a function of time or is explicitly calculated from previous time-step values. Quite often, for example in aircraft wing flutter calculations, the grid movement depends on the flow field and has to be calculated implicitly in a coupled manner for each iteration at any given time-step.

Multigrid methods have been successfully applied, on moving grids, for the former class of problems. Arnone *et al.* (1995) and Böhm *et al.* (1997) applied the multigrid technique, on moving grids, to the rotor-stator configuration. The efficiency of the multigrid convergence acceleration, on moving grids, obtained by Böhm *et al.* (1997) for the rotor-stator configuration is comparable to that on stationary grids. Crumpton and Giles (1997) applied the multigrid technique, on moving grids, to bodies undergoing prescribed periodic oscillations. Schäfer *et al.* (2001) presented a methodology for the usage of multigrid technique for coupled fluid-solid problems which can be used when the grid movement is either known *a priori* as a function of time or is explicitly calculated from previous time-step values. Schäfer *et al.* (2000) used the multigrid method of Schäfer *et al.* (2001), on moving grids, to the passing-by of two rectangular objects and to the oscillation of a torsional spring mounted pendulum in a flow field and obtained multigrid convergence acceleration by approximately a factor of 100. Sorensen *et al.* (2003) applied the multigrid technique, on moving grids, to

objects undergoing prescribed oscillations. The multigrid implementation of Sorensen *et al.* (2003) uses an agglomeration technique to generate coarse meshes and local remeshing to improve mesh quality.

In all the studies mentioned above the motion of the moving boundary (and thus the grid movement) was either known *a priori* (prescribed) or calculated explicitly from previous time step values. However, in many applications the motion of the moving boundary or the grid movement is not known *a priori* and depends on the flow field. For such problems the grid movement has to be calculated implicitly such that for a given time step an initial estimate of the grid movement is iteratively improved as the initial estimate of the flow field improves with each iteration. When the solution of the flow field converges for a given time step, the current estimate of the grid movement also converges. The application of multigrid technique to such problems involves additional difficulties because the grid movement (and hence the grid itself) is different for each iteration at any given time step. These difficulties can be further appreciated by considering an example of the questions which arise in applying multigrid technique to such problems.

Assuming that the solution on a grid with spacing, h , is restricted to a coarser grid with spacing, $2h$, and after a few relaxation sweeps, the coarse grid spacing changes from $2h$ to $2h'$. Should the correction to the fine grid solution be prolonged from $2h \rightarrow h$ or from $2h' \rightarrow h$ or from $2h' \rightarrow h'$?

This question as well as other problems arising in the application of multigrid technique when the grid movement is implicitly calculated and modifications to overcome those problems are discussed in this study. An application of multigrid technique on moving grids is presented in which the grid movement is not known *a priori* and is implicitly calculated for each iteration at any given time-step. The modified multigrid technique is applied to an example problem of a liquid drop vaporizing in a convective gas flow whereby moving grids are used to account for the change in drop size due to vaporization. Problems involving phase change such as the one under consideration, present additional difficulties (associated with the boundary conditions) for multigrid implementation which are also discussed.

Chapter 2

The Mathematical Model

The mathematical model describes the processes of vaporization and combustion of cold single component fuel droplets placed in a hot convective oxidizing flow field. The model includes the conservation equations and the boundary conditions that govern these processes along with the initial conditions used in this study. The governing equations are expressed in a local non-inertial reference frame moving at droplet velocity U_G such that the droplet remains stationary in this reference frame. Since the droplet changes its mass (and thus its size) due to vaporization with time, moving grids are used to capture the interface motion.

2.1 Assumptions

The following assumptions are made in the model:

1. The droplet is assumed to remain spherical in shape implying small Weber numbers $(\rho u^2 d / \sigma)$.
2. Phase equilibrium is assumed to exist at the liquid-gas interface.
3. The gas phase is assumed to follow the ideal gas law.
4. Thermal radiation and Dufour terms in the energy equation and the thermal diffusion term in the concentration equations are negligible.

5. The Mach number is low enough to neglect dissipation terms.
6. There are no external body forces like gravity.

2.2 The Governing Equations

The governing equations are identical in both the gas and liquid phase and are given below.

Space Conservation Law

$$\frac{d}{dt} \int_{\Omega} d\Omega - \int_S \mathbf{v}_b \cdot \mathbf{n} dS = 0. \quad (2.1)$$

Conservation of Mass

$$\frac{d}{dt} \int_{\Omega} \rho d\Omega + \int_S \rho(\mathbf{v} - \mathbf{v}_b) \cdot \mathbf{n} dS = 0 \quad (2.2)$$

where ρ is the fluid density, Ω is the control volume (CV) bounded by a closed surface S , \mathbf{v} is the fluid velocity, \mathbf{v}_b is the velocity of the CV surface and t is time.

Conservation of Momentum

$$\frac{d}{dt} \int_{\Omega} \rho \mathbf{v} d\Omega + \int_S \rho \mathbf{v}(\mathbf{v} - \mathbf{v}_b) \cdot \mathbf{n} dS = \int_S \mathbf{\Gamma} \cdot \mathbf{n} dS - \int_{\Omega} \rho \frac{d\mathbf{U}_g}{dt} d\Omega \quad (2.3)$$

$\mathbf{\Gamma}$ being the stress tensor defined as

$$\mathbf{\Gamma} = -p\delta_{ij} + \tau_{ij} = -p\delta_{ij} + \mu[(\nabla\mathbf{v}) + (\nabla\mathbf{v})^T] \quad (2.4)$$

where p is the pressure, μ the dynamics viscosity and δ_{ij} the Kronecker delta.

The term $\frac{d\mathbf{U}_g}{dt}$ in the gas phase arises because the equations are expressed in a non-inertial reference frame and it will be discussed in Section 2.6. $\frac{d\mathbf{U}_g}{dt} = 0$ in the liquid phase.

Conservation of Energy

$$\begin{aligned} \frac{d}{dt} \int_{\Omega} \rho c_P T d\Omega + \int_S \rho c_P T (\mathbf{v} - \mathbf{v}_b) \cdot \mathbf{n} dS &= \int_S k \nabla T \cdot \mathbf{n} dS + \int_{\Omega} \sum_{i=1}^{N_S} c_{P,m} T \rho D_{i,m} \nabla Y_i d\Omega \\ &- \int_{\Omega} \sum_{i=1}^{N_S} h_i M_i \sum_{k=1}^{N_R} r_{i,k} d\Omega \end{aligned} \quad (2.5)$$

where k is the diffusion coefficient, c_p is the specific heat, $D_{i,m}$ is the diffusion coefficient of species i into the gas mixture, h_i is the specific enthalpy of species i , M_i is the molecular weight of species i and $r_{i,k}$ is the molar rate of creation/destruction of species i in reaction k in the gas phase. In the liquid phase the last two terms of the right hand side of equation 2.5 are zero.

Conservation of Species i

$$\frac{d}{dt} \int_{\Omega} \rho Y_i d\Omega + \int_S \rho Y_i (\mathbf{v} - \mathbf{v}_b) \cdot \mathbf{n} dS = \int_S \rho D_{i,m} \nabla Y_i \cdot \mathbf{n} dS + \int_{\Omega} M_i \sum_{k=1}^{N_R} r_{i,k} d\Omega. \quad (2.6)$$

This equation is not solved in the liquid phase as single component fuel drops are modeled.

2.3 The Boundary Conditions

Boundary and initial conditions for the gas phase corresponding to the sudden injection of a cold droplet into a hot uniform flow field need to be given as well along with zero gradient outflow boundary conditions and liquid/gas interface boundary conditions. At the liquid/gas interface mass, energy and chemical species are conserved. Additionally, tangential velocity, stress and temperature are continuous across the liquid/gas interface and phase equilibrium is assumed to prevail. A schematic of the computational domain identifying the different boundary conditions is shown in Figure 2.1. The lengths are expressed in terms of the droplet diameter D in Figure 2.1.

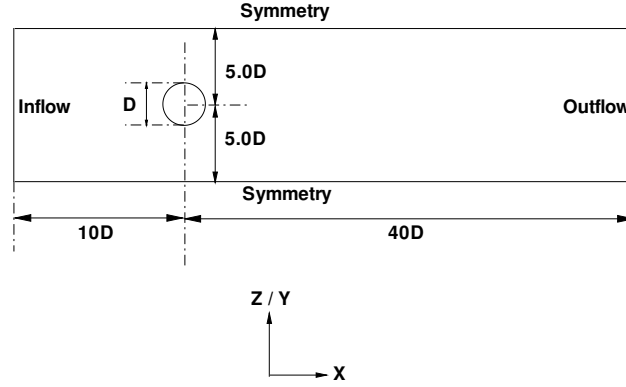


Figure 2.1: Schematic of flow configuration

Continuity of Tangential Velocity: No-Slip Condition

$$(\mathbf{v} \cdot \mathbf{t}_{\mathbf{g}})_{l,int} = (\mathbf{v} \cdot \mathbf{t}_{\mathbf{g}})_{g,int}. \quad (2.7)$$

Continuity of Stress

$$[(\mathbf{\Gamma} \cdot \mathbf{n}) \cdot \mathbf{t}_{\mathbf{g}}]_{l,int} = [(\mathbf{\Gamma} \cdot \mathbf{n}) \cdot \mathbf{t}_{\mathbf{g}}]_{g,int}. \quad (2.8)$$

Continuity of Temperature

$$T_{l,int} = T_{g,int}. \quad (2.9)$$

Conservation of Mass

$$[\rho(\mathbf{v} - \mathbf{v}_b) \cdot \mathbf{n}]_{l,int} = [\rho(\mathbf{v} - \mathbf{v}_b) \cdot \mathbf{n}]_{g,int}. \quad (2.10)$$

Conservation of Energy

$$-(k\nabla T \cdot \mathbf{n})_{l,int} = -(k\nabla T \cdot \mathbf{n})_{g,int} + \dot{m}L_{vap}. \quad (2.11)$$

Conservation of Species

$$\dot{m} = - \left(\frac{\rho D_{fm} \nabla Y_f \cdot \mathbf{n}}{1 - Y_f} \right)_{g,int}. \quad (2.12)$$

Mass Fractions at the Interface: Phase Equilibrium

Phase equilibrium between the fuel vapor and liquid fuel in the droplet is assumed to exist at the interface in order to calculate the partial pressure of the fuel vapor. Fuel mole fraction is determined by the partial pressure of the fuel at the interface temperature

$$X_{f,int} = \frac{P_{f,int}(T_{int})}{P_{g,tot}} \quad (2.13)$$

where $P_{g,tot}$ is the total absolute gas side pressure at the interface. Since in the present incompressible flow (see Chapter 3) formulation only the pressure differences (gauge pressures) have significance (the pressure-correction equation has Neumann boundary conditions, see Ferziger and Perić, 1996) the minimum local pressure in the gas phase, p_{min} , is subtracted from the local pressure and this difference is added to the absolute pressure at infinity, P_∞ , to arrive at the absolute gas pressure. The total absolute gas side pressure at the interface is then given by $P_{g,tot} = (p_{g,int} - p_{min}) + P_\infty$. The absolute partial pressure of the fuel in the

gas-phase is determined using the Antoine equation (Lide 1997)

$$\ln P_{f,int} = A - \frac{B}{T_{int} + C} \quad (2.14)$$

where A , B and C are antonie constants and T_{int} is the liquid temperature at the interface. and the fuel mass fraction is determined from (Aouina *et al.* 2001)

$$Y_{f,int} = \frac{X_{f,int}M_f}{X_{f,int}M_f + (1 - X_{f,int})M_a}. \quad (2.15)$$

The mass fractions of all other species than fuel and air (which assumed to be a mixture of nitrogen and oxygen) is zero at the interface

$$Y_{i \neq f, Nitrogen, Oxygen} = 0 \quad ; \quad i = 1, \dots, N_S \quad (2.16)$$

$$Y_{Oxygen} = 0.24(1 - Y_f) \quad (2.17)$$

$$Y_{Nitrogen} = 0.76(1 - Y_f). \quad (2.18)$$

Although the actual mass fractions of nitrogen and oxygen in air are 0.767 and 0.232 respectively slightly different values stated above were used in the calculation.

Symmetry Boundary Condition

At a symmetry plane (as shown in Figure 2.1) the convective fluxes of all quantities are zero. The normal gradients of velocity components parallel to the symmetry plane, v_p , and of all scalars are zero:

$$\frac{\partial \phi}{\partial n} = 0; \quad \phi = v_p, T, Y_i \quad ; \quad i = 1, N_s. \quad (2.19)$$

Additionally, the normal velocity component at the symmetry plane is zero:

$$\mathbf{v} \cdot \mathbf{n} = 0. \quad (2.20)$$

Inlet Boundary Conditions

Free stream values are prescribed at the inlet boundary (marked Inflow in Figure 2.1) to all variables.

$$\begin{aligned} u &= u_\infty \\ v &= v_\infty \\ w &= w_\infty \\ p &= p_\infty \\ T &= T_\infty \\ Y_i &= Y_{i,\infty}; i = 1, N_s \end{aligned} \quad (2.21)$$

Outlet Boundary Conditions

Zero gradient conditions are specified at the outlet boundary (marked Outflow in Figure 2.1):

$$\frac{\partial \phi}{\partial n} = 0; \quad \phi = u, v, w, c_p T, Y_i; i = 1, N_s. \quad (2.22)$$

Since moving grids are used, mass conservation is enforced by further adjusting the gas-phase velocities at the outlet boundary as described in section 3.2.2.6.

2.4 Initial Conditions

An initial guess is needed to start the numerical solution procedure. This initial guess is provided by initializing all the variables at the beginning of the solution procedure. All variables in the gas phase are initialized with free stream values.

$$\begin{aligned}u &= u_\infty \\v &= v_\infty \\w &= w_\infty \\p &= p_\infty \\T &= T_\infty \\Y_i &= Y_{i,\infty}; i = 1, N_s\end{aligned}\tag{2.23}$$

The following values were used to initialize variables in liquid phase.

$$\begin{aligned}u &= 0 \\v &= 0 \\w &= 0 \\p &= 0 \\T &= T_o \\Y_{i \neq f} &= 0; i = 1, N_s \\Y_f &= 1\end{aligned}\tag{2.24}$$

2.5 Evaluation of Transport Properties

The calculation of transport properties, for both phases, used in the detailed chemistry reacting flow computations is described in the following. Variable properties were used for the gas phase while constant properties were used for the liquid phase.

2.5.1 Gas Phase Properties

The transport properties in the gas phase were evaluated from the kinetic theory of gases (Hirschfelder *et al.*, 1964).

Specific Heat and Specific Enthalpy

The specific heat, $c_{p,i}$, of species, i , in gas phase was calculated from a polynomial fit of the form

$$c_{p,i}(T) = a_1 + a_2T + a_3T^2 + a_4T^3 + a_5T^4 \quad (2.25)$$

where the coefficients a_1, a_2 etc. were taken from *JANAF* tables (Bureau of Standards, 1971). The specific heat of the gas mixture, $c_{p,m}$, was then determined from the specific heats of its constituent species as

$$c_{p,m}(T) = \sum_{i=1}^{N_s} c_{p,i}(T) \cdot Y_i. \quad (2.26)$$

The specific enthalpy, $h_i(T)$, of species, i , was calculated by intergrating the specific heat of species, i , as follows

$$h_i(T) = h_{i,T^o}^o + \int_{T^o}^T c_{p,i}(T) dT \quad (2.27)$$

where h_{i,T^o}^o is the standard enthalpy of formation of species, i , at reference temperature T^o .

Viscosity

The viscosity, μ_i , of species, i , in the gas phase was calculated from Chapman-Enskog theory (see Kee *et al.* 1983) and the viscosity of the gas mixture, μ_m , was evaluated from the viscosities of the constituent species as

$$\mu_m = \frac{1}{2} \left[\sum_{i=1}^{N_s} X_i \mu_i + \left(\sum_{i=1}^{N_s} \frac{X_i}{\mu_i} \right)^{-1} \right]. \quad (2.28)$$

Thermal Conductivity

The thermal conductivity, k_i , of species, i , in the gas phase was calculated from kinetic theory of gases (see Kee *et al.* 1983) and the thermal conductivity of the gas mixture, k_m , was evaluated from the thermal conductivities of the constituent species as

$$k_m = \frac{1}{2} \left[\sum_{i=1}^{N_s} X_i k_i + \left(\sum_{i=1}^{N_s} \frac{X_i}{k_i} \right)^{-1} \right]. \quad (2.29)$$

Mass Diffusion Coefficients

Binary diffusion coefficient, D_{ij} , of species i into species j , was calculated from Chapman-Enskog theory (see Kee *et al.* 1983). The diffusion coefficient of species, i , into the gas mixture $D_{i,m}$, was calculated from the binary diffusion coefficients as follows

$$D_{i,m} = \frac{1 - Y_i}{\sum_{j \neq i} \frac{X_j}{D_{ij}}}. \quad (2.30)$$

Density

The gas phase mixture was assumed to behave as an ideal gas and the ideal gas law was used to calculate the density, ρ_m , of the gas phase mixture.

Property	Value
Density	808.184 kg/m ³
Viscosity	4.76 × 10 ⁻⁴ kg/ms
Thermal Conductivity	0.162 W/mK
Specific Heat	2.684 × 10 ³ J/kgK
Latent Heat of Vaporization	1.0246 × 10 ⁶ J/kgK

Table 2.1: Properties in the liquid phase

$$\rho_m = \frac{PM_m}{RT} \quad (2.31)$$

Vapour Pressure of the Fuel

Antoinies relation (see equation 2.14) was used to determine the vapour pressure of the fuel (ethanol) in the gas phase with the following constants (see Lide 1997)

$$A = 16.1952, B = 3423.52, C = -55.7152 \quad (2.32)$$

which give the partial pressure in kPa.

2.5.2 Liquid Phase Properties

As the variation of liquid properties, with temperature, is not large as compared to gases constant properties were used in the liquid phase. The liquid phase properties used are listed in Table 2.1.

2.6 Evaluation of Forces and Reaction Rates

The total drag force is the contribution of pressure, friction and thrust force (Chiang *et al.* 1990) .

$$F_D = F_{D,p} + F_{D,F} + F_{D,T} \quad (2.33)$$

where

$$F_{D,p} = - \int_S p(\mathbf{I} \cdot \mathbf{n}) \cdot \mathbf{i} dS \quad (2.34)$$

is the pressure drag force

$$F_{D,F} = \int_S (\boldsymbol{\tau} \cdot \mathbf{n}) \cdot \mathbf{i} dS \quad (2.35)$$

is the friction drag force and

$$F_{D,T} = - \int_S [\rho \mathbf{v}(\mathbf{v} - \mathbf{v}_b) \cdot \mathbf{n}] \cdot \mathbf{i} dS \quad (2.36)$$

is the thrust drag force. Thrust drag force arises due to mass loss because of droplet vaporization and is not an external force.

The lift force is evaluated as follows (Kim *et al.* 1993):

$$F_L = - \int_S p(\mathbf{I} \cdot \mathbf{n}) \cdot \mathbf{j} dS + \int_S (\boldsymbol{\tau} \cdot \mathbf{n}) \cdot \mathbf{j} dS - \int_S [\rho \mathbf{v}(\mathbf{v} - \mathbf{v}_b) \cdot \mathbf{n}] \cdot \mathbf{j} dS. \quad (2.37)$$

The drag and lift forces described above include all forces acting on the droplet like the Basset force and Oseen force used in modeling the trajectory of spherical particles.

The term $\int_{\Omega} \frac{d\mathbf{U}_g}{dt} d\Omega$ appears in equation 2.3 because a non-inertial reference frame is used. It is the contribution of the inertial force arising due to the movement of the non-inertial reference frame with respect to an inertial reference frame. It is evaluated as follows (see Haywood 1992):

$$\frac{d\mathbf{U}_g}{dt} = \frac{1}{\int_{\Omega} \rho d\Omega} \left[\sum F - \int_S \rho \mathbf{v}(\mathbf{v} - \mathbf{v}_b) \cdot \mathbf{n} dS - \frac{d}{dt} \int_{\Omega} \rho \mathbf{v} d\Omega \right] \quad (2.38)$$

where $\sum F$ is the sum of all external forces acting on the droplet. For a single droplet, because of problem symmetry only one component (in the main flow direction or \mathbf{i} direction) of this term is non-zero and the equation reduces to

$$\frac{d(\mathbf{U}_G \cdot \mathbf{i})}{dt} = \frac{1}{\int_{\Omega} \rho d\Omega} [F_{D,F} + F_{D,P} + F_{D,T} - \frac{d}{dt} \int_{\Omega} \rho \mathbf{v} \cdot \mathbf{i} d\Omega]. \quad (2.39)$$

When more than one droplet is present, then depending on the spatial arrangement the \mathbf{j} and/or \mathbf{k} direction, symmetry may be lost, and there would be a net force on the droplets in these directions. However, the magnitude of these forces is small (about 15 times smaller in \mathbf{j} direction and 200 times smaller in \mathbf{k} direction as compared to \mathbf{i} direction, see Kim *et al.* 1993) compared to the total drag forces acting in the \mathbf{i} direction. Thus, they are neglected and only the \mathbf{i} direction force contribution to the inertial force term $\frac{d\mathbf{U}_g}{dt}$ is considered even for multiple droplet configurations.

The drag and lift coefficients are determined by non-dimensionalization of the corresponding forces using the projected area of the sphere ($\frac{1}{2}\pi d_o^2$) (Kim *et al.* 1993):

$$C_D = \frac{F_D}{\frac{1}{2}\rho U_{\infty}^2 \pi d_o^2} \quad (2.40)$$

and

$$C_L = \frac{F_L}{\frac{1}{2}\rho U_{\infty}^2 \pi d_o^2}. \quad (2.41)$$

Average Nusselt and Sherwood numbers are defined as follows (see Haywood, 1992):

$$\overline{Nu} = \frac{d}{\int_S k dS} \int_S \frac{k \nabla T \cdot \mathbf{n}}{T_{\infty} - T_{int}} dS \quad (2.42)$$

and

$$\overline{Sh} = \frac{d}{\int_S \rho D_{f,m} dS} \int_S \frac{\rho D_{f,m} \nabla Y_f \cdot \mathbf{n}}{Y_{f,\infty} - Y_{f,int}} dS. \quad (2.43)$$

The term $r_{i,k}$ appearing in equations 2.5 and 2.6 is the molar chemical rate of creation/destruction of species i in reaction k . If the k^{th} reaction is represented by



then $r_{i,k}$ is evaluated as

$$r_{i,k} = \Lambda (\nu''_{i,k} - \nu'_{i,k}) \left[k_{f,k} \prod_{j=1}^{N_R} [C_{j,k}]^{\eta_{j,k}} - k_{b,k} \prod_{j=1}^{N_R} [C_{j,k}]^{\eta'_{j,k}} \right] \quad (2.45)$$

where $\nu'_{i,k}$ and $\nu''_{i,k}$ are the stoichiometric coefficients of species i in reaction k , for the reactants and products respectively, $C_{j,k}$ is the molar concentration of species j in reaction k , $\eta_{j,k}$ is the forward rate exponent and $\eta'_{j,k}$ is the backward rate exponent for species j in given reaction k . Λ is the net effect of third bodies in the reaction rate given by

$$\Lambda = \sum_{j=1}^{N_R} \lambda_{j,k} C_j \quad (2.46)$$

where $\lambda_{j,k}$ is the third body efficiency of species j in reaction k .

The forward rate constants for the r^{th} reaction are determined using the modified Arrhenius expression (Poinot and Veynante, 2001)

$$k_{f,r} = A_{r,f} T^{\beta_r} \exp\left(-\frac{E_{a,r,f}}{RT}\right) \quad (2.47)$$

where A_r is the pre-exponential factor for the reaction, β_r is the dimensionless temperature

exponent and $E_{a,r}$ is the activation energy for the reaction. The backward rate constants are also evaluated using equation 2.47 with the corresponding pre-exponential factor and activation energy for the backward reaction.

Chapter 3

The Numerical Method

This chapter describes the method used to solve the equations presented in Chapter 2. The equations are solved numerically using the FASTEST-3D code (see Durst and Schäfer, 1996 and Perić, 1985). It employs a fully conservative finite volume method for the solution of the flow equations. The salient features of this method are:

- Non-orthogonal boundary fitted block-structured numerical grids,
- colocated arrangement of dependent variables,
- pressure-correction approach of Semi-IMPlicit Pressure Linked Equations (SIMPLE) type (Patankar and Spalding, 1972) for the coupled system of equations,
- strongly implicit Incomplete LU decomposition method (ILU) of Stone (1968) for solving the linear equation systems,
- non-linear multigrid scheme for convergence acceleration,
- moving grids for capturing droplet distortion,
- block-structured grid partitioning for parallelization.

Although large density variations occur in reactive flows due to large temperature differences, the Mach number, $M = u/c$, defined as the ratio of fluid velocity, u , to the velocity of

sound in the medium, c , is always small. For the reactive flow calculations in this study, $u \leq 25$ m/s, $c \geq 776$ m/s and $M \leq 0.04$. As the Mach number, $M \leq 0.3$, the flow can be safely treated with incompressible flow formulation (see Muralidhar and Sundararajan, 1995).

3.1 Discretization of the Partial Differential Equations

The partial differential equations (PDEs) described in Chapter 2 are discretized using a finite volume method as described below.

3.1.1 Discretization in Space

When the conservation equations are applied to each CV to obtain an algebraic equation the following approximations are made (see Ferziger and Perić, 1996):

- Numerical differentiation to approximate the gradients of variables which are required to obtain diffusive fluxes.
- Numerical approximation of the volume and surface integrals for each CV.
- Interpolation of variable values from CV centers to other locations where they are needed for the evaluation of above integrals.

3.1.1.1 Approximation of Surface and Volume Integrals

The surface integrals are approximated, using midpoint rule, as the product of cell face area and the interpolated value of the integrand at cell face center. For example for the eastern face of a CV (see Figure 3.1)

$$\int_{S_e} f dS \approx \bar{F}_e \delta S_e \quad (3.1)$$

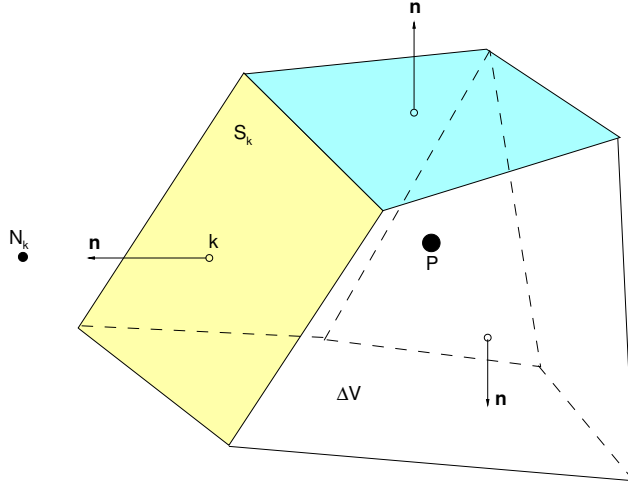


Figure 3.1: Example of a control volume and notation used

where the overbar denotes the interpolated cell face value, f is the component of the convective $(\rho\phi(\mathbf{v} - \mathbf{v}_b) \cdot \mathbf{n})$ or diffusive $(\gamma\nabla\phi \cdot \mathbf{n})$ fluxes in the direction normal to the eastern CV face and δS_e is the area of the eastern CV face. This approximation of the integral is second order accurate provided the interpolated value of the integrand at the cell face \overline{f}_e is second order accurate.

To enhance the diagonal dominance of the coefficient matrix, the convective fluxes are implemented using a deferred correction approach (Khosla and Rubin, 1974), where only the first-order upwind parts of the flux approximations contribute to the coefficient matrix, while the second-order parts are treated explicitly:

$$f = f^l + (f^h - f^l)^{old} \quad (3.2)$$

where f is the convective flux approximation, f^l and f^h are the first-order upwind part and the second-order part of the convective flux and the superscript *old* stand for previous iteration values. When the cell Peclet number, $\rho u \Delta\Omega/k$, is bigger than 10 using an upwind scheme introduces false diffusion (see Patankar, 1980). However, the deferred correction

approach described above ensures that for a converged solution ($f^l = f^{l,old}$) the first-order upwind parts of the convective fluxes cancel each other from the right hand side of equation 3.2 and the convective flux approximation is second-order accurate.

The volume integrals are also evaluated using the midpoint rule and require no additional approximations because all unknowns and fluid properties are stored at the CV center. The CV center value of the integrand is multiplied with the CV volume $\delta\Omega$.

$$\int_{\Omega} f d\Omega \approx f_P \delta\Omega \quad (3.3)$$

where f_P is the value of f at the CV center. The above approximation is also second order accurate.

3.1.1.2 Interpolation Scheme

The value of the integrand at the cell face \overline{f}_e is required in the evaluation of the surface integrals (see equation 3.1). For non-linear convective fluxes Picard iteration approach (see Ferziger and Perić, 1996) is used to linearize, \overline{f}_e , whereby the mass fluxes through the faces are calculated using previous iteration values

$$\overline{f}_e = \int_{S_e} \rho \phi (\mathbf{v} - \mathbf{v}_b) \cdot \mathbf{n} dS \approx \phi_e \int_{S_e} \rho (\mathbf{v} - \mathbf{v}_b) \cdot \mathbf{n} dS = \phi_e m_e. \quad (3.4)$$

This linearization reduces the task to finding the values of the dependent variable, ϕ , at cell faces for the evaluation of f_e . Further, the gradient, in the normal direction, $(\nabla\phi \cdot \mathbf{n})$, of the dependent variable, ϕ , is needed at cell faces for the evaluation of diffusive fluxes. These values are obtained from interpolation. As noted in section 3.1.1.1 the approximations to the surface integrals are second order accurate only as long as the interpolated value of the integrand at the cell face \overline{f}_e is second order accurate. The commonly used linear interpolation scheme (central difference scheme, CDS) is only first order accurate on distorted grids and deteriorates the overall accuracy of an otherwise second order discretization scheme. Thus a multi-dimensional Taylor series expansion based interpolation scheme (Lehnhäuser and

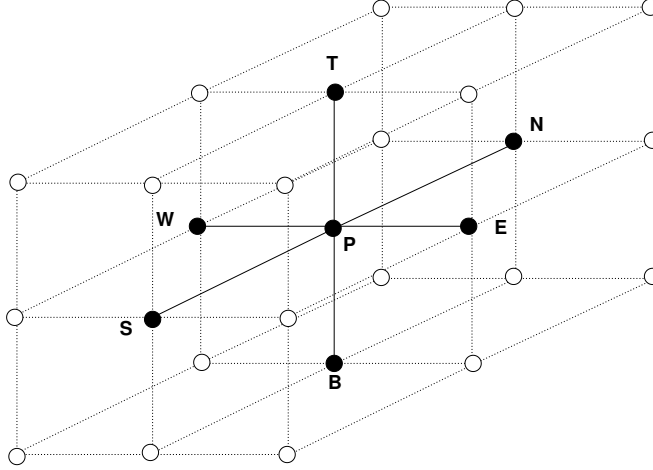


Figure 3.2: Example CV and its neighbours

Schäfer, 2001) is used which preserves second order accuracy on strongly distorted grids while preserving the CDS type sparsity pattern of the computational molecule.

3.1.2 Discretization in Time

For time discretization a fully implicit second-order accurate three-time-levels scheme (see Ferziger and Perić, 1996) is used. This scheme approximates the time derivative at $n + 1$ th level, t_{n+1} , over a time-interval Δt centered around t_{n+1} as

$$\left(\frac{d\phi}{dt}\right)_{n+1} = \frac{3\phi^{n+1} - 4\phi^n + \phi^{n-1}}{2\Delta t} \quad (3.5)$$

where ϕ^n denotes the value of the variable, ϕ , at n^{th} time-level.

Thus the overall solution procedure is second-order accurate in space and time.

3.1.3 Discretized Algebraic Equation System

The spatial domain is subdivided into a finite number of CVs. One algebraic equation per CV is then obtained by applying the conservation equations to each CV and discretizing them. Each algebraic equation involves the contributions from the CV center and from 26 neighboring CVs as shown in Figure 3.2. To reduce the computational complexity only 6 of these neighbouring CVs are treated implicitly and the rest are included in the source term.

$$A_P \phi_P + \sum_{nb} A_{nb} \phi_{nb} = S_P \quad (3.6)$$

where P denotes the center of the CV at which the equation is being discretized and has nb neighboring CVs. The coefficients A_{nb} contain contributions from surface integrals over faces common to the CV centered at P and the corresponding neighbor nb . The coefficient A_P contains contributions from volume integrals (implicitly treated parts of unsteady terms and source terms) in addition to contributions from surface integrals. S_P contains all terms which are treated as known (explicitly treated parts of surface integrals, unsteady terms, and source terms). The source term is linearized into an implicit part and an explicit part as suggested by Patankar (1980). For the solution domain as a whole, the system of M such algebraic equations, where M is the total number of control volumes, can be written in matrix notation as

$$[A]\{\phi\} = \{S\} \quad (3.7)$$

where $[A]$ is a $M \times M$ coefficient matrix, $\{\phi\}$ is the column matrix of M dependent variable unknowns and $\{S\}$ is a similar column matrix containing known source terms. The coefficients matrix $[A]$ depends on geometrical quantities, fluid properties, and the dependent variable values themselves. One such matrix equation is obtained for each dependent variable. Since the systems of equations (matrix equations of all the dependent variables put together) is non-linear, an iterative solution method is used in which the coupled equations are solved in a segregated manner, solving for each variable in turn treating all other variables other than

the one being solved as known. Furthermore, the coefficient matrix is treated as constant during “inner iterations” and updated during every “outer iteration”. The linearized system of equations, thus obtained for each “inner iteration”, is solved using the strongly implicit procedure (SIP) of Stone (1968).

3.2 The Numerical Grid

This section describes the numerical grid, used in the calculations, and other issues associated with the grid and the solution method.

3.2.1 Grid Generation

Non-orthogonal body fitted block structured grids made-up of hexahedral control volumes are used for all calculations. The grids are generated using the commercial package *ANSYS ICEMCFD - HEXA* (see ICEM CFD Engineering). An O-grid (see Thompson *et al.* 1995) is generated in the droplet interior. The height of the first layer of CVs in the gas-phase adjacent to the droplet is about 1% of initial droplet radius and the grid stretching factor between adjacent layers is 1.2. Cell volumes are calculated by decomposing each hexahedral CV into eight tetrahedra as suggested by Kordula and Vinokur (1983). The calculation of swept volumes (in equation 3.9) is also done in the same fashion by decomposing the hexahedra formed by a cell-face as it moves from its old position to its new position (Ferziger and Perić, 1996).

3.2.2 Effect of Grid Movement

As the droplet vaporizes it loses mass to its surroundings and its radius keeps decreasing with time. Moving grids are used to capture the motion of the droplet surface whereby the grid is fitted to the droplet surface and follows its motion.

3.2.2.1 Discretization of Space Conservation Law

When moving grids are used the Space Conservation Law (SCL) given by equation 2.1 must be satisfied otherwise artificial mass sources are introduced which may accumulate and spoil the solution (Demirdžić and Perić, 1988). Two approaches suggested by Demirdžić and Perić (1988,1990) to satisfy the SCL is either to calculate the grid velocities, \mathbf{v}_b , such that the SCL is satisfied or alternatively, to define the volume fluxes such that the SCL is satisfied. The latter approach is used here, as it is more convenient in three dimensions. Using the time discretization method described above the SCL equation can be written as follows:

$$\frac{3\Delta\Omega^{n+1} - 4\Delta\Omega^n + \Delta\Omega^{n-1}}{2\Delta t} = \sum_k [(\mathbf{v}_b \cdot \mathbf{n})_k S_k]^{n+1}. \quad (3.8)$$

The difference between the CV volumes at consecutive time-levels can be decomposed as follows:

$$\Delta\Omega^{n+1} - \Delta\Omega^n = \sum_k \delta\Omega_k^n \quad (3.9)$$

where $\delta\Omega_k^n$ is the volume swept by the k^{th} CV face while moving from its old position to its new position. Substitution of equation 3.9 into equation 3.8 gives

$$\frac{\sum_k (3\delta\Omega_k^n - \delta\Omega_k^{n-1})}{2\Delta t} = \sum_k [(\mathbf{v}_b \cdot \mathbf{n})_k S_k]^{n+1}. \quad (3.10)$$

If the volume swept by each face, during one time-interval, $\delta\Omega_k$, is calculated using the grid positions at two consecutive time levels and the volume fluxes, $[(\mathbf{v}_b \cdot \mathbf{n})_k S_k]^{n+1}$, are defined as

$$[(\mathbf{v}_b \cdot \mathbf{n})_k S_k]^{n+1} = \frac{(3\delta\Omega_k^n - \delta\Omega_k^{n-1})}{2\Delta t} \quad (3.11)$$

then the SCL is identically satisfied.

3.2.2.2 Generalization of Space Conservation Law

If the Space Conservation Law (SCL) is not satisfied, on moving grids, errors in the form of artificial mass sources are introduced (Demirdžić and Perić, 1988). Nevertheless, SCL is just one equation out of a set of conservation equations which have to be satisfied on moving grids. Even though SCL is satisfied, by neglecting other equations of this set, errors in the form of artificial momentum sources and scalar sources may still accumulate on moving grids, as described below, and spoil the solution.

3.2.2.3 Grid Velocity as a Counterbalance for Unsteady Term

On stationary grids, the unsteady terms in the governing equations (equations 2.2, 2.3, 2.5, 2.6) are zero if the variable values do not change with time. However, on moving grids, the volume of a CV changes with time and thus the unsteady terms in the governing equations are not zero even when the variables do not change with time. The role of the additional contribution, to the convective fluxes, from moving grids, is to make this unsteady term zero as explained below.

Consider the equation for the conservation of mass, for a constant density fluid, on stationary grids

$$\rho \left[\frac{d}{dt} \int_{\Omega} d\Omega + \int_S \mathbf{v} \cdot \mathbf{n} dS \right] = 0. \quad (3.12)$$

For a stagnant fluid, in the absence of any fluid motion, $\mathbf{v} = 0$, further, on stationary grids, the volume of a CV does not change with time, $\frac{d\Omega}{dt} = 0$, and equation 3.12 is identically satisfied:

$$\underbrace{\frac{d}{dt} \int_{\Omega} d\Omega}_{=0} + \underbrace{\int_S \mathbf{v} \cdot \mathbf{n} dS}_{=0} = 0. \quad (3.13)$$

Consider the equation for the conservation of mass, for a constant density fluid, on a grid moving with a non-zero velocity

$$\rho \left[\frac{d}{dt} \int_{\Omega} d\Omega + \int_S (\mathbf{v} - \mathbf{v}_b) \cdot \mathbf{n} dS \right] = 0. \quad (3.14)$$

For a stagnant fluid, in the absence of any fluid motion, $\mathbf{v} = 0$, further, since the grid is moving with non-zero velocity, $\mathbf{v}_b \neq 0$, and the volume of a CV will change with time, $\frac{d\Omega}{dt} \neq 0$, and equation 3.14 reduces to

$$\underbrace{\frac{d}{dt} \int_{\Omega} d\Omega}_{\neq 0} - \underbrace{\int_S \mathbf{v}_b \cdot \mathbf{n} dS}_{\neq 0} = 0. \quad (3.15)$$

If mass conservation has to be satisfied then the grid velocities have to be such that they cancel the unsteady term in equation 3.15 and the Space Conservation Law (equation 2.1) is recovered.

A similar equation can be derived for the general case of any scalar quantity, ϕ , in a convective and diffusive flow as follows. The equation for the conservation of a scalar, for a variable density fluid on a stationary grid, is given by

$$\frac{d}{dt} \int_{\Omega} \rho \phi d\Omega + \int_S \rho \phi \mathbf{v} \cdot \mathbf{n} dS = \int_S \gamma \nabla \phi \cdot \mathbf{n} dS + \int_{\Omega} q_{\phi} d\Omega \quad (3.16)$$

where γ is the exchange coefficient and q_{ϕ} could be either source or sink or both of ϕ . By taking the convective term to the right hand side equation 3.16 becomes

$$\frac{d}{dt} \int_{\Omega} \rho \phi d\Omega = \int_S \gamma \nabla \phi \cdot \mathbf{n} dS - \int_S \rho \phi \mathbf{v} \cdot \mathbf{n} dS + \int_{\Omega} q_{\phi} d\Omega. \quad (3.17)$$

By applying Gauss's divergence theorem to express the surface integrals as volume integrals, equation 3.17 becomes

$$\frac{d}{dt} \int_{\Omega} \rho \phi d\Omega = \int_{\Omega} \nabla \cdot (\gamma \nabla \phi) d\Omega - \int_{\Omega} \nabla \cdot (\rho \phi \mathbf{v}) d\Omega + \int_{\Omega} q_{\phi} d\Omega = \int_{\Omega} S_{\phi} d\Omega \quad (3.18)$$

where $S_{\phi} = \nabla \cdot (\gamma \nabla \phi - \rho \phi \mathbf{v}) + q_{\phi}$. On a stationary grid, $\frac{d\Omega}{dt} = 0$, the unsteady term becomes

$$\frac{d}{dt} \int_{\Omega} \rho \phi d\Omega = \left(\int_{\Omega} d\Omega \right) \frac{d(\rho \phi)}{dt}. \quad (3.19)$$

Thus equation 3.18 can be written as:

$$\left(\int_{\Omega} d\Omega \right) \frac{d(\rho \phi)}{dt} = \int_{\Omega} S_{\phi} d\Omega \quad (3.20)$$

which gives the rate of change of the quantity, $\rho \phi$, as:

$$\frac{d(\rho \phi)}{dt} = \frac{\int_{\Omega} S_{\phi} d\Omega}{\int_{\Omega} d\Omega}. \quad (3.21)$$

Assuming that the same flow, as the one above on stationary grids, is now being solved on moving grids the equation for the conservation of a scalar for a fluid, on a grid moving with a non-zero velocity, is given by

$$\frac{d}{dt} \int_{\Omega} \rho \phi d\Omega_M + \int_S \rho \phi (\mathbf{v} - \mathbf{v}_b) \cdot \mathbf{n} dS_M = \int_S \Gamma \nabla \phi \cdot \mathbf{n} dS_M + \int_{\Omega} q_{\phi} d\Omega_M \quad (3.22)$$

where the subscript M refers to a moving grid. By applying Gauss divergence theorem as

above, equation 3.22 can be written as

$$\frac{d}{dt} \int_{\Omega} \rho \phi d\Omega_M - \int_S \rho \phi \mathbf{v}_b \cdot \mathbf{n} dS_M = \int_{\Omega} S_{\phi} d\Omega_M. \quad (3.23)$$

The quantity, S_{ϕ} , at any given point in the flow field, is a property of the vector (velocity) and scalar fields under consideration, and thus is the same on both moving and stationary grids. For example, the gradient of a vector field is a property of the vector field and at any given point is equal to the derivative, of the particular vector field under consideration, in direction of the maximum rate of change of the vector field at that point. Hence the gradient is independent of the coordinate system used for its evaluation. Since the same flow, as the one on stationary grids, is being considered, the rate of change of the quantity, $\rho\phi$, should be independent of the grid velocity, \mathbf{v}_b , and should be the same as that on a stationary grid, and thus it is given by an expression analogous to equation 3.21 as:

$$\frac{d(\rho\phi)}{dt} = \frac{\int_{\Omega} S_{\phi} d\Omega_M}{\int_{\Omega} d\Omega_M}. \quad (3.24)$$

Comparing equation 3.23 with equation 3.24 shows that, for the rate of increase of the quantity, $\rho\phi$, on moving grids, to be the same as that on stationary grids, the following relation should be satisfied

$$\frac{d}{dt} \int_{\Omega} \rho \phi d\Omega_M - \int_S \rho \phi \mathbf{v}_b \cdot \mathbf{n} dS_M = \left(\int_{\Omega} d\Omega_M \right) \frac{d(\rho\phi)}{dt}. \quad (3.25)$$

Failure to satisfy this relation can introduce artificial sources or sinks in equation 3.24 and could lead to an erroneous value of $\frac{d(\rho\phi)}{dt}$. The space conservation law can be shown to be a special case of equation 3.25 as follows. The equation corresponding to the conservation of mass is obtained by substituting, $\phi = 1$, in the above equations for a general scalar, in which

case equation 3.25 is given by

$$\frac{d}{dt} \int_{\Omega} \rho d\Omega_M - \int_S \rho \mathbf{v}_b \cdot \mathbf{n} dS_M = \left(\int_{\Omega} d\Omega_M \right) \frac{d\rho}{dt}. \quad (3.26)$$

Further, for a constant density fluid, equation 3.26 becomes

$$\frac{d}{dt} \int_{\Omega} d\Omega_M - \int_S \mathbf{v}_b \cdot \mathbf{n} dS_M = 0 \quad (3.27)$$

which is the Space Conservation Law (equation 2.1).

It can be shown that equation 3.25 holds for velocities too, as follows. The equation for the conservation of momentum for a fluid in the absence of gravity, on a grid moving with a non-zero velocity, can be written as:

$$\frac{d}{dt} \int_{\Omega} \rho \mathbf{v} d\Omega_M - \int_S \rho \mathbf{v} \mathbf{v}_b \cdot \mathbf{n} dS_M = \int_{\Omega} S_{\mathbf{v}} d\Omega_M \quad (3.28)$$

where the subscript M refers to a moving grid and $S_{\mathbf{v}} = \nabla \cdot (\mathbf{\Gamma} - \rho \mathbf{v} \mathbf{v})$, $\mathbf{\Gamma}$ being the stress tensor. The quantity, $S_{\mathbf{v}}$, at any given point in the flow field, is a property of the vector (velocity) and scalar (pressure and temperature) fields under consideration and is same on both moving and stationary grids (assuming that the same flow is being solved for on both grids). Equation 3.25 can be derived, for $\phi = \mathbf{v}$, following the same arguments as above from equation 3.28 and its counterpart on stationary grids.

Thus, on moving grids, there is a conservation equation corresponding to each governing equation, which has to be satisfied. When one of these conservation equations is not satisfied artificial sources or sinks may accumulate, in the corresponding governing equation, and spoil the solution.

3.2.2.4 No Unique Grid Velocity

As discussed in section 3.2.2.3, on moving grids, equations 3.25 have to be satisfied simultaneously for all conserved variables in the flow under consideration.

$$\frac{d}{dt} \int_{\Omega} \rho \phi d\Omega - \int_S \rho \phi \mathbf{v}_b \cdot \mathbf{n} dS = \left(\int_{\Omega} d\Omega \right) \frac{d(\rho \phi)}{dt} ; \phi = 1, u, v, w, c_p T, Y_i \quad (3.29)$$

where ϕ is 1 for the continuity equation, \mathbf{v} for the momentum equation, $c_p T$ for the energy equation and Y_i for the mass fraction equation.

However, since ϕ can take arbitrary values (at any given point it can be any one of 1, u , v , w , $c_p T$ or Y_i depending on the equation) a unique grid velocity, \mathbf{v}_b , which satisfies these equations simultaneously cannot exist. The concept that there exists, at each grid-point, a unique grid velocity and thus a unique mass flux contribution from moving grids which is the same for all the governing equations has to be abandoned. Instead, the convective flux contribution from moving grids, has to be calculated from equations 3.25 where ϕ takes a value depending upon the governing equation to which it contributes.

The convective flux contribution from moving grids can be directly calculated from equation 3.29 as follows:

$$\int_S \rho \phi \mathbf{v}_b \cdot \mathbf{n} dS = \frac{d}{dt} \int_{\Omega} \rho \phi d\Omega - \left(\int_{\Omega} d\Omega \right) \frac{d(\rho \phi)}{dt} ; \phi = 1, u, v, w, c_p T, Y_i. \quad (3.30)$$

3.2.2.5 Effect of Grid Movement on the Pressure-Correction Equation

If the continuity equation (equation 2.2) is discretized in a manner consistent with the SCL equation then, for incompressible flows, the unsteady term and the contribution of the grid movement to the mass fluxes cancel each other

$$\frac{d}{dt} \int_{\Omega} \rho d\Omega + \int_S \rho (\mathbf{v} - \mathbf{v}_b) \cdot \mathbf{n} dS = \rho \underbrace{\left[\frac{d}{dt} \int_{\Omega} d\Omega - \int_S \mathbf{v}_b \cdot \mathbf{n} dS \right]}_{SCL} + \int_S \rho \mathbf{v} \cdot \mathbf{n} dS \quad (3.31)$$

and the continuity equation reduces to

$$\int_S \rho \mathbf{v} \cdot \mathbf{n} dS = 0 \quad (3.32)$$

which is the same as the continuity equation on stationary grids for incompressible flows. Thus for present incompressible flow formulation grid movement does not effect the pressure-correction equation.

3.2.2.6 Adjustment of Mass Flux at Outflow

Apart from the mass inflow at the inlet boundary there is a net mass flux into the gas-phase due to the vaporization of the droplet and due to mass flux caused by the movement of the boundaries of the gas-phase computational domain. However, the pressure-correction equation cannot ensure a net conservation of mass over the computational domain because as seen above for incompressible flows the continuity equation (equation 3.32) does not involve grid velocities (or equivalently the mass flux caused by the grid movement). Thus mass conservation has to be enforced at the boundaries of the computational domain. This is done by adjusting the net mass outflow to be equal to the net mass inflow as follows. The total mass inflow m_{in} into the computational domain is calculated by summing up the mass flux at the inlet boundary and mass flux due to the movement of the gas-phase domain boundaries. Similarly, the total mass outflow m_{out} is calculated by summing up the mass flux at the outlet. Then the velocities at the outlet boundary are adjusted such that the difference between total mass inflow and total mass outflow, $m_{in} - m_{out}$, is distributed in a weighted manner (corresponding to the profile of m_{out}) at the outflow boundary.

Mass is conserved, in the present study, in the liquid-phase because the rate of decrease of droplet volume is calculated from the rate of evaporated mass (see section 3.4.2) and thus the net mass outflow, due to vaporization, from the liquid-phase computational domain is equal to the net mass inflow, due to the movement of the liquid-phase boundaries.

3.2.3 The Multigrid Technique

The full approximation scheme (FAS) multigrid method used in the thesis is described below. In this scheme the full approximation to the fine-grid solution is computed on coarse grids. On a given grid, with spacing h , the intermediate solution to equation 3.7, obtained after m outer iterations, satisfies the following equation

$$[A_h^m]\{\phi_h^m\} - \{S_h^m\} = \{R_h^m\} \quad (3.33)$$

where $\{R_h^m\}$ is the residual vector after m iterations. This solution is improved (by reducing low frequency errors) by iterating on a coarser grid with spacing $2h$. The variables, ϕ_h^m , and residuals, R_h^m , on the fine grid (with spacing h) are transferred to the coarse grid (with spacing $2h$) by a suitable restriction operator

$$\tilde{\phi}_{2h} = I_h^{2h} \phi_h^m \quad (3.34)$$

where I_h^{2h} is the restriction operator and $\tilde{\phi}_{2h}$ are the restricted variables on the coarse grid. The coefficient matrix, $[\tilde{A}_{2h}]$, and the source term, $\{\tilde{S}_{2h}\}$, on the coarse grid are then calculated as usual using the restricted variables, $\tilde{\phi}_{2h}$, and other quantities based on restricted fine grid solution. The equations which are solved on the coarse grid provide a correction to the fine-grid solution. Thus, to ensure that equations on the coarse grid are identically satisfied when the residuals on the fine grid are zero, a correction is added to them

$$[\hat{A}_{2h}]\{\hat{\phi}_{2h}\} - \{\hat{S}_{2h}\} = [\tilde{A}_{2h}]\{\tilde{\phi}_{2h}\} - \{\tilde{S}_{2h}\} - \{\tilde{R}_{2h}\} \quad (3.35)$$

where $\hat{\phi}_{2h}$ is the full approximation to be computed. The coarse grid coefficient matrix, $[\hat{A}_{2h}]$, and source term, $\{\hat{S}_{2h}\}$, are based on $\hat{\phi}_{2h}$. Initially, for the first coarse grid iteration, $\hat{A}_{2h} = \tilde{A}_{2h}$, $\hat{S}_{2h} = \tilde{S}_{2h}$ and $\hat{\phi}_{2h} = \tilde{\phi}_{2h}$. The first two terms on the right hand side of equation 3.35 constitute the correction term. If the fine grid residual is zero, the coarse grid equation (equation 3.35) will be identically satisfied and the coarse grid approximation

will not change from its initial value, $\hat{\phi}_{2h} = \tilde{\phi}_{2h}$. For non-zero fine grid residuals the coarse grid approximation, $\hat{\phi}_{2h}$, will change from its initial value, $\tilde{\phi}_{2h}$, and after some iterations the coarse grid approximation is used to calculate the correction by which $\tilde{\phi}_{2h}$ has improved

$$\phi'_{2h} = \hat{\phi}_{2h} - \tilde{\phi}_{2h}. \quad (3.36)$$

This correction is prolonged from the coarse grid to the fine grid using an appropriate prolongation operator

$$\phi'_h = I_{2h}^h \phi'_{2h} \quad (3.37)$$

where I_{2h}^h is the prolongation operator and the fine grid solution, ϕ_h^m , is updated by adding the correction, ϕ'_h , to it. Usually more than two grid levels are used, starting at the finest grid level the above described procedure is recursively repeated to move through the grids until the coarsest grid is reached (restriction) and then up again until the the finest grid level is reached (prolongation). This strategy of moving through the grid levels constitutes a *V-cycle*. A few such cycles are carried out at each time step until the convergence criteria are satisfied. Trilinear interpolation (see Press *et al.* 1992) is used for restriction and prolongation of variable values. The restricted fine-grid residuals (and mass fluxes through CV faces) on the coarse grid are the sum of the residuals (and the mass fluxes through CV faces) of the corresponding fine grid CVs. The mass fluxes on the coarse grid are corrected by using the difference, $\hat{u}_i - \tilde{u}_i$. If the fine grid mass fluxes satisfy the continuity equation so will the initial coarse grid mass fluxes and for a converged fine grid solution ($\hat{u}_i = \tilde{u}_i$) the correction to the coarse grid mass fluxes will be zero. Since the pressure source term is linear, the coarse-grid pressure variable becomes, $p' = \hat{p} - \tilde{p}$, and initially the pressure variable on the coarse grid starts with zero ($\hat{p} = \tilde{p}$ initially). Thus pressure is not restricted to the coarse grid, instead the coarse grid pressure-correction equation gives a correction for the fine grid pressure correction. Additionally, care must be taken that boundary conditions are treated in a consistent manner on all grids.

3.2.3.1 Application of Multigrid Technique to Droplet Vaporization

Numerical simulation of droplet vaporization and ignition is a computationally intensive problem often tractable only on supercomputers. Convergence acceleration techniques like multigrids, if applied to this problem, can offer large savings of computational resources. One possible approach for implementing multigrid technique on moving grids is to keep the grid distortion constant during the multigrid cycles. To be more specific at each time step the grid is distorted and iterations are carried out, which may include multigrid cycles, without further distortion until convergence (one cycle) and then the grid distortion is updated and the process is repeated again. A few such cycles can be performed during each time step. This is not very attractive for the problem being studied here since the grid distortion depends strongly on the flow field and evolves dynamically during the solution and thus keeps changing from one iteration to the next unless convergence is obtained.

The multigrid technique described above is applied to the problem of droplet vaporization and combustion with a few modifications. These modifications account for the grid movement, during multigrid cycles, associated with droplet vaporization and for the consistent treatment of the interface boundary conditions which involve gradients on both sides of the gas-liquid interface.

3.2.3.2 Treatment of Secondary Mass Flow due to Grid Movement

In the sequential decoupled solution method adopted here, the convective fluxes are usually linearized using the Picard iteration approach as described by equation 3.4 in section 3.1.1.2. Usually when using this method on stationary grids mass fluxes across CV boundaries are calculated at the beginning of each iteration (using values from the previous iteration) and these mass fluxes are used for assembling the pressure-correction equation. These mass fluxes are then corrected after the solution of pressure-correction equation and the corrected mass fluxes are used for the discretization of the convective fluxes in momentum and scalar transport equations.

However, on moving grids the motion of CV boundaries leads to a secondary mass flow and thus the mass fluxes across the CV boundaries have a contribution from the grid movement, $-\int_S \rho \mathbf{v}_b \cdot \mathbf{n} dS$, in addition to the mass flow due to the bulk motion of the fluid, $\int_S \rho \mathbf{v} \cdot \mathbf{n} dS$, in equations 2.2, 2.3, 2.5 and 2.6. Since, for incompressible flows, the pressure-correction equation remains unchanged due to grid movement (i.e. does not involve the secondary mass flow contribution from the grid movement to the mass fluxes, see section 3.2.2.1) the following practice is usually adopted (Demirdžić and Perić, 1990). At the beginning of each iteration mass fluxes are calculated using only the mass flow due to bulk fluid motion, $\int_S \rho \mathbf{v} \cdot \mathbf{n} dS$, to assemble the pressure correction equation and after the solution of the pressure-correction equation and subsequent correction of mass fluxes, the secondary mass flow contribution from the grid movement, $-\int_S \rho \mathbf{v}_b \cdot \mathbf{n} dS$, is added to the corrected mass fluxes so that when they are used for the discretization of convective fluxes in momentum and scalar transport equations the contribution from the grid movement is included.

The above mentioned practice of adding the secondary mass flow contribution from the grid movement, $-\int_S \rho \mathbf{v}_b \cdot \mathbf{n} dS$, to the corrected mass fluxes on moving grids entails caution when multigrid technique is used. In the multigrid procedure the mass fluxes on the coarse grid are not directly calculated but instead are obtained by restricting the fine grid mass fluxes (from the previous iteration) to the coarse grid, by summing up the mass fluxes through all the fine grid CV faces making up the coarse grid CV face. The fine grid mass fluxes and thus the restricted mass fluxes will have the secondary mass flow contribution from the grid movement ($-\int_S \rho \mathbf{v}_b \cdot \mathbf{n} dS$). While assembling the pressure-correction equation on the coarse grid, caution must be exercised to make sure that the restricted mass fluxes thus obtained do not include the secondary mass flow contribution from the grid movement ($-\int_S \rho \mathbf{v}_b \cdot \mathbf{n} dS$), however, while discretizing convective fluxes in the momentum and scalar transport equations the corrected restricted mass fluxes (obtained after the solution of the pressure-correction equation) should include the secondary mass flow contribution from the grid movement ($-\int_S \rho \mathbf{v}_b \cdot \mathbf{n} dS$). If the secondary mass flow contribution from the grid movement ($-\int_S \rho \mathbf{v}_b \cdot \mathbf{n} dS$) is added to the source term instead (rather than to the mass

fluxes) then the procedure is identical to that on a stationary grid in the following sense. The fine grid mass fluxes can be directly restricted and the restricted mass fluxes can be used to assemble the pressure-correction equation. The convective fluxes in the momentum and scalar transport equations can then be discretized using the corrected restricted mass fluxes obtained after the solution of the pressure-correction equation.

3.2.3.3 Change in Geometry due to Grid Movement

Grid coarsening effects the approximation of the underlying geometry. For example, in a two-dimensional plane, if a n -sided regular polygon is used to approximate a circle, then the errors in the calculation of its surface area depends on n . The errors in calculated surface area can be decreased by increasing n . Since the calculation of grid distortion depends on the properties of the underlying geometry (in this study the volume and surface area of the droplets in equation 3.48) a small difference in the approximation of such properties, between the coarse and fine grids, can cause the grid distortion calculated on the coarse grid, using initial (restricted) variable values, to be different from the one calculated on fine grid even for a converged solution. Further for a non-converged solution the grid distortion changes for each iteration of the restriction cycle and the underlying geometrical properties (like the interpolation factors used to determine cell face values) keep changing from their initial value. To ensure that a converged fine grid solution is not changed in case of small differences in grid distortion between the fine and coarse grids, the coefficient matrix, $[\tilde{A}_{2h}]$, and the source term, $\{\tilde{S}_{2h}\}$, in equation 3.35 are updated to reflect the change in grid distortion only. Thus for each iteration of the restriction cycle the coefficient matrix, $[\tilde{A}_{2h}]$, and the source term, $\{\tilde{S}_{2h}\}$, are recalculated using the restricted values of velocities, pressures, mass fluxes, temperatures, concentrations etc. in such a way that, $[\tilde{A}_{2h}]$ and $\{\tilde{S}_{2h}\}$, differ from their initial value only because of the change in the underlying geometry if any.

This method will ensure that if the restricted fine grid residuals, $\{\tilde{R}_{2h}\}$, in equation 3.35 are zero, then during any iteration of the restriction cycle, $\hat{\phi}_{2h} = \tilde{\phi}_{2h}$, $[\hat{A}_{2h}] = [\tilde{A}_{2h}]$, $\{\hat{S}_{2h}\} = \{\tilde{S}_{2h}\}$, and the coarse grid approximation will not change from its restricted value even if the

grid distortions on the coarse and fine grids are different from each other.

Further, while prolonging the corrections from the coarse grid to the fine grid the interpolation factors corresponding to the the first iteration of the restriction cycle are used. If the solution on a grid with spacing, h , is restricted to a coarser grid with spacing, $2h$, and after a few relaxation sweeps the coarse grid spacing changes from $2h$ to $2h'$ then the correction to the fine grid solution is prolonged from $2h$ to h neglecting the change in coarse grid spacing during the restriction cycle.

This prolongation from $2h$ to h will ensure that small differences in calculated values of grid distortion between the fine and coarse grids will not change a converged value of grid distortion on the fine grid.

3.2.3.4 Treatment of Interface Boundary Conditions

Since the boundary conditions at the interface of the droplet and the gas phase involve gradients (see for example equation 2.8) care must be taken to avoid inconsistency on coarser grids. The reason for possible inconsistency is the same as that for the boundary conditions at the symmetry plane (which also involve gradients) and can arise because, in general, a restricted variable, $\tilde{\phi}$, will have an arbitrary gradient at the boundary and thus will not satisfy either the zero gradient condition at the symmetry plane, or, for example, the continuity of stress condition at the interface. Thus it must be ensured that the restricted variables, $\tilde{\phi}$, at the interface satisfy the boundary conditions by applying boundary conditions to $\tilde{\phi}$. This can be easily done for the velocity boundary conditions, however, the coupled nature of the conservation of energy boundary condition at the interface poses additional problems. The velocity boundary conditions (equations 2.7 and 2.8) are not coupled to the mass flux due to vaporization since, \dot{m} , does not appear in equations 2.7 and 2.8. However, \dot{m} , appears in the conservation of energy boundary condition (equation 2.11) .

In a problem involving phase change, such as the one under consideration, the rate of change of mass undergoing phase change (and thus the grid movement) is coupled to the interface temperature distribution. This is a two-way coupling in which the interface temperature dis-

tribution depends on the rate of mass undergoing phase change which in turn depends on the interface temperature distribution. For the droplet vaporization problem under consideration this coupling is brought through by the conservation of energy condition (involving rate of mass vaporization and temperature distribution at the interface) together with the conditions of conservation of species (involving fuel concentration distribution at the interface) and of phase equilibrium (involving fuel concentration as well as temperature distribution at the interface) which are implemented as boundary conditions at the interface (equations 2.11, 2.12 and 2.13) and must always be satisfied. Owing to this coupling a given grid distortion (or rate of mass vaporization) corresponds to a specific interface temperature distribution and any change in the former will cause a change in the latter and vice-versa. Ensuring that the boundary condition for the conservation of energy (equation 2.11) holds at the interface on the coarse grid for the restricted variables, $\tilde{\phi}$, requires the determination of a restricted interface temperature distribution which along with the corresponding grid distortion predicted for this interface temperature distribution satisfies this boundary condition. Determination of such an interface temperature distribution involves the simultaneous solution of the equation of energy conservation together with equations of mass conservation and phase equilibrium at the interface (equations 2.11, 2.12 and 2.13). An iterative solution procedure based on bisection method is used to solve these equations for the initial restricted interface temperature distribution on the coarse grid. In the algorithm for the bisection method the upper and lower limits of temperature are determined by the initial droplet temperature and the liquid fuel boiling temperature respectively. An initial estimate of the interface temperature is iteratively improved until equations 2.11, 2.12 and 2.13 are simultaneously satisfied.

3.2.3.5 Evaluation of Pressure during Multigrid Restriction Cycle

During the multigrid restriction cycle, the fine grid pressure, p , is not restricted to the coarse grid but instead the fine grid pressure correction, $p' = \hat{p} - \tilde{p}$, is directly used (see section 3.2.3). Determination of fuel mass fraction at the interface requires the evaluation of fuel mole fraction which is determined by assuming phase equilibrium to exist at the

interface. Evaluation of fuel mole fraction in the gas phase at the interface requires the value of pressure at that point (equation 2.13). On coarse grids, equation 2.13 requires the coarse grid approximation of pressure, \hat{p} , at a point. Thus in order to calculate the fuel mole fraction (and mass fraction) on coarse grid during restriction cycle the restricted pressure, \tilde{p} , is determined and the pressure at a point is evaluated as $\hat{p} = p' + \tilde{p}$.

3.3 The Pressure-Correction Equation

Since there is no obvious equation for calculating pressure an equation for pressure-correction is derived by imposing the continuity constraint. The pressure-correction equation is constructed from the discretized momentum and continuity equations using a modified variant of the SIMPLE algorithm. On non-orthogonal grids with a colocated variable arrangement the modified algorithm avoids pressure-velocity decoupling. The algorithm is briefly described in the following and more details can be found in Ferziger and Perić (1996). For a given outer iteration, during which the coefficient and source matrices are updated, the discretized equations for velocities are of the following form

$$A_P^{u_i} u_{i,p}^{m*} + \sum_{nb} A_{nb}^{u_i} u_{i,l}^{m*} = S_{u_i}^{m-1} - \left(\frac{\delta p^{m-1}}{\delta x_i} \right)_P \quad (3.38)$$

where u_i^{m*} is the current estimate of the solution, m is the counter for outer iterations and $S_{u_i}^{m-1}$ is the source term which is explicitly calculated. The pressure p^{m-1} and velocities u_i^{m*} calculated from equation 3.38 are provisional values which do not satisfy the continuity equation and a correction is added to them.

$$p^m = p^{m-1} + p' \quad (3.39)$$

$$u_i^m = u_i^{m*} + u_i' \quad (3.40)$$

In the original SIMPLE algorithm velocity-correction is expressed in terms of the gradient of the pressure-correction

$$u'_{i,P} = -\frac{1}{A_P^{u_i}} \left(\frac{\delta p'}{\delta x_i} \right)_P \quad (3.41)$$

and the pressure-correction equation is derived from the continuity constraint which states that the net mass flux into each CV must be zero. However, to calculate the mass flux, velocities at cell faces are needed which are obtained by interpolation on collocated grids. The interpolated velocities at cell faces are further modified, to yield a compact pressure-correction equation and avoid oscillatory solutions on non-orthogonal grids, by adding the difference between the interpolated and actual pressure gradients calculated at the cell face (Rhie and Chow, 1983).

$$u_{i,e}^{m*} = \overline{(u_i^{m*})_e} - \Delta\Omega_e \overline{\left(\frac{1}{A_P^{u_i}} \right)_e} \left[\left(\frac{\delta p}{\delta x_i} \right)_e - \overline{\left(\frac{\delta p}{\delta x_i} \right)_e} \right]^{m-1} \quad (3.42)$$

where the overbar denotes interpolated values. The cell face velocity-correction is expressed in terms of the interpolated values of the coefficients $\frac{1}{A_P^{u_i}}$ instead of equation 3.41.

$$u'_{i,e} = -\overline{\left(\frac{1}{A_P^{u_i}} \right)_e} \left(\frac{\delta p'}{\delta x_i} \right)_e. \quad (3.43)$$

The mass fluxes calculated using the interpolated velocity do not satisfy the continuity equation and their sum gives a mass source. In order to satisfy the continuity constraint for each CV the mass fluxes are corrected by using the velocity-correction expressed in terms of the gradient of the pressure-correction (equation 3.43):

$$\sum_c (\rho u_n^{m*} S)_c - (\rho \Delta\Omega S)_c \overline{\left(\frac{1}{A_P^{u_i}} \right)_c} \left(\frac{\delta p'}{\delta n} \right)_c = 0 \quad (3.44)$$

where c stands for a CV face in the east, west, north, south, top and bottom directions and the summation is implied over all these faces. Equation 3.44 when written for all the faces of all the CVs gives an equation for pressure-correction, p' .

3.4 Implementation of Boundary Conditions

Usually, the boundaries are not aligned with the coordinate directions $(\mathbf{i}, \mathbf{j}, \mathbf{k})$ on non-orthogonal grids and care must be taken while implementing the boundary conditions. For implementing boundary conditions a local Cartesian coordinate system $(\mathbf{n}, \mathbf{t}_g, \mathbf{s})$ is used, which is rotated with respect to the coordinate directions $(\mathbf{i}, \mathbf{j}, \mathbf{k})$ such that \mathbf{n} is the outward unit normal vector and \mathbf{t}_g and \mathbf{s} are unit vectors tangential to the boundary. Implementation details of inlet and outlet boundary conditions can be found in Ferziger and Perić (1996), for the symmetry boundary condition in Perić (1985) and are briefly summarized here. These boundary conditions correspond to the following two cases:

- known boundary values (Dirichlet condition)
- known boundary fluxes (Neumann condition).

The first type applies to inlet boundaries where the values of all variables are known. This condition is incorporated in the solution procedure by assigning the known values to the boundary nodes. The second type applies to the symmetry and outlet boundaries where the boundary flux is known. If the boundary flux is known then the boundary values are evaluated from the discretized flux expressions.

3.4.1 Evaluation of Tangential Gradients

At the interface, implementation of the continuity of stress boundary condition equation 2.8 presents an additional difficulty because gradients in the direction of tangential velocity are needed at the interface as described below. If the tangential direction \mathbf{t}_g is chosen to lie in the direction of the resultant shear-force at the interface then equation 2.8 can be written in terms of the local coordinate system $(\mathbf{n}, \mathbf{t}_g, \mathbf{s})$ as follows

$$\mu \left(\frac{\partial u_t}{\partial n} + \frac{\partial u_n}{\partial t_g} \right)_{g,int} = \mu \left(\frac{\partial u_t}{\partial n} + \frac{\partial u_n}{\partial t_g} \right)_{l,int} . \quad (3.45)$$

Implementation of equation 3.45 requires the evaluation of the gradients in the normal and tangential directions. The evaluation of the normal gradient is described in Ferziger and Perić (1996) and Perić (1985). The gradient in the tangential direction can be evaluated in terms of the gradients along the grid-lines lying on the interface. An obvious choice would be to use linear interpolation to evaluate this derivative in terms of the derivatives along the grid-lines

$$\frac{\partial\phi}{\partial t_g} = (\mathbf{t}_g \cdot \mathbf{t}_{g_1}) \frac{\partial\phi}{\partial t_1} + (\mathbf{t}_g \cdot \mathbf{t}_{g_2}) \frac{\partial\phi}{\partial t_2} \quad (3.46)$$

where \mathbf{t}_{g_1} and \mathbf{t}_{g_2} are unit vectors along the non-orthogonal grid-lines lying on the interface and \mathbf{t}_g is the unit vector in the direction of resultant shear-force at the interface. Equation 3.46 is exact on orthogonal grids but introduces an error on non-orthogonal grids. For non-orthogonal grids the derivative is evaluated as follows

$$\frac{\partial\phi}{\partial t_g} = \frac{(\mathbf{t}_g \cdot \mathbf{t}_{g_1}) - (\mathbf{t}_{g_1} \cdot \mathbf{t}_{g_2})(\mathbf{t}_g \cdot \mathbf{t}_{g_2})}{1 - (\mathbf{t}_{g_1} \cdot \mathbf{t}_{g_2})^2} \frac{\partial\phi}{\partial t_{g_1}} + \frac{(\mathbf{t}_g \cdot \mathbf{t}_{g_2}) - (\mathbf{t}_{g_1} \cdot \mathbf{t}_{g_2})(\mathbf{t}_g \cdot \mathbf{t}_{g_1})}{1 - (\mathbf{t}_{g_1} \cdot \mathbf{t}_{g_2})^2} \frac{\partial\phi}{\partial t_{g_2}}. \quad (3.47)$$

Equation 3.47 reduces to equation 3.46 for orthogonal grids ($\mathbf{t}_{g_1} \cdot \mathbf{t}_{g_2} = 0$).

3.4.2 Evaluation of Grid Distortion and Interface Motion

In the present study droplets are assumed to remain spherical in shape throughout their life-times. This assumption means that the kinematic condition (used for interface tracking) is identical at all points on the interface and the problem of determining interface motion reduces to finding out the droplet diameter after grid movement. The droplet diameter after distortion, d^{new} , is calculated by requiring that the change in droplet mass, due to a change in its volume, is equal to the amount of mass vaporized from its surface.

$$\frac{d}{dt} \int_{\Omega} \rho d\Omega = \int_S \dot{m} dS \quad (3.48)$$

Failure to satisfy equation 3.48 will lead to artificial mass sources or sinks for droplets. Since the numerical grid merely provides an approximation of the droplet volume or surface area (which becomes better as the grid is refined but is never exact), equation 3.48 cannot be solved directly (for example by using the formula for the volume and surface area of a sphere). Instead one has to find out the volume of the droplet, as approximated by the numerical grid for a given diameter, by adding up the volumes of all its individual constituent CVs. This lack of an explicit functional relationship between volume/surface area and droplet diameter prevents the calculation of droplet diameter directly from equation 3.48. An iterative solution procedure based on bisection method (see for example Press *et al.* 1992) is used to solve equation 3.48 for the droplet diameter. Once the new droplet diameter is known the grid inside the droplet is moved linearly such that for each grid-point the change in radial distance from droplet center is given by

$$\frac{r}{d^{old}}(d^{new} - d^{old}) \quad (3.49)$$

where d^{new} is the droplet diameter after distortion, d^{old} is the droplet diameter before distortion and r is the radial distance of a grid-point from the droplet center. The grid in the gas phase follows the interface motion.

3.5 Solution Algorithm

The overall solution algorithm is same for both the gas and liquid phase and can be summarized as follows (a flowchart of the outer iteration procedure is shown in Figure 3.3):

- All the variables are initialized at $t = t_0$ by assigning them initial values (equations 2.23 and 2.24) and the time is advanced $t_1 = t_0 + \Delta t$.
- The grid is distorted (as outlined in section 3.4.2) for the current time-level using the previous iteration value as an initial guess and the coupled non-linear equations are

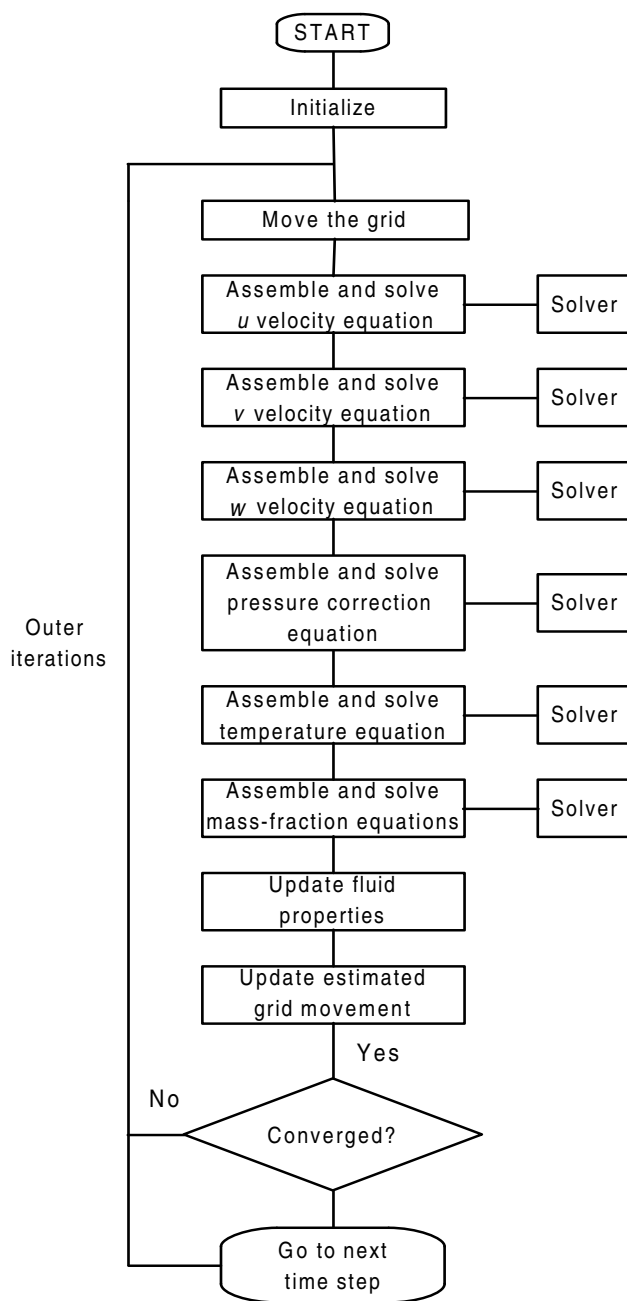


Figure 3.3: Solution algorithm

iteratively solved for the current time-level by repeatedly carrying out the following steps:

1. An algebraic equation system (section 3.1.3) for each velocity component is obtained by assembling the momentum equations as outlined in section 3.1. In each such algebraic equation system values of pressure, fluid properties and velocity components other than the one being solved for, are taken from the previous iteration and treated as known. An improved estimate of the velocity at the current time-level is obtained by iteratively solving these linear equation systems using the Strongly Implicit Procedure of Stone (1968).
 2. Mass fluxes through CV faces are calculated using the improved estimate of the velocity field and the pressure-correction equation is derived by requiring that mass-conservation is satisfied (section 3.3).
 3. Pressure-corrections, p' , are obtained by solving the pressure-correction equation, which are then used to correct the mass fluxes, velocities and pressures as outlined in section 3.3.
 4. Energy and species conservation equations are discretized, in a manner similar to step 1, and solved to obtain improved estimates of temperature and mass fractions at the current time-level.
 5. The fluid properties are updated.
 6. An improved estimate of the grid movement is calculated using equation 3.48 and the grid is moved to fit the new boundaries (as outlined in section 3.4.2).
- Steps 1 to 6 are repeated until the residual in each equation becomes sufficiently small. When all the equations are satisfied to a specified tolerance ($\leq 10^{-6}$) the solution at the current time-level is complete and time is advanced by another Δt ($\Delta t = 10^{-5}$ s). The solution of the current time-level serves as an initial guess for the solution at the new time-level and the above procedure is repeated by returning to step 1.

Chapter 4

Results and Discussion

The results of numerical calculations are discussed in this chapter. It is divided into four major parts:

- Study of the effect of introducing additional conservation laws on moving grids
- Study of convergence acceleration, on moving grids, by application of the multigrid technique to a problem involving phase change
- Study of three-dimensional interaction effects between two solid spheres as a first approximation to droplets vaporization and ignition
- Study of three-dimensional interaction effects between two vaporizing and igniting droplets.

4.1 Generalization of Space Conservation Law

The effects of introducing additional conservation laws (see section 3.2.2.2), on moving grids, was studied in a three-dimensional lid driven cavity flow. A schematic of the flow configuration, along with the boundary conditions, is shown in Figure 4.1. Four different test cases $C1$, $C2$, $C3$, and $C4$ were chosen as described in Table 4.1.

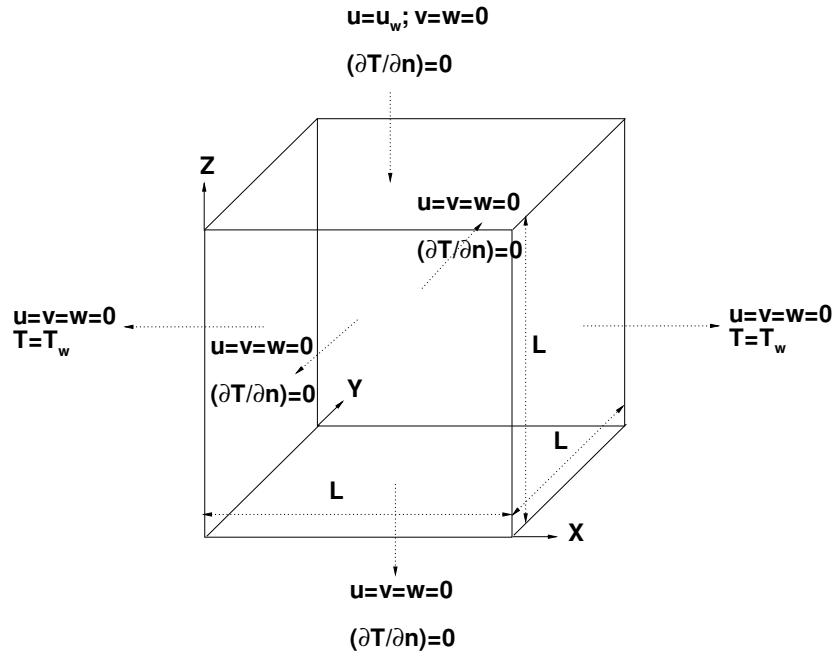


Figure 4.1: Schematic of flow configuration

Test Case	Description
$C1$	Stationary grid calculation on Grid1
$C2$	Moving grid calculation in which only the SCL (equation 3.27) is satisfied
$C3$	Moving grid calculation satisfying the entire set of conservation equations 3.29
$C4$	Stationary grid calculation on Grid2

Table 4.1: Description of test cases

For all calculations, lid dimension $L = 1$, lid velocity $u_w = 1$, gas density $\rho = 1$, gas viscosity $\mu = 0.01$, thermal conductivity of gas $k = 0.01$, specific heat of gas $c_p = 1$, wall temperature, T_w , was varied linearly from $T_w = 1$ at $t = 1$ to $T_w = 0.5$ at $t = 7$ after which T_w was held constant at 0.5 (by prescribing these values the governing equations are solved in dimensionless form with the code which discretizes the equations expressed in terms of physical variables). This gives a Reynolds number, based on u_w and L , of 100 while the Prandtl number varies from 1 to 2. Initial values of $u_o = v_o = w_o = 0$ and $T_o = 1$ were prescribed in the computational domain. The time step, $\Delta t = 1$ was used for all calculations and the calculations were performed until $t = 14$. An O -grid was generated inside the 3D cavity using the commercial grid-generator *ANSYS ICEMCFD-HEXA*. The calculations on the stationary grid (test case *C1*) were carried out on Grid1, a cross-section of which is shown in Figure 4.2. Since an O -grid is used owing to symmetry of the computational domain the other two cross-sections are identical to the one shown in Figure 4.2. For the calculations on moving grids (test cases *C2* and *C3*), grid movement was prescribed such that the grid changed from its initial configuration, Grid1, to its final configuration, Grid2, with the rate of change of CV volumes (or grid movement) decaying exponentially with time. Initially, the maximum rate of change of CV volume was approximately 50% ($0.5 \leq \left| \frac{\Omega^{t_o+1} - \Omega^{t_o}}{\Omega^{t_o}} \right| \leq 1.5$). A comparison of the cross-sectional view of Grid2 (obtained at $t = 14$) with Grid1 (at $t = 0$) is shown in Figure 4.2(b).

Variable values, at a monitoring point located at the center of the computational domain, are compared from the three test cases. Figure 4.3 shows the evolution of the maximum temperature and the temperature at the reference point. It is seen from Figure 4.3 that test case *C2*, which satisfies the entire set of conservation equations (equations 3.29), reproduces the solution on the stationary grid (test case *C1*) exactly, while test case *C3*, which satisfies the SCL only, deviates from the stationary grid solution.

Similar observation can be made for the X - velocity components shown in Figure 4.4. The Y - and Z -components of velocity are compared in Figure 4.5. Test case *C2* reproduces the stationary grid (*C1*) results exactly until $t = 6$ while test case *C3* again deviates from the

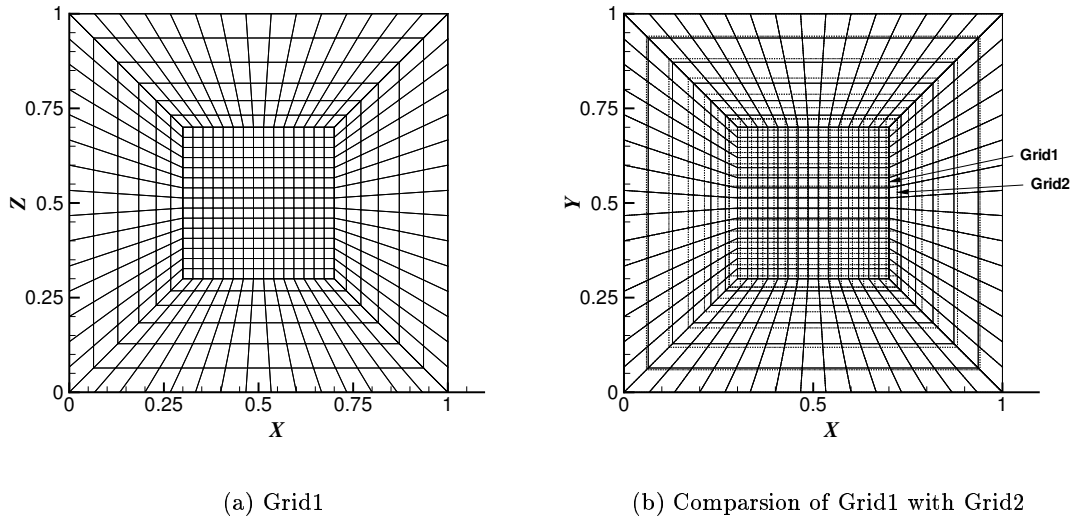


Figure 4.2: Cross-section of numerical grids

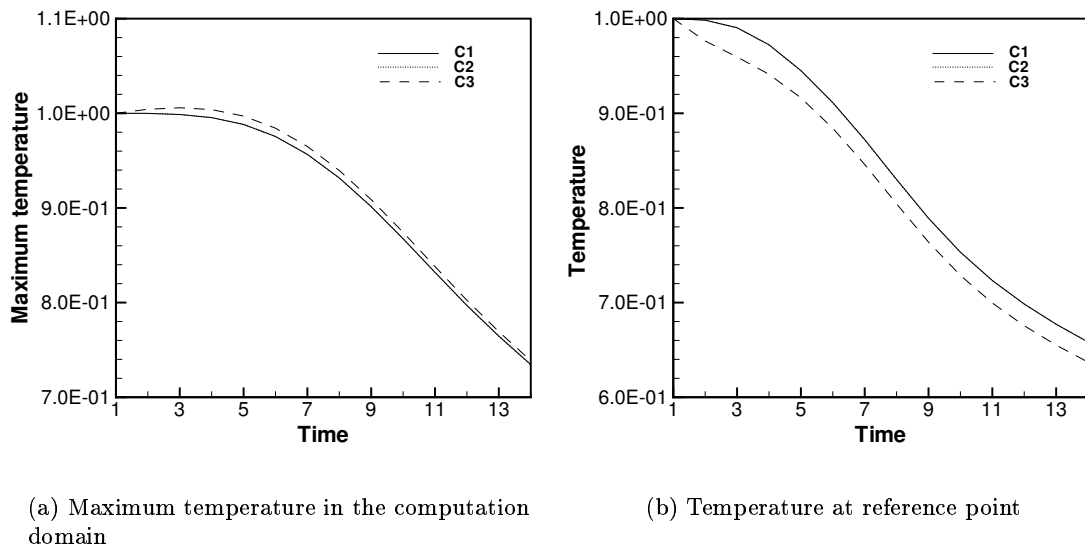


Figure 4.3: Comparison of temperatures

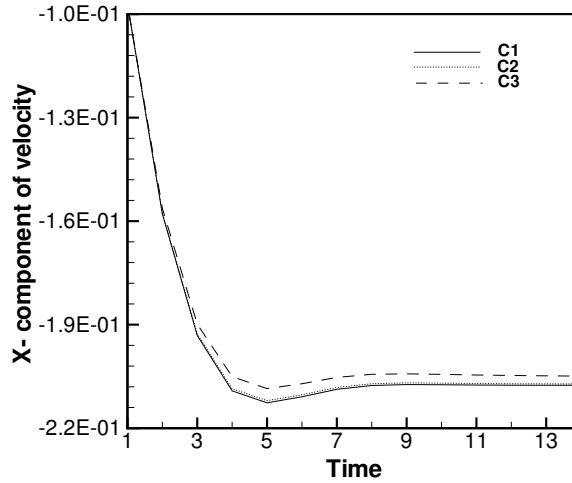
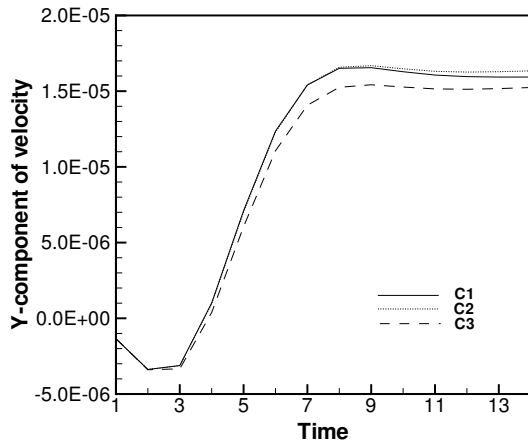


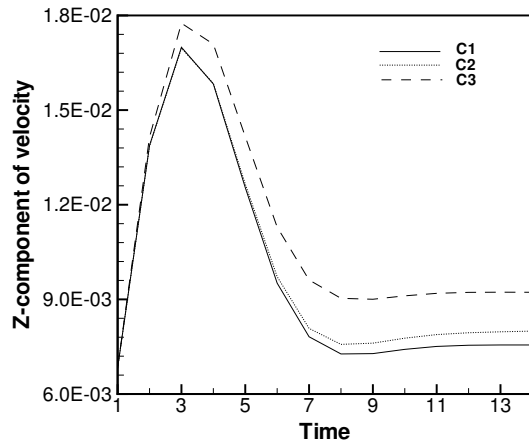
Figure 4.4: X -component of velocity at reference point

stationary grid solution. There is a discrepancy, between test case $C1$ and $C2$, during the later parts ($t \geq 7$) of the computations in Figure 4.5 which is explained below. Since the grid movement decays exponentially with time and is almost negligible when $t \geq 11$, one can conclude that the deviation from the stationary grid values, during the later parts ($7 \geq t \leq 11$) of the computation, are not due to grid movement. Instead, unlike the temperatures or X -component of velocity, the Y - and Z - components of velocity are quite sensitive to the grid used for computation and the deviation occurs because of changes in the underlying geometrical features of the grid. This is readily confirmed by carrying out computations (test case $C4$) on a stationary grid, Grid2, and comparing it with test cases $C1$ and $C2$ (shown in Figure 4.6). It is evident from Figure 4.6 that the Y - and Z - components of velocity are indeed sensitive to the grid used. The moving grid calculation, test case $C2$, lies intermediate of $C1$ and $C4$, and, shifts in proximity from $C1$ to $C4$ as time progresses, as expected.

To further emphasize the importance of satisfying the entire set of conservation equations (equations 3.29) another series of computations was performed on very rapidly moving grids. Except for the rate of grid movement the computations (i.e. the flow geometry, initial and boundary conditions etc.) are identical to the one described above (section 4.1). The grid

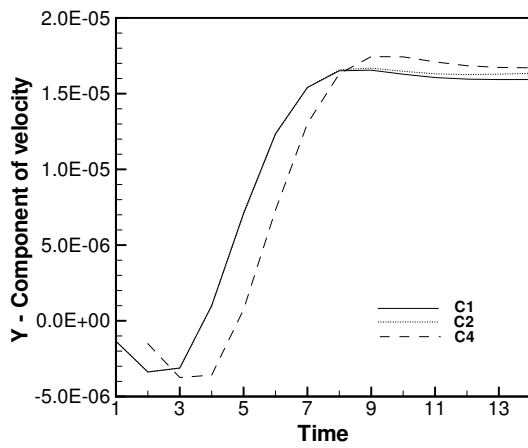


(a) Y - component of velocity at reference point

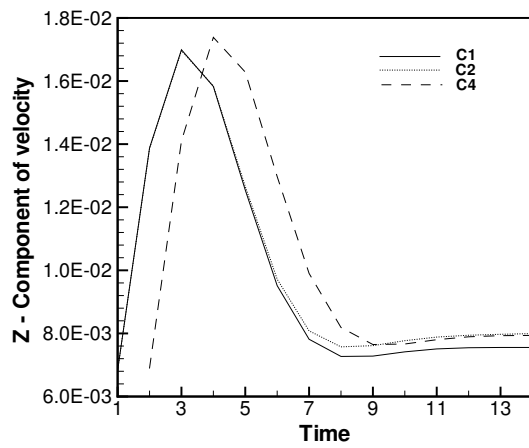


(b) Z - component of velocity at reference point

Figure 4.5: Comparison of velocity components



(a) Y - component of velocity at reference point



(b) Z - component of velocity at reference point

Figure 4.6: Comparison of velocity components

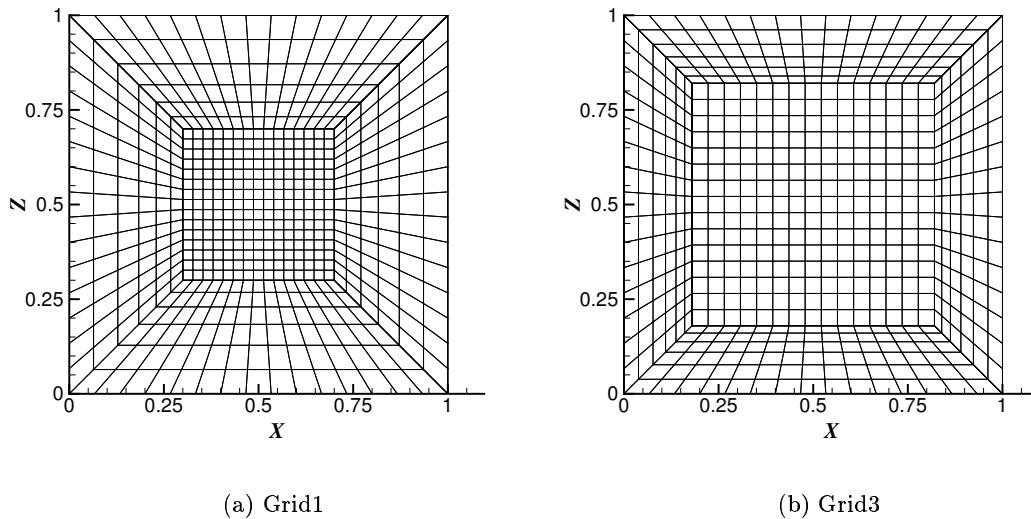
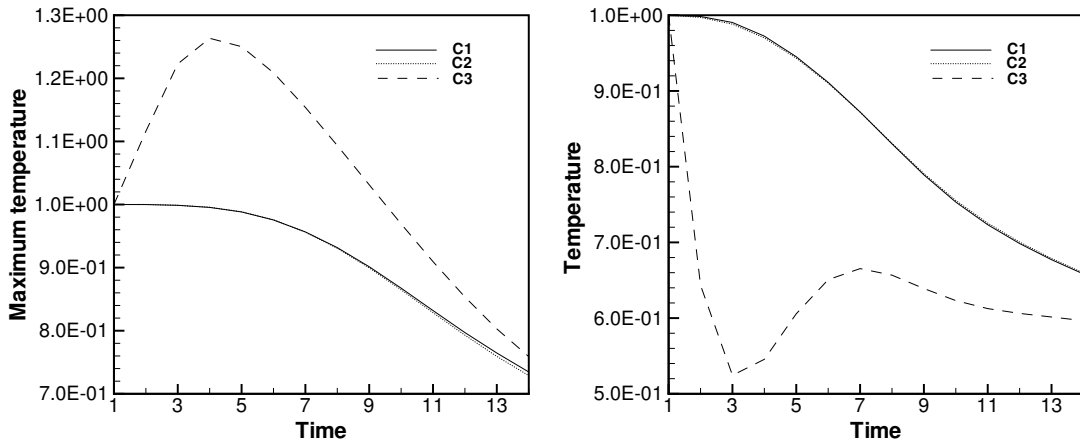


Figure 4.7: Cross-sections of numerical grids

is moved from its initial configuration, Grid1, at $t = 0$, to its final configuration, Grid3, at $t = 14$. The rate of change of CV volumes again decayed exponentially with time as above and the initial maximum rate of change of CV volume was such that $0.1 \leq \left| \frac{\Omega^{t_o+1} - \Omega^{t_o}}{\Omega^{t_o}} \right| \leq 10$. The cross-sectional views of the two grids are shown in Figure 4.7 for comparison. It can be seen from Figure 4.7 that the configuration of the grid changes considerably. Since most of the grid movement happens during the first few time-steps the rate of grid movement is very rapid. Figure 4.8 shows the evolution of the maximum temperature in the computational domain and the temperature at the monitoring point with time.

Since the wall temperature is never greater than unity, $T_w \leq 1$, and the initial temperature, $T_o = 1$, the maximum temperature in the computational domain should never exceed unity. An inspection of the maximum temperatures in Figure 4.8(a) shows that failure to satisfy the additional conservation law for temperature gives the unphysical result of temperatures in excess of unity in the computational domain. The temperature at the monitoring point is in bad agreement too when the additional conservation law for temperature is not satisfied (test case C3). Test case C2, which satisfies the additional conservation law for temperature, produces results in good agreement with those on stationary grid (test case C1). The remark-



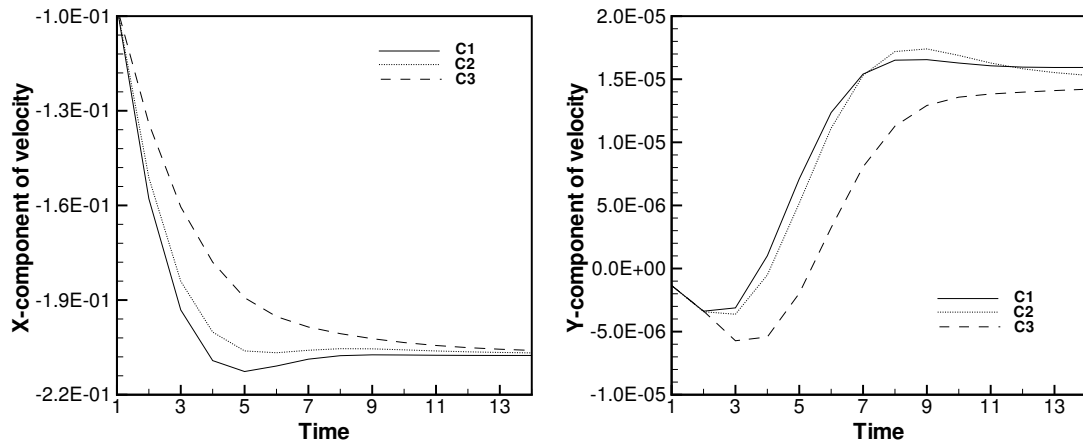
(a) Maximum temperature in the computational domain

(b) Temperature at monitoring point

Figure 4.8: Comparison of temperatures

ably good agreement between predicted temperatures for test cases $C1$ and $C2$ is expected since temperature is the only unsteady variable.

Figures 4.9 and 4.10 show the evolution of velocity components, at the monitoring point, with time, for the three test cases ($C1$, $C2$ and $C3$). Test case $C2$ does not reproduce the stationary grid computation, test case $C1$, results exactly since the grid movement is very rapid. However, the results for test case $C2$, which satisfies additional conservation law for velocity, are much closer to the stationary grid computations, test case $C1$, while those of test case $C3$, which does not satisfy the additional conservation law for velocity, are further away. Particularly, it can be seen that for test case $C3$ the difference in the Z -component of velocity at $t = 4$ is approximately about 45 percent while test case $C2$ produces reasonable results. The large discrepancy in the Z -component of velocity near the end of the computation is due to its sensitivity on the grid as shown above.



(a) X - component of velocity

(b) Y - component of velocity

Figure 4.9: Comparison of velocity components

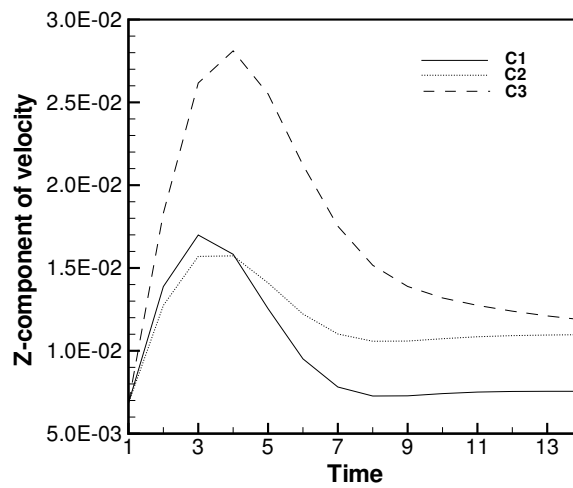


Figure 4.10: Z -component of velocity

Parameter	Value	Parameter	Value
Free-stream Temperature	1250 K	Initial Drop Temperature	300 K
Molecular Weight of Oxidizer	20.0 kg/mol	Free-stream Pressure	10^5 Pa
Initial Relative Velocity of Drop	25.0 m/s	Liquid-phase Prandtl Number	8.59
Initial Gas-phase Reynolds Number	100	Gas-phase Prandtl number	0.74
Molecular Weight of Fuel	114.2 kg/mol	Liquid/Gas phase Viscosity	10.49
Liquid/Gas phase Specific Heat	1.87	Liquid/Gas phase Density	251.93
Latent Heat/Specific Heat of Liquid	135.95 K	Gas-phase Schmidt Number	2.36

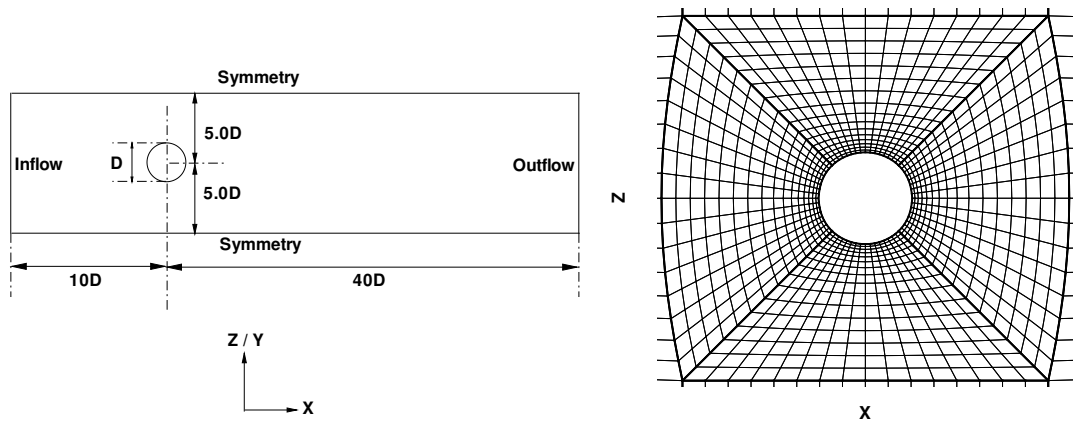
Table 4.2: Initial parameters used in the study

4.2 Convergence Acceleration by Multigrid

The convergence acceleration obtained by applying the multigrid technique on moving grids is studied for an example problem of a liquid drop vaporizing in a convective gas flow. The vaporization of a cold n-octane drop suddenly injected into a hot air stream was simulated. Since the variation of liquid properties with temperature is not large constant physical properties are used for the liquid phase. The physical parameters used in the study are listed in Table 4.2.

A schematic of the flow configuration, along with the boundary conditions, is shown in Figure 4.11(a). Two O -grids were generated, the first one inside the drop and the second one around the drop. A cross-sectional view of the block structure and the grid around the drop is also shown in Figure 4.11(b). As the droplet decreases in size due to vaporization the grid inside and around the drop moves to account for the change in droplet size. It can be seen that the quality of the grid (in terms of angles between grid lines) does not deteriorate much as the drop size decreases.

The finest grid for all computations is kept same and has about 3.5×10^5 CVs. Computations have been carried out on a single grid (hereafter designated SG), multigrid with two grid-levels ($MG2$) and multigrid with three grid-levels ($MG3$). The corresponding cycle definitions are shown in Figure 4.12. For all computations the solution for a given time step were taken to



(a) Schematic of flow configuration

(b) Partial view of grid around the drop

Figure 4.11: Schematic of flow configuration and the grid around the drop

be converged when the maximal relative residual of all equations fell below 5×10^{-6} . The computations were stopped when the mass of the drop fell below 12 % of its initial value at which point the size of the droplet becomes extremely small to allow further grid movement.

The number of outer iterations on the finest grid, required for convergence, for the single grid (*SG*) and multigrid (*MG2* and *MG3*), computations are shown in Figure 4.13 for different time steps.

The oscillations in the number of outer iterations for time steps between 250 and 450 observed in all the three calculations are believed to be due to the iterative nature of the solution procedure as the droplet surface reaches its wet bulb temperature. The wet bulb temperature is reached after about 450 time steps. Figure 4.13(a) clearly shows the reduction in the number of outer iterations, required on the finest grid, when multigrid technique is used. The difference becomes more pronounced as the number of multigrid levels increases from 2 to 3. The multigrid convergence acceleration, defined as the ratio of the number of fine grid iterations on single grid to the number of fine grid iterations on multigrid, is also shown in Figure 4.13(b). On an average the overall calculation speeds up approximately by a factor of 4 for multigrid with 2 grid-levels while multigrid with 3 grid-levels speeds it up approximately

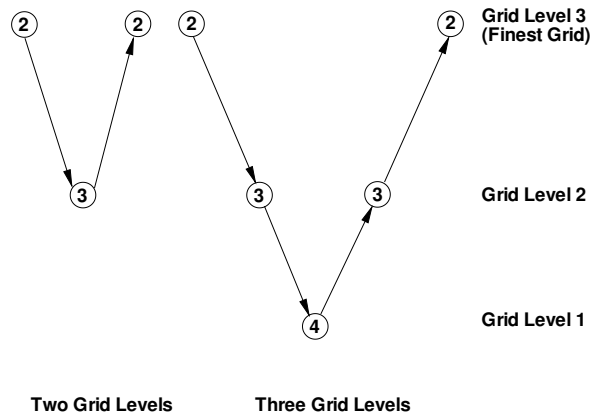
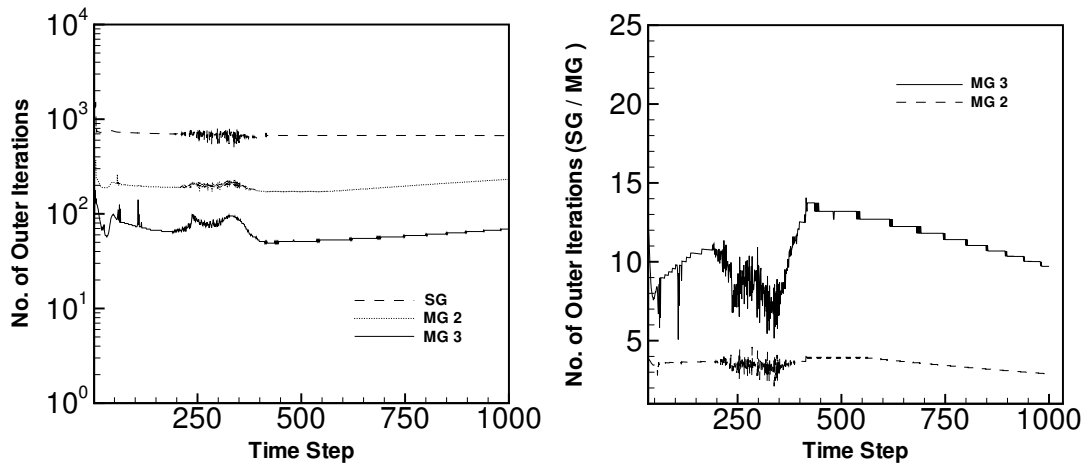


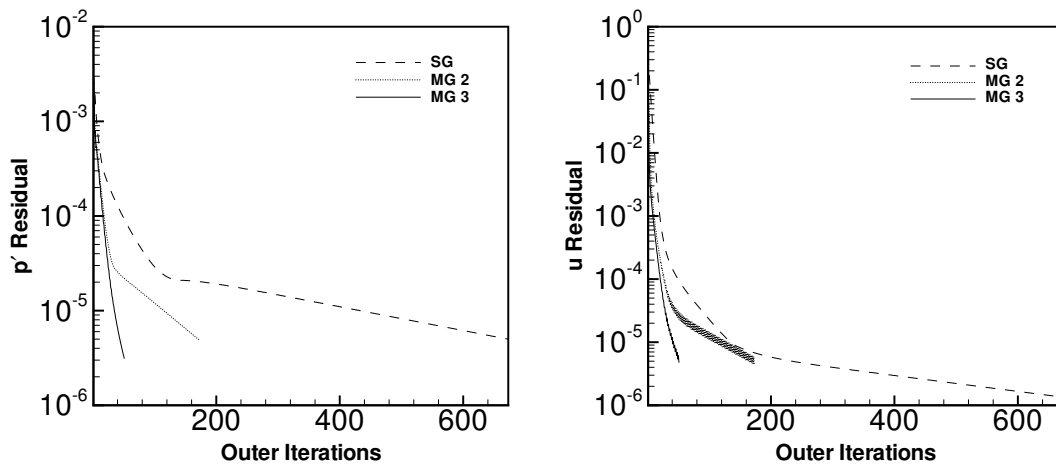
Figure 4.12: Multigrid cycle definition



(a) Number of outer iterations on finest grid for different time steps

(b) Number of SG / MG outer iterations on the finest grid for different time steps

Figure 4.13: Convergence history



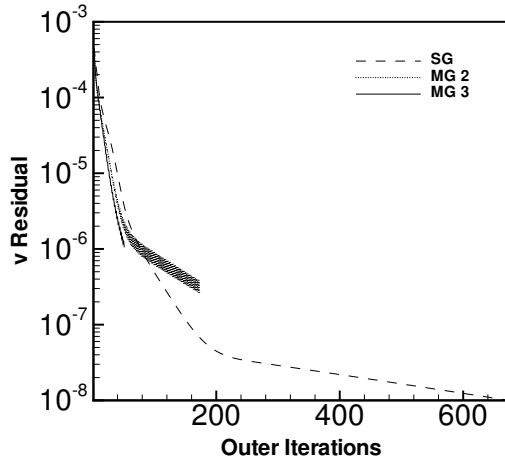
(a) Residuals of pressure-correction equation as a function of the number of fine grid iterations

(b) Residuals of X -component of momentum equation as a function of the number of fine grid iterations

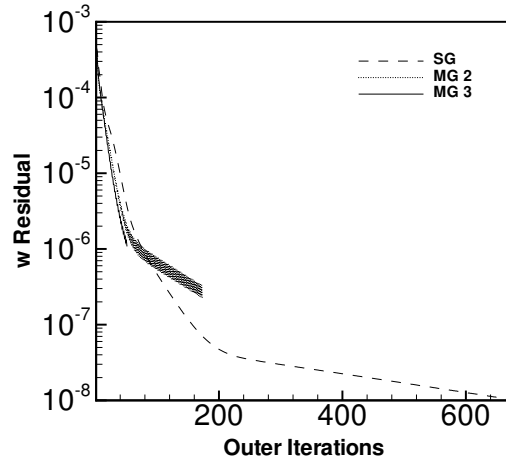
Figure 4.14: Residual history

by a factor of 10. The total computational time required by multigrid with 2 grid-levels was about half of that required by single grid and that of multigrid with 3 grid-levels was about one-fourth of that required by single grid.

Figure 4.14 shows the residuals, of the pressure-correction equation and X -component of momentum equation, as a function of outer iterations at time step 500 for single grid and multigrid computations. For multigrid computations with 2 grid-levels ($MG2$) the residuals fall linearly in the beginning but after the residuals fall below a certain value they decrease more slowly. For the multigrid computations with 3 grid-levels the residuals fall almost linearly at a constant rate. However, for the single grid computations, the residuals fall in a somewhat exponential fashion whereby the residuals decrease more slowly as they get smaller. It can be seen that if the convergence criterion is made smaller the difference between the number of iterations required for multigrid with 3 grid-levels ($MG3$) and single grid (SG) computations will increase and very high multigrid convergence acceleration rates can be obtained.

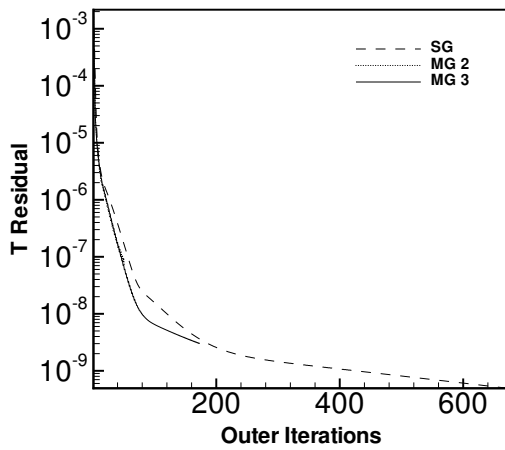


(a) Residuals of Y -component of momentum equation as a function of the number of fine grid iterations

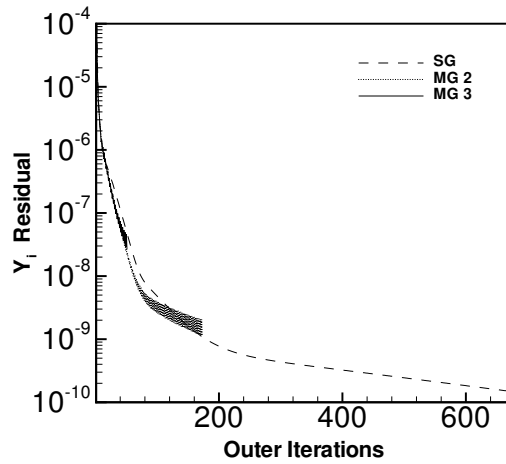


(b) Residuals of Z -component of momentum equation as a function of the number of fine grid iterations

Figure 4.15: Residual history



(a) Residuals of energy equation as a function of number of fine grid iterations



(b) Residuals of mass-fraction equation as a function of number of fine grid iterations

Figure 4.16: Residual history

For the sake of completeness the residual histories of other equations are shown in Figures 4.15 and 4.16 and they show similar behaviour as discussed for residuals in Figure 4.14. The rate of decrease of residuals in Figures 4.15 and 4.16 is much faster than that in Figure 4.14 for all computations. The residuals in Figures 4.15 and 4.16 quickly fall below the convergence criteria, for all computations, and thus are not the convergence rate determining factors for this particular problem. The residuals of the pressure-correction equation fall more slowly than those of other equations and the convergence acceleration effect is best seen in the residual histories of the pressure-correction equation. The multigrid convergence acceleration factors obtained in this study can be improved further by either using more than 3 grid-levels or using more refined grids or by making the convergence criterion smaller (more restrictive). The computations presented in this study show that on moving grids, when the grid movement is not known *a priori* and is implicitly calculated, the multigrid technique can be implemented with minor modifications to obtain convergence acceleration.

4.3 Interaction between two Solid Spheres in a Convective Flow

A detailed study is performed to assess the ability of the code to accurately simulate the interaction between droplets. The major concern here was to see whether the interaction effects between multiple bluff bodies is accurately reproduced by the code and whether the introduction of more than one bluff body caused any additional computational difficulties. For this purpose the interaction between two fixed identical solid spheres is chosen which has been studied by Kim *et al.* (1993).

The schematic of the flow configuration is shown in Figure 4.17 in which the physical length scales are non-dimensionalized using the sphere diameter D . Different conditions were studied by varying the distance between the centers of the two spheres. Figure 4.17 shows the case for a separation distance, $S = 4.5$, defined as the distance between the centers of the two spheres normalized by the sphere diameter. Symmetry boundary condition was implemented at the walls by prescribing zero convective fluxes of all quantities and zero normal gradients

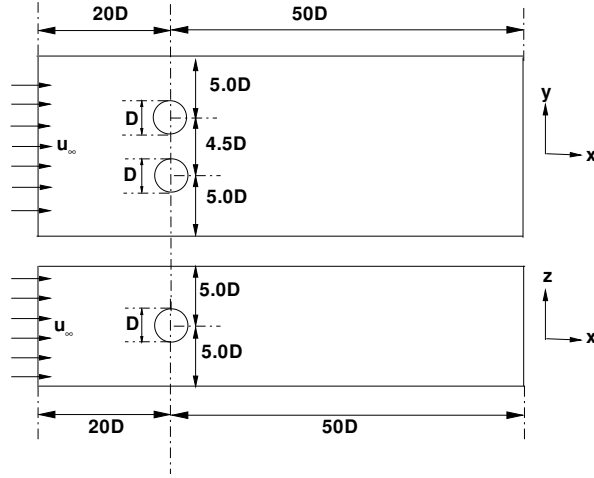


Figure 4.17: Schematic of the flow configuration for $S = 4.5$ for two cross-sectional views of velocity components parallel to the symmetry plane ($\frac{\partial u_p}{\partial n} = 0$). On the spheres, the velocities were set equal to zero. Zero-gradient boundary condition was prescribed at the outlet boundary. At inlet a constant free-stream velocity, u_∞ , parallel to X -axis is prescribed and all variables are given initial values of zero except at the inlet where $u = 1$, $v = w = p = 0$. For all calculations the sphere diameter $D = 1$ m, free-stream velocity $u_\infty = 1$ m/s, density $\rho = 1$ kg/m³ and viscosity $\mu = 0.01$ Ns/m² giving a Reynolds number of 100.

The length of the first row of cells in the immediate vicinity of the sphere surface was about $0.005D$. The solution was tested by varying the location of the outflow boundary. When the outflow boundary was moved from $50D$ to $100D$ the drag coefficient changed by 0.92 percent for a Reynolds number, based on sphere diameter of 100.

4.3.1 Wake Structure

The minimum distance between the two spheres occurs in the $X - Y$ symmetry plane and hence the interaction between them will be strongest in this plane. The characteristics of the wake in this plane are presented. Figure 4.18 shows the streamline pattern around a single sphere in the $X - Y$ plane at a Reynolds number of 100 (see Johnson and Patel, 1999).

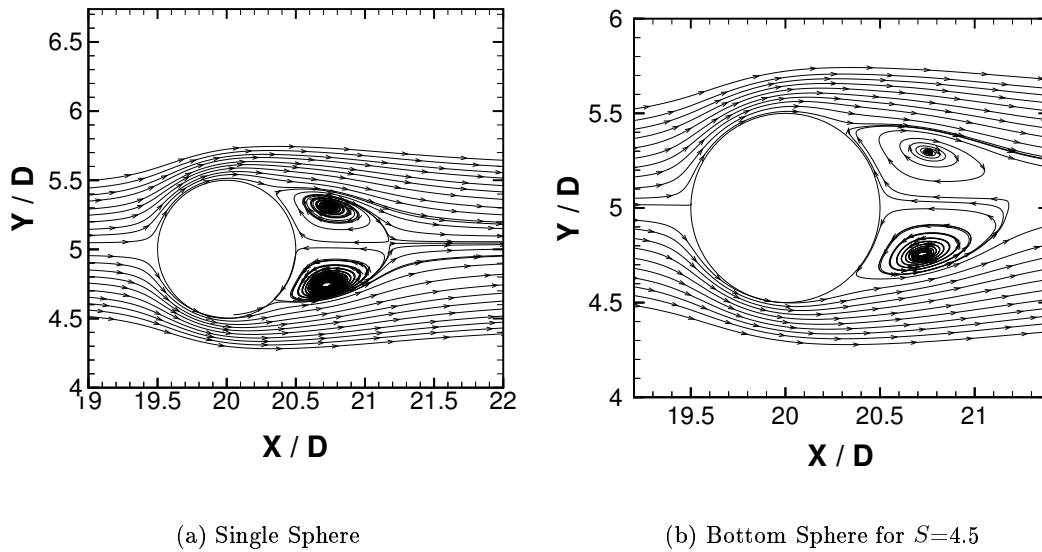


Figure 4.18: Streamline patterns in the $X - Y$ plane at a Reynolds number of 100.

It is well known that the flow past a single sphere at this Reynolds number is steady and axi-symmetric, the stagnation point is located on the axis of symmetry and two identical counter-rotating vortices are seen in the wake.

Figure 4.18 also shows the streamlines around the bottom sphere in the $X - Y$ plane at a Reynolds number of 100. The pattern is similar for the top sphere too. The separation distance between the two spheres is $S = 4.5$. A streamline pattern quite different from that of the single sphere axi-symmetric case is obtained. Although two counter rotating eddies can still be seen but both eddies are now smaller than those of axi-symmetric flow. The bottom eddy is attached to the sphere while the top eddy is detached from the sphere. Also, the bottom eddy is larger than the top eddy and thus both the eddies are not even of the same strength. The bottom eddy is formed by fluid separating from the bottom of the sphere and in this sense is similar to the axi-symmetric case. The top eddy on the other hand is formed not by the separation of fluid from the sphere but rather by the entrainment of the fluid from the lower eddy. One can also see flow across the axis of geometrical symmetry as some fluid from the bottom passes between the detached top eddy and the sphere. Thus, the axi-symmetry is clearly lost due to hydrodynamic interaction between the spheres. These

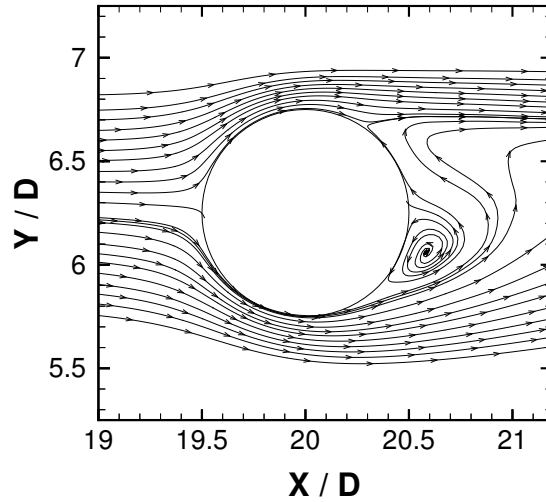


Figure 4.19: Streamline patterns in the $X - Y$ plane for bottom sphere at $S = 1.5$ and $Re = 100$.

differences from the axi-symmetric case are because the flow region between the two spheres is confined and becomes narrower. Thus, the fluid in this narrow region is accelerated and consequently the pressure decreases due to acceleration. The pressure above the sphere is lower than the pressure below the sphere and the fluid from the bottom eddy is pushed upwards. The fluid approaching the sphere from the top left is decelerated, consequently increasing its pressure. Thus, the pressure in the top left is more than in the bottom left, as the fluid is not confined at the bottom of the sphere. There is a difference in pressures between the top and bottom portions of the sphere on left side and at the center with the pressures on the top being less. The situation will be opposite for the right side of the sphere where the pressure on the top will be less than on the bottom side. However, due to viscous effects the pressure does not recover fully and the pressure difference is greater on the left side and is not quite compensated for by the pressure difference at the right, giving rise to a repulsive force between the spheres. This is shown later in the pressure plot.

Figure 4.19 shows the streamline pattern around the bottom sphere in the $X - Y$ plane at a Reynolds number of 100 at a separation distance between the two spheres of $S = 1.5$. The streamline pattern in this case is completely different from the axi-symmetric case and

from that for $S = 4.5$. The most striking difference is that the upper eddy is absent. Fluid separating from the top part of the sphere does not undergo recirculation whereas the portions of fluid separating from the bottom eddy and moving upwards almost reach the top separation point without recirculation before moving downstream. The size of the bottom eddy is also smaller, and about half the size, compared to the $S = 4.5$ case.

4.3.2 Pressure and Shear Stress Distribution

Figure 4.20 shows the non-dimensional pressure coefficient, $2(p - p_\infty)/\rho u_\infty^2$, around the bottom sphere in the $X - Y$ plane at a Reynolds number of 100 for $S = 4.5$ and for $S = 1.5$. The change in the relative magnitudes of the pressure between the top and the bottom of the spheres for the two different separation distances can be clearly seen. While for $S = 4.5$ the top part has higher pressure, for $S = 1.5$ the top part has lower pressure as compared to the bottom part. For $S = 4.5$ the pressure on the top of the sphere, between $\theta = -\pi$ and $\theta = -2.2$ radians, is seen to be less than the pressure on the bottom and almost of equal magnitude elsewhere. It thus contributes to a positive lift force, which tends to attract the spheres. We focus on $S = 1.5$ in the following discussion. On an average the pressure is higher on the top, contributing to a negative lift force and thus to a repulsion between the spheres. The pressure on the bottom of the sphere is lower than that on the top between $\theta = -3.14$ and $\theta = -2.5$ radians where the angle at the front stagnation point, of the axi-symmetric flow case, is $\theta = -3.141$ and at the rear stagnation point is $\theta = 0$. On the bottom of the sphere the minimum pressure occurs at an angle less than $\theta = -2.4$ radians while on the top it occurs at an angle greater than this value and is lower than the minimum pressure on the bottom of the sphere. The maximum pressure is shifted a few degrees towards the symmetry plane measured from $\theta = -\pi$. These observations suggest that the front and rear stagnation points are shifted a few degrees towards the $X - Z$ symmetry plane.

Figure 4.21 shows the shear-stress coefficient, $\frac{2\tau}{\rho u_\infty^2}$, in the same plane as that used for the pressure coefficient in Figure 4.20, at a Reynolds number of 100 for $S = 4.5$ and for $S = 1.5$, respectively. As in the case for Figure 4.20 the same qualitative trend is observed for both

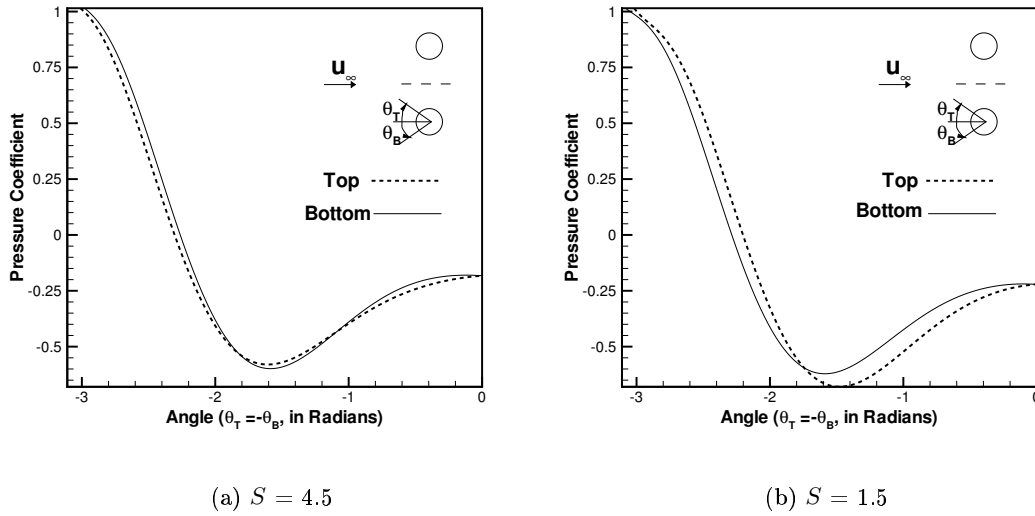


Figure 4.20: Distribution of pressure coefficient

$S = 4.5$ and $S = 1.5$ separation distances with the difference in the shear forces between the upper and lower parts of the sphere becoming more pronounced for smaller separation distances. The change in the relative magnitudes of the shear stresses between the top and bottom parts of the sphere with separation distance is again observed. The clockwise direction is considered positive for the shear stress on the top of the sphere and the anti-clockwise direction is considered positive for the shear stress on the bottom. We focus on $S = 1.5$ in the following discussion. On an average, the shear stress is higher on the lower part of the sphere compared to the upper part, particularly between $\theta = -\pi$ to $\theta = -1.8$ radians and between $\theta = -1.3$ to $\theta = -0$ radians. For these two ranges of angles the Y -component of the forces will be significant, while for the range of angles for which shear stress on the upper part is higher the Y -component of the forces will be small. Thus, owing to their inclinations with the X -axis, the shear forces on the two lower parts have a significant component in the Y -direction and thus contribute to both the lift (parallel to the X -axis) and drag (parallel to the Y -axis), whereas the shear force on the top will have mostly have a small component in the Y -direction and thus contributes mainly to the drag. Thus, the shear forces, like the pressure forces, contribute to the repulsion of the two spheres.

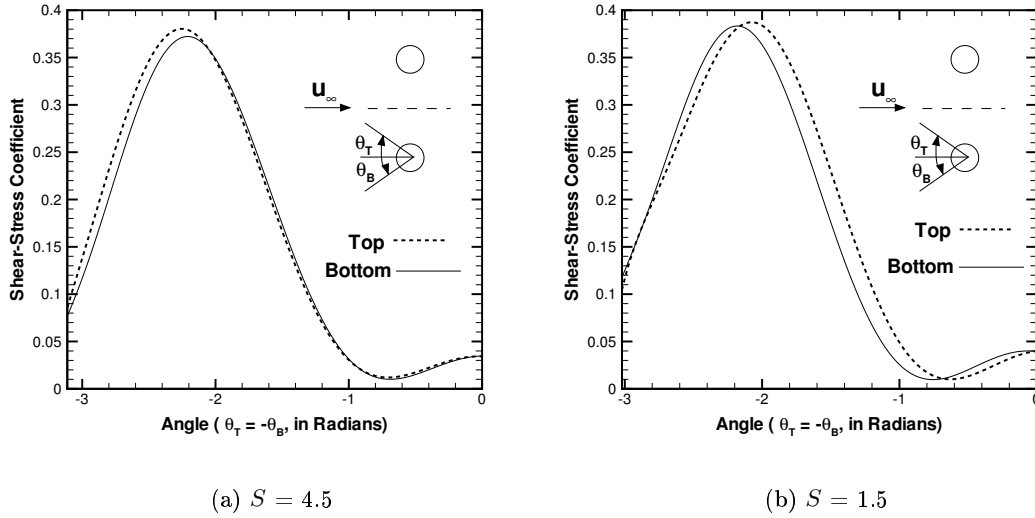


Figure 4.21: Distribution of shear stress coefficient

All the above observations are in agreement with those of Kim *et al.* (1993) and show that the computer code accurately reproduces the interaction effects between multiple bluff bodies.

4.4 Single and Interacting Droplet Ignition

Ignition of a single ethanol drop and of a pair of identical ethanol droplets in tandem configuration was numerically simulated. The inter-droplet separation distance for the two droplet case was three times the initial droplet diameter because strong interactions are expected at this separation (Chiang *et al.*, 1990). The schematic of the flow configuration and the grid around the drop for the single drop case is similar to that of Figure 4.11. Figure 4.17 closely corresponds to the schematic for the two droplet case except that here the droplets are placed in tandem configuration (the second droplet is placed downstream behind the first droplet) rather than side-by-side since in this configuration the downstream droplet will be more strongly influenced by the wake of the lead droplet. A detailed chemical reaction mechanism with 342 elementary reactions between 38 different chemical species was used for both the single droplet and for the interacting droplet cases (Chevalier, 1993). Transport

Parameter	Value	Parameter	Value
Free-Stream Gas-phase Temperature	1500 K	Initial Drop Diameter	96.26 μm
Free-Stream Gas-phase Pressure	10^6 Pa	Initial Drop Temperature	300 K
Free-stream Nitrogen Mass Fraction	0.76	Initial Drop Velocity	25 m/s
Free-stream Oxygen Mass Fraction	0.24		

Table 4.3: Initial values used for ethanol droplets

properties in the gas phase are calculated from the kinetic theory of gases (Hirschfelder *et al.*, 1964) and specific enthalpies and heat capacities are calculated using the polynomial fits of *JANAF* tables (Bureau of Standards, 1971). Some of the physical parameters used in the study are shown in Table 4.3. Three *O*-grids were generated, the first two inside the drops and the third one around the drops. A cross-sectional view of the block structure and the grid around the drop is also shown in Figure 4.22.

These parameters correspond to an initial Reynolds number based on drop diameter of 100. As the drop decelerates due to drag forces acting on it and its diameter changes due to vaporization the Reynolds number keeps decreasing with time from its initial value of 100. Figure 4.22 shows the variation of maximum temperature in the computational domain with time for the two cases. If the location of the maximum slope of temperature is used as a criterion for the ignition delay then the ignition delay for the single droplet is 2.5 ms while for the pair of interacting droplets the ignition delay is 3.5 ms.

Figure 4.23 shows the ignition delay times from Sangiovanni and Kesten (1977) for monodispersed streams of $200\mu\text{m}$ droplets as a function of fuel type and gas phase temperature. In Figure 4.23 circles refer to a free stream temperature of 1452 K and a free stream velocity of 136 m/s. Squares and triangles refer to a free stream temperature and a free stream velocity of 1363 K and 134 m/s and 1242 K and 133 m/s respectively. The experiments were carried out at atmospheric pressure.

The ignition delay for $200\mu\text{m}$ butyl alcohol droplets at an initial temperature of 1452 K and at a free-stream gas velocity of 136 m/s is around 3 ms for an interdroplet separation distance of 3 droplet diameters. This compares favorably with the present calculation of

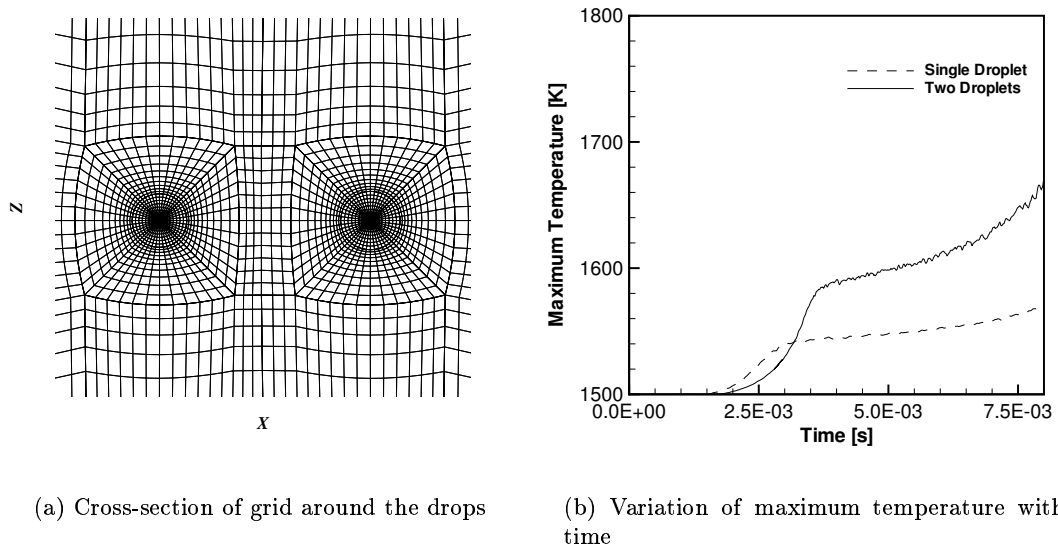


Figure 4.22: Grid around drops and the variation of maximum temperature with time

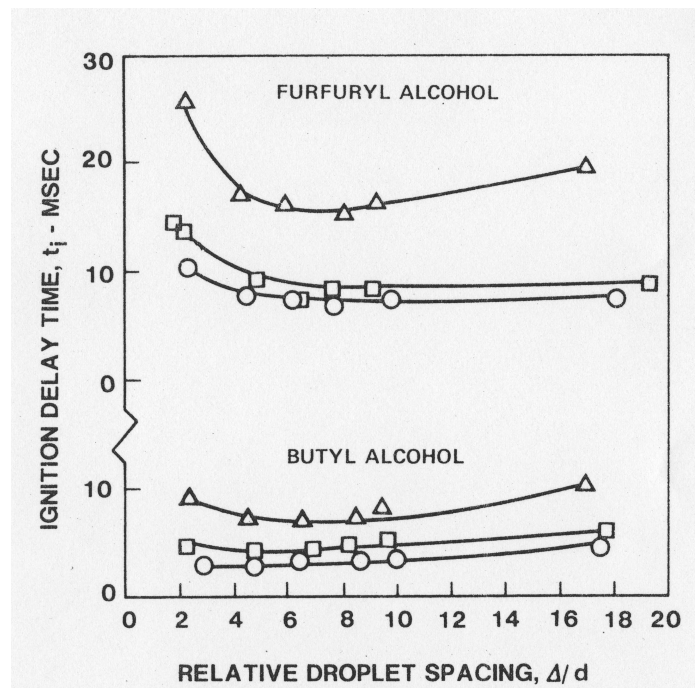
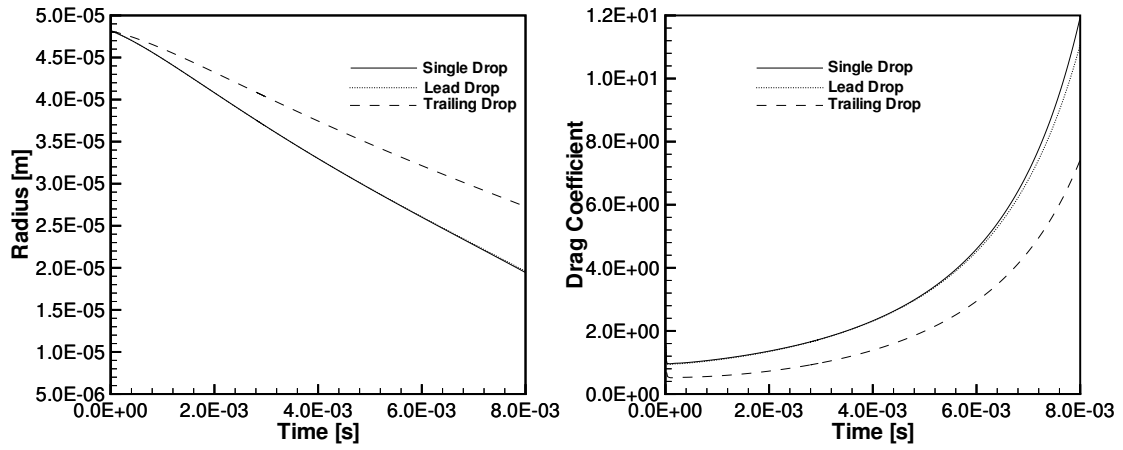


Figure 4.23: Ignition delay times from Sangiovanni and Kesten (1977)

ignition delay time of 3.5 ms. The present computations were carried out for a lighter fuel (ethanol) at a much higher pressure (10 bar) and both of these factors tend to decrease the ignition delay (Aggarwal, 1998). However this effect is more than offset by the smaller free stream velocities used in the present study (25 m/s). Due to smaller free stream velocity the droplet vaporization rates are smaller and a longer time is required for the fuel concentration to build up in the gas phase. Thus the smaller free stream velocity, used in the present study, contributes to a longer ignition delay.

Figure 4.24 shows the variation of droplet radius and drag coefficients as a function of time. No appreciable difference is found in the variation of droplet radius and drag coefficients between the single droplet and lead droplet cases. This is expected as the downstream (trailing) droplet will not influence the flow field upstream. The effect of droplet interaction will be felt downstream by the trailing droplet. This is clearly seen in Figure 4.24 where the variation of droplet radius and drag coefficients is different for the trailing droplet as compared to the lead droplet. The radius of the trailing droplet decreases more slowly as compared to the lead droplet suggesting lower vaporization rates due to the buildup of fuel concentration in the wake of the lead droplet. The Reynolds number will also show the same trend. The Reynolds number of the trailing droplet will be higher and its rate of decrease will be slower compared to that of the leading droplet. Since the drag coefficient over solid spheres is inversely proportional to Reynolds number it can be expected that the drag coefficient for the leading drop will be higher than that of the trailing drop as is readily confirmed in Figure 4.24.

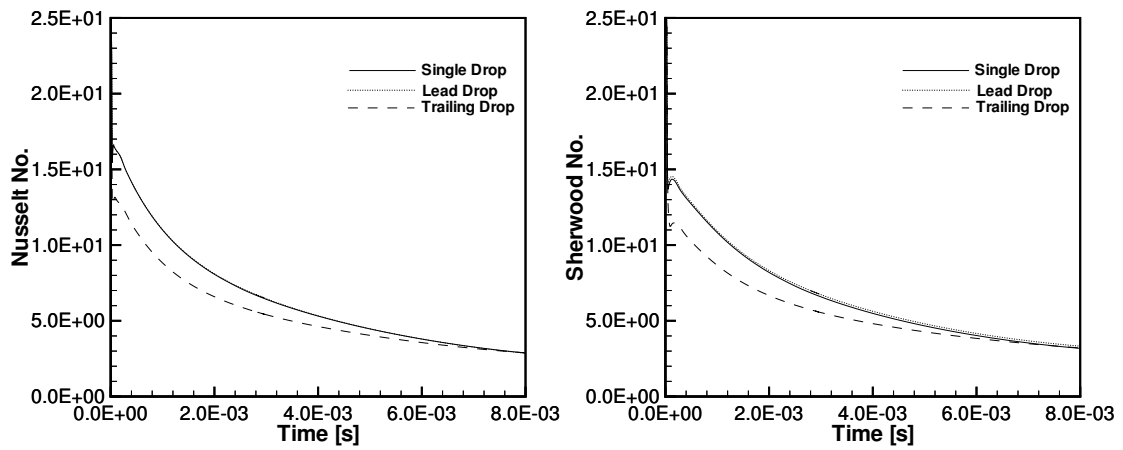
Figure 4.25 shows the comparison of droplet Nusselt and Sherwood numbers as a function of time. The difference between the leading and trailing drop Nusselt and Sherwood numbers decreases with time suggesting that the interaction effects on heat and mass transfer rates decrease as the droplets continue to vaporize. This is expected because as the droplets continue to vaporize their size becomes smaller, and since the absolute distance between the two droplets l is held constant, the ratio of the relative distance between the droplets l/d increases. After some time the relative distance l/d is so large that interaction effects are



(a) Droplet radius as a function of time

(b) Droplet drag as a function of time

Figure 4.24: Comparison of droplet radius and drag coefficients



(a) Nusselt no. as a function of time

(b) Sherwood no. as a function of time

Figure 4.25: Comparison of Nusselt and Sherwood numbers

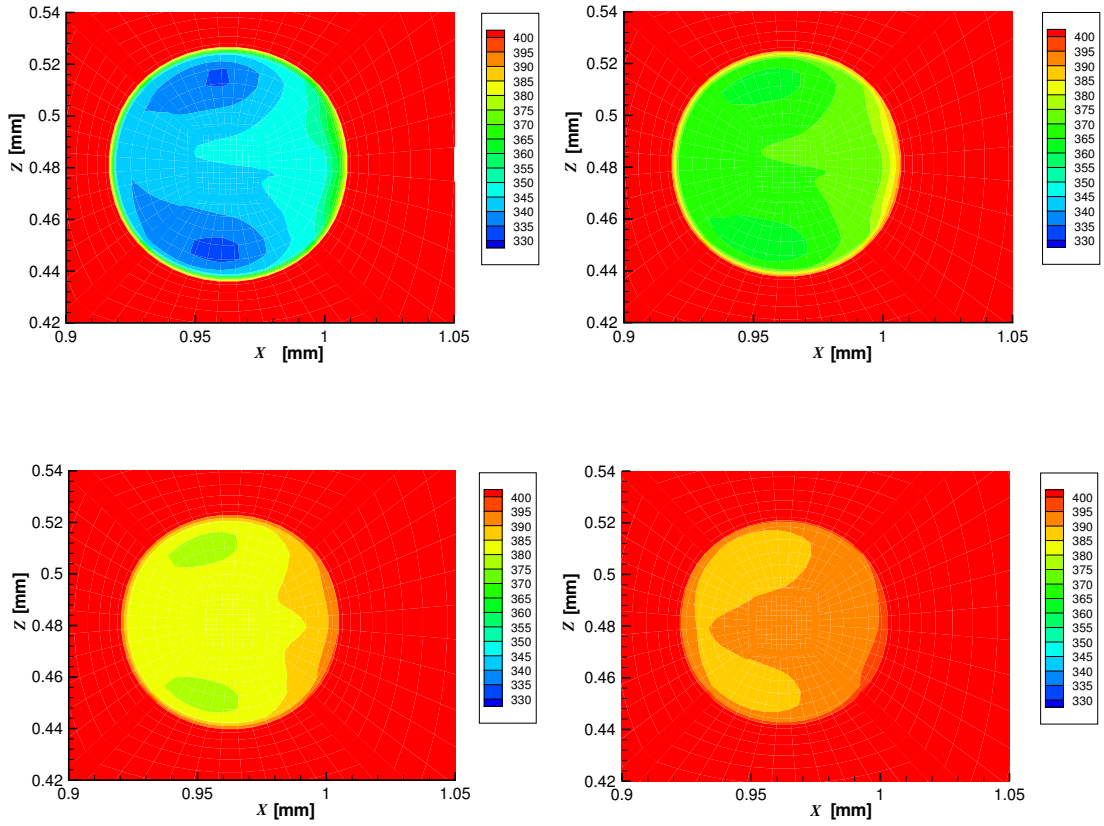


Figure 4.26: Zoomed view of contour plots of temperature for single droplet at different time instants: top left 0.5 ms, top right 1.0 ms, bottom left 1.5 ms and bottom right 2.0 ms

negligible and the droplets behave independent of each other.

Thus it can be seen that interaction effects can cause the trailing droplet heat and mass transfer rates to be quite different during the initial periods of its lifetime depending on the relative distance between the leading and trailing droplets.

Figure 4.26 shows the temperature distribution in and around the droplet (for the single droplet case) in the $X - Z$ plane at different time instants during its initial heatup period. It is seen that the droplet heats up quickly in about 2 ms. The temperature inside the droplet evolves from a non-uniform distribution at 0.5 ms to a more or less uniform distribution at at 2 ms. The temperatures inside the droplet are not exactly symmetric about the centerline which may be due to numerical diffusion inside the droplets. In all the four time instances

shown the highest temperatures occur in a thin layer in the rear of the droplet whereas regions of lowest temperature are concentrated in two lobes near the front of the droplet. A large portion of the droplet seems to be at more or less at the same temperature at any given instant of time.

Figure 4.27 shows the temperature distribution in and around the droplets (for the interacting droplets case) in the $X - Z$ plane at different time instants during its initial heatup period. The magnification of Figure 4.27 is less than the single droplet case in order to resolve both the droplets. Overall the same trends as the single droplet case are observed here too. The temperature of the downstream droplet is less than that of the lead droplet as its rate of heat transfer is reduced by the wake of the latter.

Figure 4.28 shows the contour plots of temperature in the $X - Z$ plane at the instant of ignition for the single drop and Figure 4.29 shows the contour plots of temperature in the $X - Z$ plane at the instant of ignition for the interacting drops cases. The white circles indicate the droplets.

The instant of ignition is determined from Figure 4.22 to be 2.5 ms for the single drop case and 3.5 ms for the interacting drops case. The droplet is placed approximately at 1.0 mm from the inlet for both cases. No appreciable difference is seen between the location of ignition between the two cases which occurs around 30 droplet diameters downstream. However the temperature at the ignition location for the interacting drop case is clearly higher compared to the single drop case. This agrees with Figure 4.22 which shows that higher maximum gas temperatures are obtained for the interacting drop case as compared to the single drop case.

Figure 4.30 and 4.31 show the distribution of temperature in the $X - Z$ plane at 6.5 ms. The temperatures are higher in general for the interacting droplet case as compared to the single droplet case. This is in agreement with Figure 4.22 where the maximum gas phase temperature for the interacting droplet case is higher than the maximum gas phase temperature for the single droplet case. It can also be seen from Figures 4.30 and 4.31 that the flame moves closer to the droplets at 6.5 ms as compared to the instant of ignition at 3.5 ms for the interacting droplet case (Figure 4.29) and at 3 ms for the single droplet case (Figure 4.28).

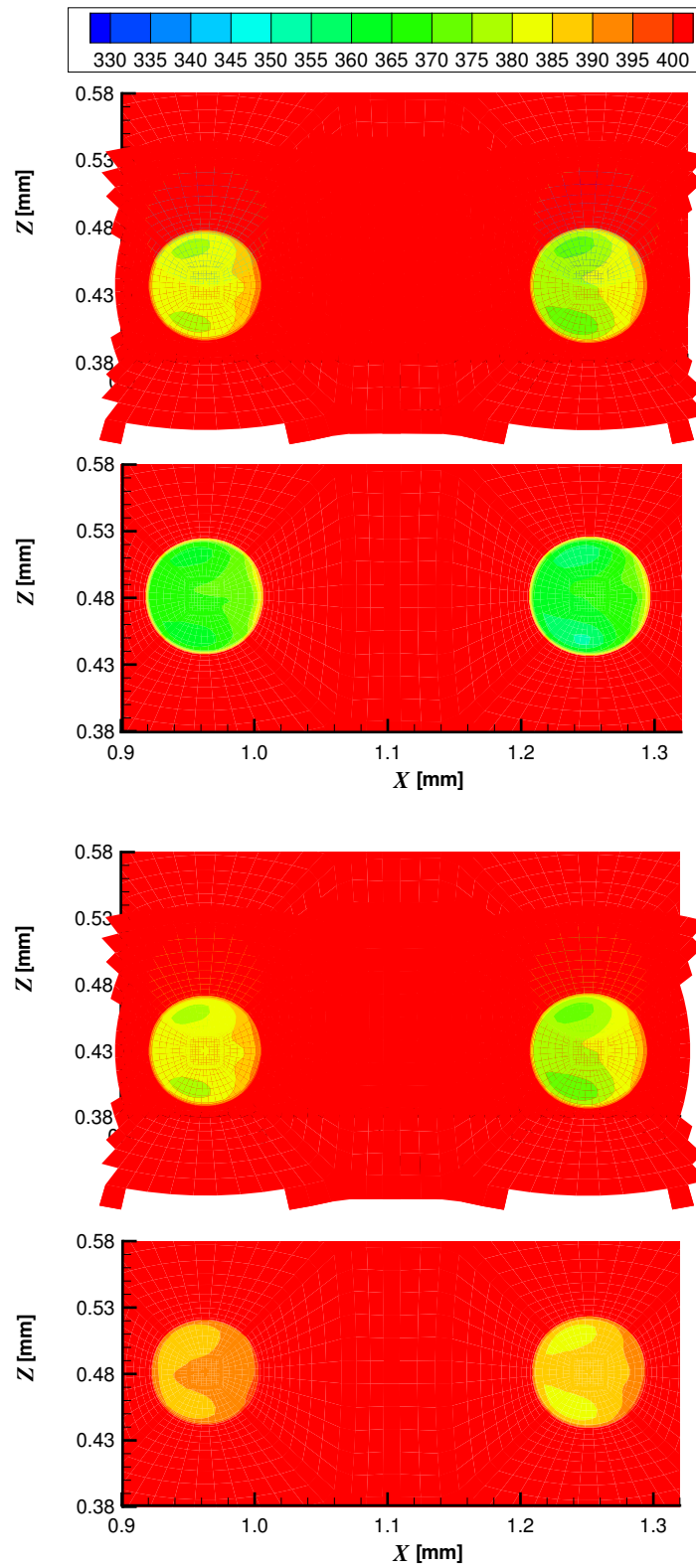


Figure 4.27: Zoomed view of contour plots of temperature for interacting droplets at different time instants: from top to bottom 0.5 ms, 1.0 ms, 1.5 ms and 2.0 ms

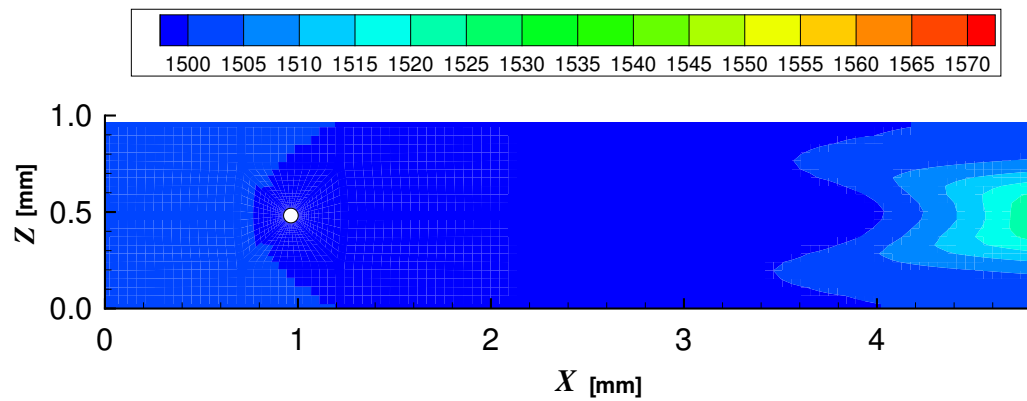


Figure 4.28: Contour plot of gas temperature at ignition: single droplet

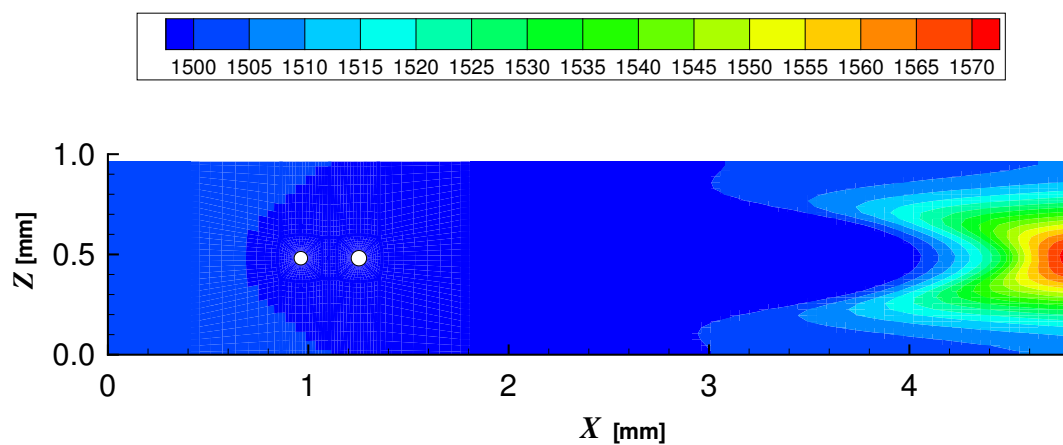


Figure 4.29: Contour plot of gas temperature at ignition: interacting droplets

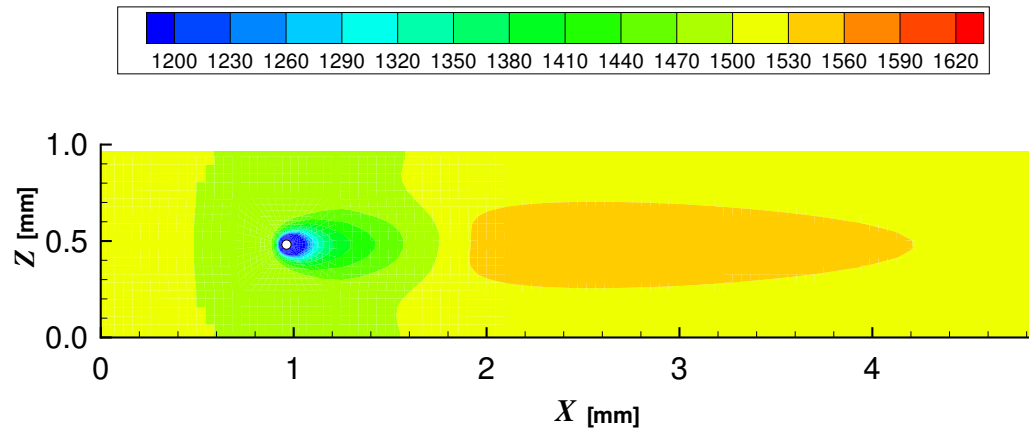


Figure 4.30: Contour plots of gas temperature at 6.5 ms: single droplet

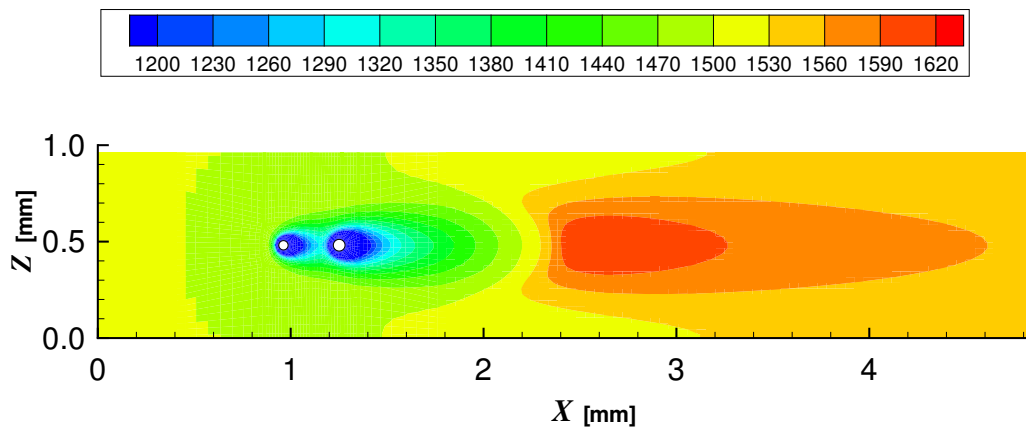


Figure 4.31: Contour plots of gas temperature at 6.5 ms: interacting droplets

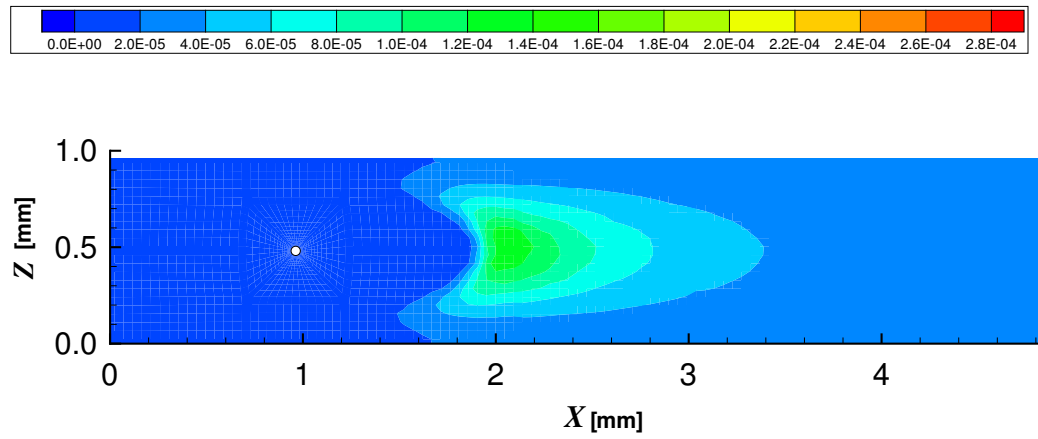


Figure 4.32: Contour plots of OH mass fraction at 6.5 ms: single droplet

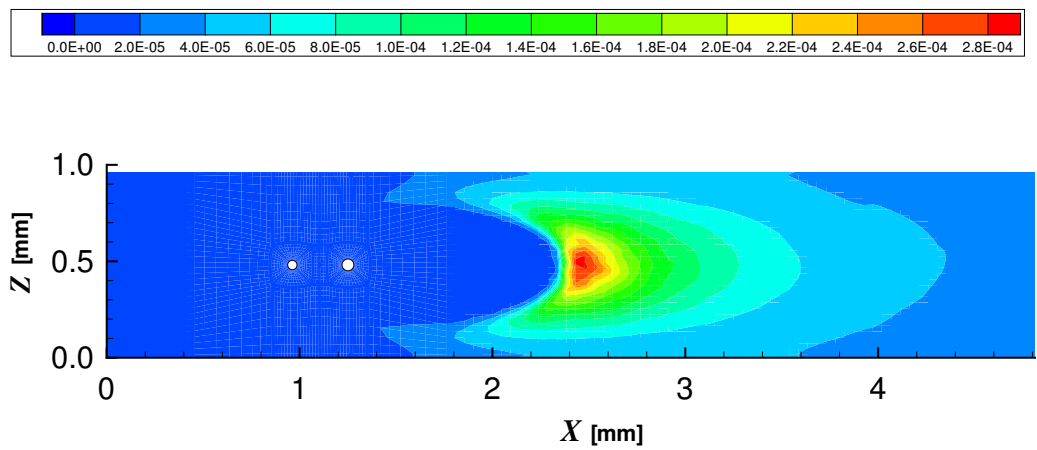
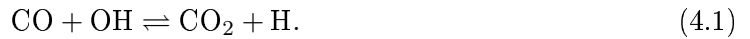


Figure 4.33: Contour plots of OH mass fraction at 6.5 ms: interacting droplets

Figures 4.32 and 4.33 show the distribution of OH radical in the $X - Z$ plane at 6.5 ms. The white circles indicate the droplets. It can be seen from the OH radical distribution that the flame height is bigger for the interacting droplets case as compared to the single droplet case. In addition, the concentrations of the OH radical are higher in the interacting droplets case. Since OH participates in the final oxidation of CO and H₂ into CO₂ and H₂O, where a large part of heat release associated with combustion occurs (Glassman, 1996), higher temperatures are expected in the interacting droplets case. This agrees with higher temperatures found in Figure 4.29 for the interacting droplets case as compared to Figure 4.28 for the single drop case.

Figures 4.34 and 4.35 show the distribution of CO and Figures 4.36 and 4.37 show the distribution of CO₂ in the $X - Z$ plane at 6.5 ms. The distribution of CO is notably different as compared to that of CO₂. At this instance (6.5 ms) the regions of high concentrations of CO₂ are further downstream of the droplets as compared to that of CO. This may be expected since the oxidation of CO into CO₂ is a slow reaction which consumes a lot of energy.



Additionally, since both the OH and CO concentrations in the interacting droplet case are higher than that for the single droplet case the concentrations of CO₂ for the interacting droplet case would be higher too as confirmed in Figure 4.37. This is also consistent with the observation that the concentration of OH is also higher in the interacting droplets case as compared to the single droplet case.

Figures 4.38 and 4.39 show the distribution of formaldehyde in the $X - Z$ plane at 6.5 ms. In general, higher concentrations of formaldehyde are seen in the interacting droplet case as compared to the single droplet case. Particularly, a higher concentration of formaldehyde can be seen between the two droplets in the interacting droplets case. This may form due to incomplete combustion due to a higher concentration of the fuel vapour in the interacting

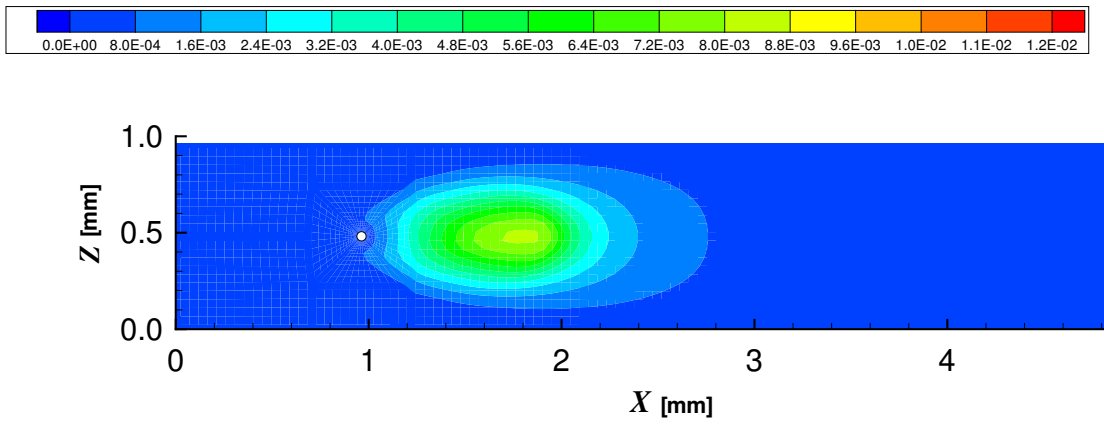


Figure 4.34: Contour plots of CO mass fraction at 6.5 ms: single droplet

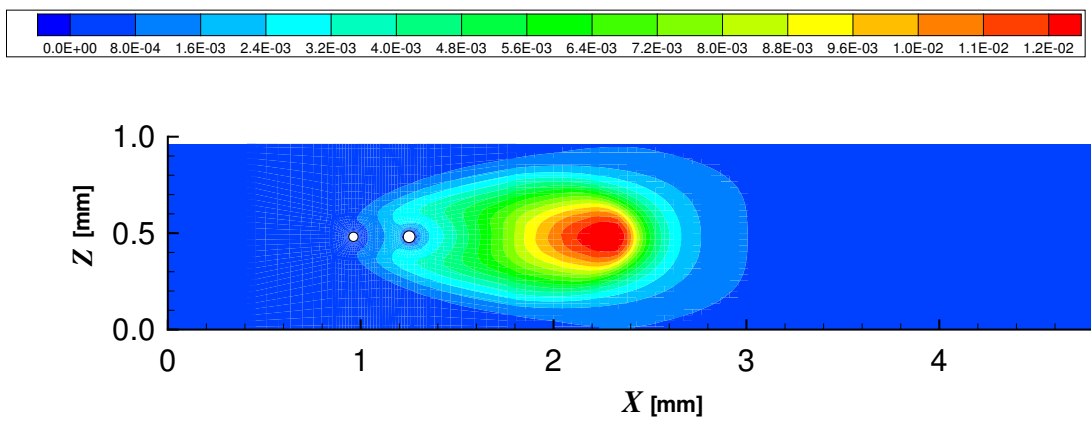


Figure 4.35: Contour plots of CO mass fraction at 6.5 ms: interacting droplets

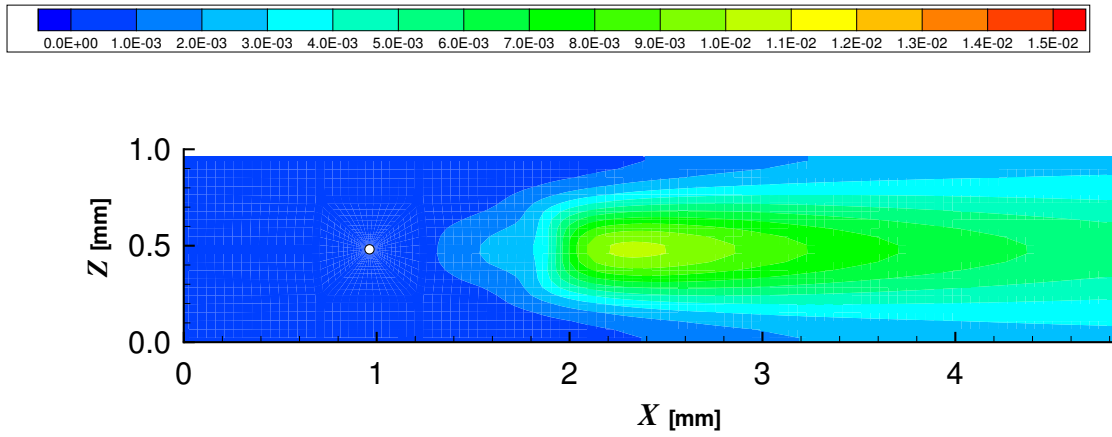


Figure 4.36: Contour plots of CO₂ mass fraction at 6.5 ms: single droplet

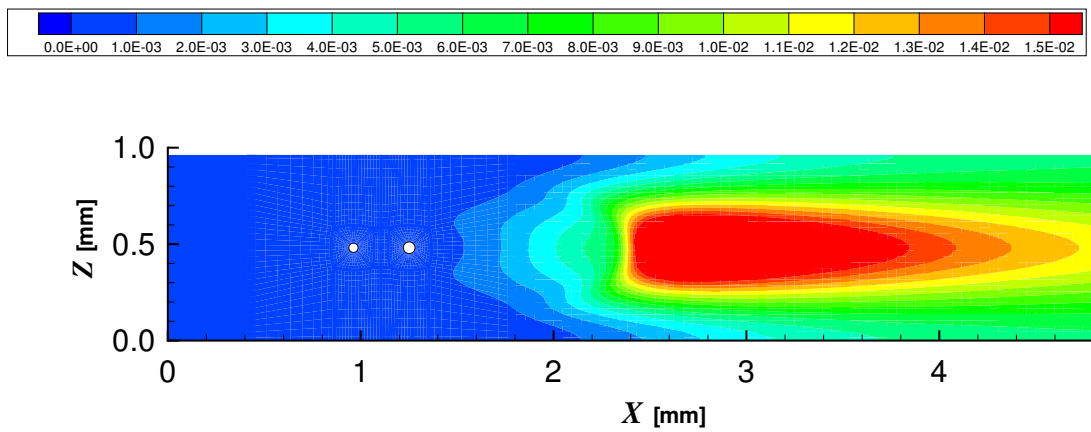


Figure 4.37: Contour plots of CO₂ mass fraction at 6.5 ms: interacting droplets

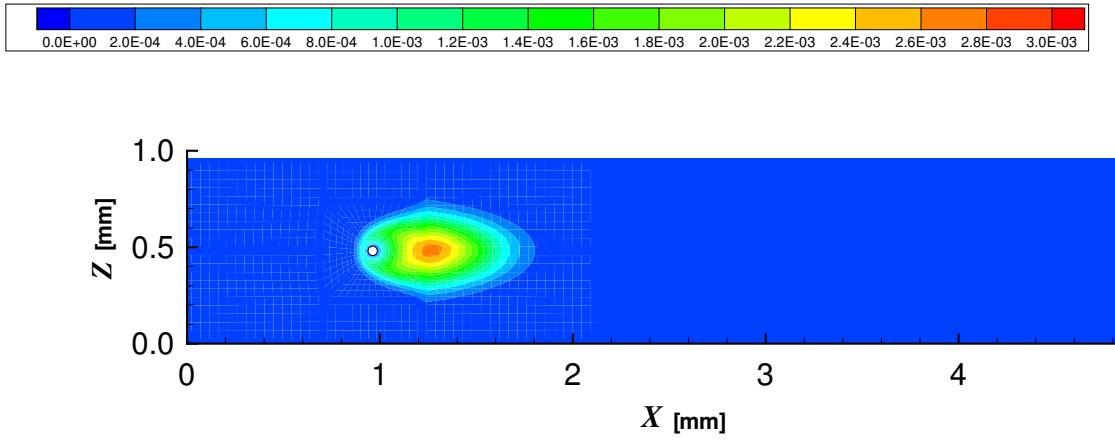


Figure 4.38: Contour plots of CH_2O mass fraction at 6.5 ms: single droplet

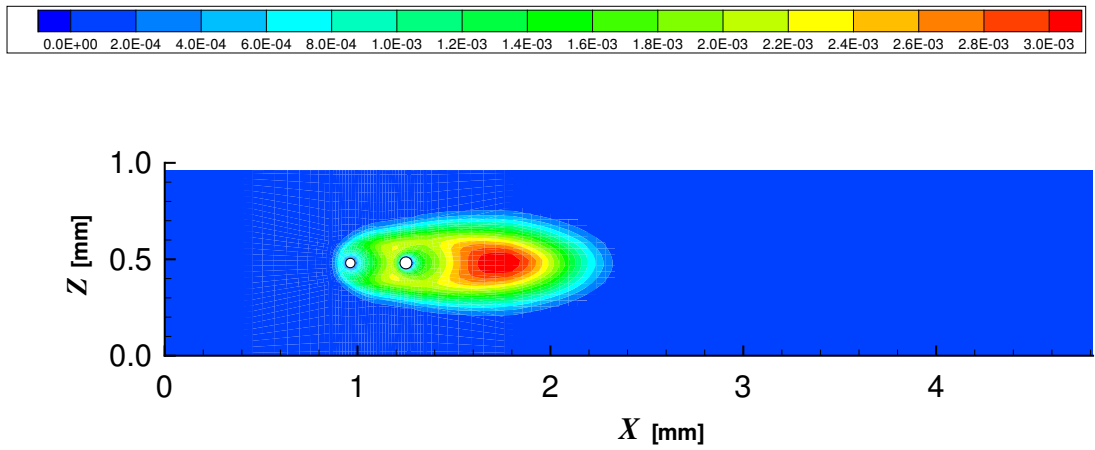


Figure 4.39: Contour plots of CH_2O mass fraction at 6.5 ms: interacting droplets

droplets case. A higher concentration and a bigger envelope of formaldehyde is also observed in the wake of the downstream droplet as compared to the single droplet. Since formaldehyde is a pollutant, high concentrations of formaldehyde are undesirable and should be avoided. When the interdroplet separation distance is small, higher concentrations of formaldehyde are likely to occur compared to when the interdroplet separation distance is large.

Chapter 5

Conclusions

A numerical method has been developed to simulate droplet interaction effects during vaporization and ignition using moving grids with finite volume discretization.

It is shown that SCL is just one equation, out of a set of additional conservation equations, which have to be satisfied on moving grids. By computing identical flows on both stationary and moving grids it is shown that when all the additional conservation equations are satisfied the moving grid solution is identical to the stationary grid solution while neglecting all additional conservation equations except the SCL produces erroneous results on moving grids. This point is further emphasized by computing flows on very rapidly moving grids and showing that satisfying all the additional conservation equations gives reasonable agreement with the stationary grid solution while neglecting additional conservation equations may even produce unphysical solutions. Thus even though SCL is satisfied, by neglecting other equations of this set, errors in the form of artificial sources/sinks may still accumulate, on moving grids, leading to erroneous solutions for unsteady computations. In light of the above we recommend using numerical methods, for moving grids, that satisfy all the additional conservation equations.

A modified algorithm for the application of multigrid technique on moving grids was presented in which the grid movement is not known *a priori* and is implicitly calculated for each

iteration at any given time-step. Problems involving phase change present additional difficulties (associated with the boundary conditions) for multigrid implementation which were also discussed. The modified multigrid technique was applied to an example problem of a liquid drop vaporizing in a convective gas flow whereby moving grids are used to account for the change in drop size due to vaporization. Computational results were presented to show that on moving grids, when the grid movement is not known *a priori* and is implicitly calculated, the multigrid technique can be implemented with minor modifications to obtain convergence acceleration.

The ability of the code to accurately simulate the interaction between droplets was assessed. It was shown that the computer code accurately reproduces the interaction effects between multiple bluff bodies. Combustion of a single ethanol drop and of a pair of identical ethanol droplets in tandem configuration was numerically simulated. It was shown that interaction effects can cause the trailing droplet heat and mass transfer rates to be quite different during the initial periods of its lifetime. The predicted ignition delay for the interacting droplet case compares favorably with experiments.

The computer code was developed to enable parametric studies of droplet interactions. It allows a lot of flexibility in studying three dimensional interactions between droplets. The number of droplets as well as the spatial arrangement of the droplets can be changed without any modification of the code. Similarly, the fuel (chemical species of the droplets) and the detailed chemical reaction mechanism used for a particular fuel-air mixture can be changed easily. The code is highly optimized to run on a variety of platforms and fully parallelized on shared memory and distributed memory architectures allowing considerable savings in computational costs. The improved moving grid technique and the extended multigrid algorithm incorporated in the code gives it a computational advantage for studying droplet vaporization and ignition problems.

Bibliography

- [1] Aggarwal, S. K. (1998): A review of spray ignition phenomena: present status and future research. *Prog. Energy Combust. Sci.*, 24, 565-600
- [2] Annamalai, K., Ryan, W. (1991): Evaporation of arrays of drops using the point source method, *Central States Section of the Combustion Institute Conference Proceedings*, No. 91-56, 347-354
- [3] Annamalai, K. , Ryan, W. (1992): Interactive processes in gasification and combustion. Part 1: Liquid drop arrays and clouds. *Prog. Energy Combust. Sci.*, 18, 221-295
- [4] Aouina, Y., Gutheil, E., Maas, U., Riedel, U. , Warnatz, J. (2001): Mathematical modeling of droplet heating, vaporization, and ignition including detailed chemistry. *Combust. Sci. and Tech.*, 173, 1-29
- [5] Arnone, A., Pacciani, R., Sestini, A. (1995): Multigrid computations of unsteady rotor-stator interaction using the Navier-Stokes equations. *J. Fluids. Engng.*, 117, 647-652
- [6] Atthasit, A., Biscos, Y. , Lavergne, G. (2003): A rectilinear droplet stream study: Influence of lateral interaction on droplet dynamical behaviour. *Nineth International Conference on Liquid Atomisation and Spray Systems (ICLASS)*, July 13-17, Sorrento, Italy
- [7] Batchelor, G. K., Green, J. T. (1972): The hydrodynamic interaction of two small freely-moving spheres in a linear flow field, *J. Fluid Mech.*, 56, 375-400

- [8] Bellan, J., Cuffel, R. (1983): A theory of non-dilute spray evaporation based upon multiple drop interactions. *Combust. Flame*, 51, 55-67
- [9] Bellan, J., Harstad, K., (1987): Analysis of the convective evaporation of nondilute clusters of drops. *Int. J. Heat Mass Transfer*, 30, 125-136
- [10] Bureau of Standards, Washington, D. C. (1971): *JANAF Thermochemical Tables*, 2nd Edition.
- [11] Böhm, M., Wechsler, K., Schäfer, M. (1998): A parallel moving grid multigrid method for flow simulation in rotor-stator configurations. *Int. J. Numer. Meth. Engng.*, 42, 175-189
- [12] Cao, W., Huang, W., Russell, R. D. (2002): A moving mesh method based on the geometric conservation law. *SIAM J. Sci. Comput.*, 24, 118-142
- [13] Chen S. J., Tong, A. Y. (1988): Application of elliptic grid generation technique to the solution of hydrodynamics and heat transfer of droplet arrays at intermediate Reynolds numbers. *Int. J. Heat Mass Transfer*, 31, 1063-1072
- [14] Chevalier, C. (1993): *Entwicklung eines detaillierten Reaktionsmechanismus zur Modellierung der Verbrennungsprozesse von Kohlenwasserstoffen bei Hoch- und Niedertemperaturbedingungen*. Ph.D Thesis, Universität Stuttgart, Stuttgart
- [15] Chiang, C. H., Raju, M. S., Sirignano, W. A. (1990): Numerical analysis of convecting, vaporizing fuel droplet with variable properties. *Int. J. Heat Mass Transfer*, 35, 1307-1324
- [16] Cornish, A. R. H. (1965): Note on the minimum possible rate of heat transfer from a sphere when other spheres are adjacent to it. *Trans. Inst. Chem. Eng.*, 43, T332-T333
- [17] Crumpton, P. I., Giles, M. B. (1997): Implicit time accurate solutions on unstructured dynamic grids. *Int. J. Numer. Meth. Fluids*, 25, 1285-1300

- [18] Demirdžić, I., Perić, M. (1988): Space conservation law in finite volume calculations of fluid flow. *Int. J. Numer. Meth. Fluids*, 8, 1037-1050
- [19] Demirdžić, I., Perić, M. (1990): Finite volume method for prediction of fluid flow in arbitrarily shaped domains with moving boundaries. *Int. J. Numer. Meth. Fluids*, 10, 771-790
- [20] Devarakonda, V. , Ray, A. K. (2003): Effect of inter-particle interactions on evaporation of droplets in a linear array. *J. Aerosol Sci.*, 34, 837-857
- [21] Durst, F., Schäfer, M. (1996): A parallel block-structured multigrid method for the prediction of incompressible flows. *Int. J. Numer. Meth. Fluids*, 22, 549-565
- [22] Dwyer, H. A., Stapf, P. , Maly, R. (2000): Unsteady vaporization and ignition of a three-dimensional droplet array. *Combust. Flame*, 121, 181-194
- [23] Farhat, C., Geuzaine, P., Grandmont C. (2001): The discrete geometric conservation law and the nonlinear stability of ALE schemes for the solution of flow problems on moving grids. *J. Comput. Phys.*, 174, 669-694
- [24] Fedoseeva, N. V. (1973): Kinetics of evaporation of a droplet system. *Adv. Aerosol Phys.* 3, 35-42
- [25] Ferziger, J.H., Perić, M. (1996): *Computational methods for fluid dynamics*. Springer, Berlin
- [26] Fuchs, N. A. (1959): *Evaporation and droplet growth in gaseous media*. Pergamon Press, New York
- [27] Geuzaine, P., Grandmont, C., Farhat, C. (2003): Design and analysis of ALE schemes with provable second-order time-accuracy for inviscid and viscous flow simulations. *J. Comput. Phys.*, 191, 206-227
- [28] Glassman, I. (1996): *Combustion*, Third Edition, Academic Press, San Diego, CA

- [29] Guillard, H., Farhat, C. (2000): On the significance of the geometric conservation law for flow computations on moving meshes. *Comput. Methods Appl. Mech. Engrg.*, 190, 1467-1482
- [30] Haywood, R. J. (1992): *Dynamics and energetics of deformable evaporating droplets at intermediate Reynolds numbers*. PhD Thesis, University of Waterloo
- [31] Hirschfelder, J. O., Curtiss, C. F., Bird, R. B. (1964): *Molecular Theory of Gases and Liquids*. John Wiley & Sons Inc., New York
- [32] Huang, L. J., Ayyaswamy, P. S., Sripada, S. S. (1996): Condensation on a spray of water drops: a cell model study-I transport quantities. *Int. J. Heat Mass Transfer*, 39, 3781-3790
- [33] ICEM CFD HEXA from *ICEM CFD Engineering*, 2855 Telegraph Ave., 501, Berkeley, CA 94705
- [34] Inuma, K. (1962): Flame propagation in liquid fuel droplet arrays with forced convection. *Combust. Flame*, 6, 127-129
- [35] Jeffrey, D. J., Onishi, Y. (1984): Calculation of the resistance and mobility functions for two unequal rigid spheres in low Reynolds number flows, *J. Fluid Mech.*, 139, 261-290
- [36] Johnson, T. A., Patel, V. C. (1999): Flow past a sphere up to a Reynolds number of 300, *J. Fluid Mech.* 378, 19-70
- [37] Kadowaki, T., Maruta, K., Kobayashi, H., Hasegawa, S., Niioka, T. (1996): Ignition experiment on droplet matrix in microgravity. *Microgravity Sci. Tech.*, 4, 269-274
- [38] Kamakoti, R., Shyy, W. (2004): Evaluation of geometric conservation law using pressure-based fluid solver and moving grid technique. *Int. J. Numer. Meth. Heat Fluid Flow*, 14, 849-863

- [39] Kee, R. J., Warnatz, J., Miller, J. A. (1983): *A fortran computer code package for the evaluation of gas-phase viscosities, conductivities and diffusion coefficients. Report SAND83-8209*, Sandia National Laboratory, Livermore
- [40] Khosla, P.K., Rubin, S.G. (1974): A diagonally dominant second-order accurate implicit scheme. *Computer Fluids*, 2, 207-209
- [41] Kim, I., Elghobashi, S. E., Sirignano, W. A. (1993): Three-Dimensional Flow Over Two Spheres Placed Side-by-Side. *J. Fluid Mech.*, 246, 465-468
- [42] Kordula, W., Vinokur, M. (1983): Efficient computation of volume in flow predictions. *AIAA J.*, 21, 917-918
- [43] Labowsky, M. (1976): The effects of nearest neighbor interactions on the evaporation rate of cloud particles. *Chem. Eng. Sci.*, 31, 803-813
- [44] Labowsky, M. (1977): A formalism for calculating the evaporation rates of rapidly evaporating interacting particles. *Combust. Sci. Technol.*, 18, 141-145
- [45] Labowsky, M. (1980): Calculation of burning rates of interacting fuel droplets, *Combust. Sci. Technol.*, 22, 217-226
- [46] Lafaurie B., Nardone C., Scardovelli R., Zaleski S, Zanetti, G. (1994): Modelling merging and fragmentation in multiphase flows with SURFER. *J. Comput. Phys.*, 113, 134-147
- [47] Lehnhäuser, T., Schäfer, M. (2001): Improved linear interpolation practice for finite-volume schemes on complex grids. *Int. J. Numer. Meth. Fluids*, 1, 1-21
- [48] Lide, D. R. (1997): *CRC handbook of chemistry and physics*. CRC Press LLC, New York
- [49] Mikami, M., Kato, H., Sato, J., Kono, M. (1994): Interactive combustion of two droplets in microgravity. *Twenty-Fifth Symposium (International) on Combustion* 431-438

- [50] Morton, S.A., Melville, R.B., Visbal M.R. (1997): Accuracy and coupling issues of aeroelastic Navier-Stokes solutions of deforming meshes, *AIAA Paper97-1085*, 38th AIAA Structures, presented at Structural Dynamics and Materials Conference, Kissimmee, Florida, April 7-10
- [51] Mukhopadhyay, A., Sanyal, D. (1999): A study of thin-film quasisteady spherically-symmetric combustion of multicomponent fuel droplets: part-I modelling for droplet surface regression and non-unity gas-phase Lewis number. *Int. J. Energy Res.*, 23, 963-977
- [52] Mukhopadhyay, A., Sanyal, D. (1999): A study of thin-film quasisteady spherically-symmetric combustion of multicomponent fuel droplets: part-II parametric studies. *Int. J. Energy Res.*, 23, 979-987
- [53] Muralidhar, K., Sundararajan, T. (1995): *Computational fluid flow and heat transfer*. Narosa Publishing House, New Delhi
- [54] Nobari, M. R. H., Tryggvason, G. (1996): Head-on collision of drops - A numerical investigation. *Phys. Fluids*, 8, 29-42
- [55] Nobari, M. R. H., Tryggvason, G. (1996): Numerical simulations of three-dimensional drop collisions. *AIAA J.*, 34, 750-755
- [56] Nohara, H., Maruta, K., Hasegawa, S., Kobayashi, H., Niioka, T. (2000): Microgravity ignition experiment on a droplet array in high-temperature low-speed airflow. *Combust. Sci. Tech.*, 153, 169-178
- [57] Nuruzzaman, A. S. M., Hedley, A. B., Beer, J. M. (1970): Combustion rates in self-supporting flames on monosized droplet streams. *J. Inst. Fuel*, 301-310
- [58] Nuruzzaman, A. S. M., Hedley, A. B., Beer, J. M. (1970): Combustion rates in self-supporting flames on monosized droplet streams. *13th Symposium (International) on Combustion*, 787-799
- [59] Patankar, S. V. (1980): *Numerical heat transfer and fluid flow*. Hemisphere Publishing Corporation

- [60] Patankar, S. V., Spalding D. B. (1972): A calculation procedure for heat, mass and momentum transfer in three-dimensional parabolic flows. *Int. J. Heat Mass Transfer*, 15, 1787-1806
- [61] Patnaik, G. (1986): *A numerical solution of droplet vaporization with convection*. Ph.D Dissertation, Carnegie-Mellon University, Dept. of Mechanical Engineering
- [62] Perić, M. (1985): *A finite volume method for the prediction of three-dimensional fluid flow in complex ducts*. PhD Thesis, University of London
- [63] Poinso, T., Veynante, D. (2001): *Theoretical and numerical combustion*. R. T. Edwards Inc., Philadelphia, USA
- [64] Press, W. H., Teukolsky, S. A., Vetterling, W. T., Flannery, B. P. (1992): *Numerical recipes in Fortran 77*, Second Edition, Cambridge University Press, Cambridge
- [65] Raju, M. S., Sirignano, W. A. (1987): Unsteady Navier-Stokes solution for two vaporizing droplets. *AIAA Aerospace Sciences Meeting*, Paper 87-0300
- [66] Raju, M. S., Sirignano, W. A. (1990): Interaction between two vaporizing droplets in an intermediate Reynolds number flow. *Phys. Fluids A*, 2, 1780-1796
- [67] Rangel, R. H., Sirignano, W. A. (1987): Vaporization, ignition and combustion of two parallel fuel droplet streams, *ASME/JSME Thermal Engineering Conference*, 1, 27-34
- [68] Rangel, R. H., Sirignano, W. A. (1988): Unsteady flame propagation in a spray with transient droplet vaporization, *Twentieth-Second Symposium (International) on Combustion*, 1931-1939
- [69] Renaud, F., Chauveau, C., Gokalp, I., Segawa, D., Kadota, T. (2003): Experimental study in microgravity of the vaporization of a 3D droplet array in a high pressure and high temperature environment. *European Combustion Meeting*, Oct. 25-28, Orleans, France

- [70] Reichenbach, R., Squires, D., Penner, S., S. (1962): Flame propagation in liquid-fuel droplet arrays. *8th Symposium (International) on Combustion* 1069-1973
- [71] Reiss, H. (1951): The growth of uniform colloidal dispersions, *J. Chem. Phys.*, 19, 482-489
- [72] Rhie, C.M., Chow, W. L. (1983): A numerical study of the turbulent flow past an isolated airfoil with trailing edge separation. *AIAA J.*, 21, 1525-1532
- [73] Rieber, M., Frohn, A. (1995): Three-dimensional Navier-Stokes simulation of binary collisions between drops of equal size. *J. Aerosol Sci.*, 26, S929-S930
- [74] Samson, R., Deutch, J. M. (1977): Exact solutions for the diffusion controlled rate into a pair of reacting skins. *J. Chem. Phys.*, 67, 847
- [75] Sangiovanni, J. J., Kesten, A. S. (1975): A theoretical and experimental investigation of the ignition of fuel droplets. *Joint meeting of CSS/CI and WSS/CI*, San Antonio, TX, April 21-22
- [76] Sangiovanni, J. J., Kesten, A. S. (1977): Effect of droplet interaction on ignition in monodispersed droplet streams. *16th Symposium (International) on Combustion*, 577-592
- [77] Sangiovanni, J. J., Dodge, L. G. (1978): Observations of flame structure in the composition of monodispersed droplet streams. *17th Symposium (International) on Combustion*, 455-465
- [78] Sanyal, D., Sundararajan, T. (1992): An analytical model of spray combustion for slowly moving fuel drops. *Int. J. Heat Mass Transfer*, 35, 1035-1048
- [79] Sato, J., Konishi, K., Okada, H., Niioka, T. (1986): Ignition process of fuel spray injected into high pressure high temperature atmosphere. *Twenty-First Symposium (International) on Combustion*, 695-702

- [80] Schäfer, M., Meynen, S., Sieber, R., Teschauer, I. (2000): Multigrid methods for coupled fluid-solid problems. presented at *European Congress on Computational Methods in Applied Sciences and Engineering ECCOMAS 2000*, Barcelona, September 11-14
- [81] Schäfer, M., Teschauer, I. (2001): Numerical simulation of coupled fluid-solid problems. *Comput. Methods Appl. Mech. Engrg.*, 190, 3645-3667
- [82] Silverman, I. , Sirignano, W. A. (1994): Multi-droplet interaction effects in dense sprays. *Int. J. Multiphase Flow*, 20, 99-116
- [83] Sommer, H. T. (1986): Ignition studies of fuel droplet streams. *Twenty-First Symposium (International) on Combustion*, 641-646
- [84] Sorensen, K. A., Hassan, O., Morgan, K., Weatherill, N. P. (2003): A multigrid accelerated time-accurate inviscid compressible fluid flow solution algorithm employing mesh movement and local remeshing. *Int. J. Numer. Meth. Fluids*, 43, 517-536
- [85] Sripada, S. S., Ayyaswamy, P. S., Huang, L. J. (1996): Condensation on a spray of water drops: a cell model study-I flow description. *Int. J. Heat Mass Transfer*, 39, 3781-3790
- [86] Stapf, P., Dwyer, H. A., Maly, R. (1998): A group combustion model for treating reactive sprays in I.C. Engines. *Twenty-Seventh Symposium (International) on Combustion*, The Combustion Institute, Boulder, CO, 1857-1864
- [87] Stone, H. L. (1968): Iterative solution of implicit approximations of multidimensional partial differential equations. *SIAM J. Numer. Anal.*, 5, 530-558
- [88] Tal, R., Lee, D. N., Sirignano, W. A. (1983): Hydrodynamics and heat transfer in sphere of particle assemblages - cylindrical cell models. *Int. J. Heat Mass Transfer*, 26, 1265-1273
- [89] Tal, R., Lee D. N., Sirignano W. A. (1984): Heat and momentum transfer around a pair of spheres in viscous flow. *Int. J. Heat Mass Transfer*, 27, 1953-1962

- [90] Tal, R., Sirignano, W. A. (1984): Cylindrical cell model for the hydrodynamics of particle assemblages at intermediate Reynolds numbers. *AIChE J.*, 28, 233-236
- [91] Tamura, Y., Fujii, K. (1993): Conservation law for moving and transformed grids. *AIAA 93-3365-CP*, presented at *AIAA 11 th Computational Fluid Dynamics Conference*, Orlando, Florida, U.S.A., July 6-9 1993.
- [92] Thomas, P.D., Lombard, C.K. (1979): Geometric conservation law and its application to flow computations on moving grids. *AIAA J.*, 17, 1030-1037
- [93] Thompson, J. F., Warsi, Z. U. A., Mastin, C. W. (1995): Numerical grid generation: Foundations and applications. *Elsevier Science Publishing Co. Inc.* (also available at thompson <http://www.erc.msstate.edu/publications/gridbook/>)
- [94] Tishkoff, J. (1979): A model for the effect of droplet interactions on vaporization. *Int. J. Heat Mass Transfer*, 22, 1407-1415
- [95] Trulio, J.G., Trigger, K.R. (1961): Numerical solution of the one-dimensional hydrodynamic equations in an arbitrary time-dependent coordinate system. *University of California Lawrence Radiation Laboratory Report UCLR-6522*
- [96] Tsai, J. S., Sterling, A. M. (1990): The application of an embedded grid to the solution of heat and momentum transfer for spheres in a linear array. *Int. J. Heat Mass Transfer*, 33, 2491-2502
- [97] Twardus, E. M., Brzustowski (1977): The interaction between two burning fuel droplets. *5th Int. Symposium on combustion processes*, Krakow, Poland
- [98] Umemura, A., Ogawa, A., Oshiwa, N. (1981): Analysis of the interaction between two burning droplets. *Combust. Flame*, 41, 45-55
- [99] Umemura, A., Ogawa, A., Oshiwa, N. (1981): Analysis of the interaction between two burning droplets with different sizes. *Combust. Flame*, 43, 111-119

- [100] Umemura, A. (1994): Interactive droplet vaporization and combustion: Approach from asymptotics. *Prog. Energy Combust. Sci.*, 20, 325-372
- [101] Xiong, T. Y., Law, C. K., Miyasaka, K. (1985): Interactive vaporization and combustion of binary droplet system. *Twentieth Symposium (International) on Combustion*, Combustion Inst., Pittsburgh, PA, 1781-1787
- [102] Zhang, J. , Fan, L. S. (2002): A semianalytical expression for the drag force of an interactive particle due to wake effect. *Industrial & Engineering Chemistry Research*, 20, 5094- 5097
- [103] Zung, J. T. (1967): Evaporation rates and lifetimes of clouds and sprays in air - The cellular model. *J. Chem. Phys.*, 46, 2064-2070

Eidesstattliche Erklärung

Ich erkläre hiermit, dass ich die vorliegende Arbeit selbst verfasst und mich dabei keiner anderen als der von mir ausdrücklich bezeichneten Quellen und Hilfen bedient habe.

Heidelberg, den 26.08.2005